UNIVERSIDAD DE SALAMANCA

Departamento de Ingeniería Cartográfica y del Terreno

TESIS DOCTORAL

MENCIÓN INTERNACIONAL

Multispectral Imaging for the Analysis of Materials
and Pathologies in Civil Engineering,
Constructions and Natural Spaces

Susana del Pozo Aguilera

Directores de Tesis:

Dr. Diego González Aguilera

Dr. Pablo Rodríguez Gonzálvez

2016

Departamento de Ingeniería Cartográfica y del Terreno

Escuela Politécnica Superior de Ávila

Universidad de Salamanca

AUTOR:

Susana del Pozo Aguilera

DIRECTORES:

Dr. Diego González Aguilera

Dr. Pablo Rodríguez
Gonzálvez

2016

Informe de los Directores de Tesis

Multispectral Imaging for the Analysis of Materials and Pathologies in Civil Engineering, Constructions and Natural Spaces

presentada en el
Departamento de Ingeniería Cartográfica y del Terreno

por
Susana del Pozo Aguilera

The Doctoral Thesis "*Multispectral Imaging for the Analysis of Materials and Pathologies in Civil Engineering, Constructions and Natural Spaces*", presented by Susana del Pozo Aguilera, is part of the research line entitled "*Radiometric analysis of images to study different land covers by optical remote sensing systems*" in which by using different active and passive sensors as conventional and multispectral cameras, different terrestrial laser systems or even their combination; different materials and pathologies regarding disciplines as civil engineering, cultural heritage and natural resources have been analysed.

Remote sensing is an invaluable tool when direct measurements are difficult or impossible to perform and lack of knowledge will result in costly expenditures, long delays or even wrong decisions. The evolution of optical remote sensing over the past few decades has enabled the availability of rich spatial, spectral and temporal information to remote sensing analysts without forgetting its non-invasive and non-destructive character. In this way, the present Thesis is framed within close-range imagery conducted by airborne and terrestrial-based platforms to accurately image different land surfaces with high resolution. It includes techniques to hybridise remotely sensed imagery acquired simultaneously from active and passive sensing modalities for a joint radiometric-geometric analysis to support decision making processes. With the advances in sensor technology and the increasing quantity of multi-sensor, multi-temporal, and multi-data from different sources, data fusion has become as a valuable tool in remote sensing applications.

Optical remote sensing focuses on the range from visible to near infrared light. Remote sensing systems used for imaging purposes in this spectral range are mostly passive systems, detecting the solar radiation reflected or transmitted by objects on Earth. But in this case, the contribution of the intensity data collected by active systems (terrestrial laser scanners) give an added value to the radiometric data from conventional passive sensors. This research line is not trendy or novel in the fields of Geomatics because it is a well-established technique that has long been used form many years, especially in the case of satellite observations. However, it offers a great scientific contribution in the close-range remote sensing area as it deals very rigorously, by using an in-house software developed for this purpose, the vicarious radiometric calibration of sensors, the data acquisition and its main common problems, the sensor and data fusion, potentials and limitations of several sensors and wavelengths regarding the field of application, the analysis of data and the extraction of valuable final products.

It is a line of research promoted and developed by the TIDOP Research Group (http://tidop.usal.es/) of the University of Salamanca, which is researching and developing software and hardware tools within competitive projects and in collaboration with other research groups and leading companies at national and international level. Specifically, this line is a topic of interest for the Department of Geoscience and Remote Sensing of the Faculty of Civil Engineering and Geosciences of the Delft University of Technology. They were interested in the application of a low-cost multispectral camera to the field of geology. As a result, Susana del Pozo Aguilera conducted a 3-months research stay at the Department in Delft (The Netherlands) under the supervision of Dr. Roderik Lindenbergh, which culminated with a high impact publication and give rise the third chapter of the Thesis.

The new scientific contributions and the valuable results obtained led to the publication of various scientific articles, all currently published in prestigious journals in the field of remote sensing, civil engineering and instrumentation, subject to anonymous peer review and indexed in databases Journal Citation Report (JCR), being in the top quartile (Q1) of their category. It is noteworthy that the results derived an intellectual

property and a technical book chapter which highlight the research, implementation and knowledge transfer capabilities of Susana del Pozo Aguilera.

The Doctoral Thesis is completed with a proper section of conclusions and future perspectives in which, the major contributions and recommendations for future works are precisely specified in order to complement this work being fully integrated into the line of research. Accordingly, this Thesis brings the cutting edge in signal processing and exploitation research closer to users and developers of remote sensing technology and it would be a valuable reference to graduate students and researchers in the academia and the industry who are interested in keeping abreast with the current state-of-the-art in signal and image processing techniques for optical remote sensing.

Given the conditions put forward, the supervisors consider that the present Doctoral Thesis is suitable for submission and public defence in the form of *"Compendium of Publications"* and with *"International Mention"* since it presents more than sufficient original results according to the requirements and regulations established by the University of Salamanca in this regard. In witness whereof, this certificate has been signed at

Ávila, 10 February 2016,

Dr. Diego González Aguilera   Dr. Pablo Rodríguez Gonzálvez

Aval internacional correspondiente a la Tesis Doctoral

Multispectral Imaging for the Analysis of Materials and Pathologies in Civil Engineering, Constructions and Natural Spaces

A continuación se adjuntan dos informes de evaluación de la Tesis escritos por dos doctores pertenecientes a instituciones no españolas

EVALUATION LETTER OF THE DOCTORAL THESIS WITH THE "INTERNATIONAL MENTION" FORM ORGANIZED AS A COMPENDIUM OF SCIENTIFIC PAPERS

Dr. Tim Vlemmix

Department of Geoscience & Remote Sensing

Faculty of Civil Engineering and Geosciences

Stevinweg 1, 2628 CN, Delft, the Netherlands

t.vlemmix@tudelft.nl

+31 15 27 83 417

21 January 2016

Subject: Thesis Review

To whom it may concern,

With great pleasure I have been reading the PhD dissertation *Multispectral Imaging for the Analysis of Materials and Pathologies in Civil Engineering, Constructions and Natural Spaces* written by *Susana del Pozo Aguilera* (University of Salamanca, Department of Cartographic and Land Engineering). Before evaluating, I will summarize shortly the content of this work.

The thesis opens with an introductory chapter describing the principles of remote sensing and different type of sensors. Also the principles of radiometric calibration are discussed as well as techniques for multispectral data analysis (supervised and unsupervised classification). The remainder of the introductory chapter describes the motivation and objectives for this work, namely to develop a vicarious radiometric calibration protocol in order to allow synergistic use of multiple sensors in a wide range of application areas (e.g. environmental monitoring, cultural heritage monitoring).

The development and results of the calibration method are described in the second chapter. The authors developed their own software package (MULRACS) for this purpose, and this software is also made publicly available. Methods are tested on field measurements using an unmanned aerial system flying at low altitude over natural terrain where artificial targets (low cost vinyl sheets) with well-known spectral properties were added. The low error w.r.t. the final calibration factors demonstrates the successfulness of the developed workflow.

The third chapter is about an application in the field of geology and describes methods to discriminate between sedimentary rocks using two different data t ypes: close-range visible

and very-near infrared images. Observations were performed in the Rhone-Alpes region in France. Like in the previous part of the study, a reference panel was used to correct for the varying solar irradiance (effectively a correction for atmospheric modification of the solar irradiance). It was concluded that two types of rock can be discriminated using the multispectral camera: limestone and marlstone. Discrimination between limestone and sandstone is remains a challenge. Cloudy days are favourable for this type of analysis because of fewer issues with shadowing. In future studies information about the BRDF of this type of rock would enhance the potential of this technique.

Chapter four describes a study devoted to quite a different field of application: detection and quantification of physical and chemical pathologies in facades of cultural heritage. In addition to the multispectral camera, a laser scanning system is used (essentially the primary instrument used in this study because of several advantages related to active remote sensing). Different classification algorithms are compared (Fuzzy K-means clustering and maximum likelihood). A spectroradiometer was used for validation. One of the main conclusions is that adding intensity information to multispectral information improves classification both qualitatively and quantitatively. Another section of chapter four focuses on the mapping of surface moisture affectation in concrete structures. Chapter four concludes with a chapter written for a textbook on *Geotechnologies for the Reverse Engineering of Structures and Infrastructures*. This informs readers about, amongst others, using remote sensing instrumentation for efficient and cost effective damage assessments and the added value of multispectral systems.

Altogether the work described in this thesis is very complete in the sense that the PhD candidate has been working with various sensors (active and passive), performed both laboratory experiments and various types of fieldwork, developed and used a range of software packages and did this in quite different fields of application (geology, cultural heritage, structural engineering). These activities have been executed with considerable success, as described in this thesis. The study has lead to convincing conclusions and recommendations for future work, mostly from an instrumental perspective. In addition the thesis has a clear structure and is very well written in the English language. This is also proven by the fact that the three main chapters are either published or accepted for final publication in peer-reviewed journals. Therefore I strongly recommend Susana del Pozo Aguilera to obtain the degree of International Doctor at the University of Salamanca in Spain and I would like to congratulate both her and her supervisors with this work.

With friendly greetings,

Dr. Tim Vlemmix

Department of Geoscience & Remote Sensing

Delft University of Technology

Dr Fabio Menna
3D Optical Metrology (3DOM) unit
Bruno Kessler Foundation (FBK)
Via Sommarive 18, 38123 Povo (Trento) - Italy
Tel. +39 0461 314446
Web: http://www.fbk.eu; http://3dom.fbk.eu
Email: fmenna@fbk.eu

External examiner review for the International PhD thesis "Multispectral Imaging for the Analysis of Materials and Pathologies in Civil Engineering, Constructions and Natural Spaces" by Susana del Pozo Aguilera, Department of Cartographic and Land Engineering, University of Salamanca, Spain

The research work deals with the study and classification of materials and pathologies in civil engineering and related disciplines through automatic procedures which use either a commercially available camera or a terrestrial laser scanner or even their combination. A research software has also been developed for the radiometric calibration of passive sensors at close-range distances. Radiometric as well as geometric calibration are investigated in order to accurately compute the electromagnetic energy reflected by the materials observed in the scene. The exclusive use of each technology and their comparison is also discussed.

The thesis is well written, literature review and related works are quite complete with good figures and graphics that are in general explanatory and relevant.

The material/content is well-structured and organized although, in my opinion, the book chapter would have fit better at the beginning of the thesis instead of being the last chapter. Nevertheless if the structure of the thesis requires the chronological order of candidate's record of publications it does not represent an issue.

The length of the thesis is sufficient to accurately describe in detail the proposed method and its innovative outcomes. Due to the listing of single publications some topics are often repeated but this does not represent a demerit in my opinion, rather it highlights the strength of the methodology/technique which has been successfully applied in different fields demonstrating its robustness.

As far as calibration of the multispectral camera is concerned, the work carried out by Susana del Pozo Aguilera is mainly based on the vicarious radiometric calibration which is a well-established technique for in situ verification of multispectral sensors. Also, the correction of image vignetting and geometrical distortions are well known concepts but the author has also remarked their influence on the radiometric calibration.

Susana del Pozo Aguilera has also developed a software for Multispectral Radiometric Calibration named "MULRACS" that will be provided along with the thesis. The software is explained in appendix B even though in my opinion there are too few details to provide a fair evaluation.

Page | 1 of 2

Dr Fabio Menna
3D Optical Metrology (3DOM) unit
Bruno Kessler Foundation (FBK)
Via Sommarive 18, 38123 Povo (Trento) - Italy
Tel. +39 0461 314446
Web: http://www.fbk.eu; http://3dom.fbk.eu
Email: fmenna@fbk.eu

As overall evaluation, in my opinion, the thesis is a good and comprehensive study that will be a reference guide for scientists and engineers who need to use low cost but reliable procedures for classifications based on close range and low altitude UAS surveys. The fusion of data coming from different sensors has also been proved effective. The writing is accurate and often enriched by critical comments. The overall scientific merit is high due to the candidate ability to highlight the range of applicability of the technique, its strength and limitations with respect to the field of application as for instance when applying the technique in the terrestrial case for geological purposes.

I strongly recommend the author to obtain the degree of International Doctor at the University of Salamanca in Spain.

Trento, 8/02/2016

Fabio Menna – FBK Trento, Italy

Listado de artículos publicados

Esta Tesis Doctoral consiste en un compendio de 4 artículos científicos y un capítulo de libro, publicados en revistas internacionales de alto impacto. A continuación se enumeran estas publicaciones.

1. **Vicarious radiometric calibration of a multispectral camera on board an unmanned aerial system**

Susana Del Pozo[1], Pablo Rodríguez-Gonzálvez[1], David Hernández-López[2] and Beatriz Felipe-García[2]

[1]Department of Cartographic and Land Engineering, University of Salamanca, Hornos Caleros, Ávila 05003, Spain
[2]Institute for Regional Development (IDR), Albacete, University of Castilla La Mancha, Ciudad Real 13003, Spain

2. **Discrimination between sedimentary rocks from close-range visible and very-near infrared images**

Susana Del Pozo[1], Roderik Lindenbergh[2], Pablo Rodríguez-Gonzálvez[1], Jan Kees Blom[2] and Diego González-Aguilera[1]

[1]Department of Cartographic and Land Engineering, University of Salamanca, Polytechnic School of Ávila, Ávila, Spain
[2]Department of Geoscience and Remote Sensing, Delft University of Technology, Delft, The Netherlands

3. **Multispectral radiometric analysis of façades to detect pathologies from active and passive remote sensing**

Susana Del Pozo[1], Jesús Herrero-Pascual[1], Beatriz Felipe-García[2], David Hernández-Lopez[2], Pablo Rodríguez-Gonzálvez[1] and Diego González-Aguilera[1]

[1]Department of Cartographic and Land Engineering, University of Salamanca, Hornos Caleros, Ávila 05003, Spain
[2]Institute for Regional Development (IDR), Albacete, University of Castilla La Mancha, 02071, Albacete, Spain

4. **Automatic mapping of moisture affectation in exposed concrete structures by fusing different wavelength remote sensors**

Borja Conde[1], Susana del Pozo[2], Belén Riveiro[1] and Diego González-Aguilera[2]

[1]Department of Materials, Engineering, Applied Mechanics and Constructions, School of Industrial Engineering, University of Vigo, Vigo, 36208, Spain
[2]Department of Cartographic and Land Engineering, High School of Ávila, University of Salamanca, Ávila 05003, Spain.

5. **Multispectral imaging: fundamentals, principles and methods to damage assessment in constructions**

Susana del Pozo[1], Luis Javier Sánchez-Aparicio[1], Pablo Rodríguez-Gonzálvez[1], Jesús Herrero-Pascual[1], Ángel Muñoz-Nieto[1], Diego González-Aguilera[1] and David Hernández-López[2]

[1]Department of Cartographic and Land Engineering. High School of Ávila, University of Salamanca, Ávila, Spain
[2]Regional Development Institute IDR, University of Castilla La Mancha, Albacete, Spain

A mis padres

y hermanos

La energía radiante óptica ha sido siempre el nexo de unión entre el sistema visual humano y el mundo exterior, siendo la energía solar esencial para el crecimiento y desarrollo biológico.

(Grum, 2012)

Abstract

Multispectral imaging is a non-destructive technique that combines imaging and spectroscopy to analyse the spectral behaviour of materials and land covers through the use of geospatial sensors. These sensors collect both spatial and spectral information for a given scenario and a spectral range, so that, their graphical representation elements (pixels or points) store the spectral properties of the radiation reflected by the material sample or land cover. The term multispectral imaging is commonly associated with satellite imaging, but the application range extends to other scales as close-range photogrammetry through the use of sensors on board of airborne systems (gliders, trikes, drones, etc.) or through their use at ground level. Its usefulness has been proved in a variety of disciplines from topography, geology, atmospheric science to forestry or agriculture. The present thesis is framed within close-range remote sensing applied to the civil engineering, cultural heritage and natural resources fields via multispectral image analysis.

Specifically, the main goal of this research work is to study and analyse the radiometric behaviour of different natural and artificial covers by combining several sensors recording data in the visible and infrared ranges of the spectrum. The research lines have not been limited to the 2D data analysis, but in some cases 3D intensity data have been integrated with 2D data from active (terrestrial laser scanners) and passive (multispectral digital cameras) sensors in order to analyse different materials and possible associated pathologies, getting more comprehensive products due to the metric that 3D brings to 2D data.

Works began with the radiometric calibration of the active and passive sensors used by the vicarious calibration method. The calibrations were carried out through MULRACS, a multispectral radiometric calibration software developed for this purpose (see Appendix B). After the calibration process, active and passive sensors were used together for the discretization of sedimentary rocks and detecting pathologies, as moisture, in façades and in civil structures. Finally, the Doctoral Thesis

concludes with a theoretical book chapter in which all the know-how and expertise arising during this research stage have been compiled.

Resumen

Las imágenes multiespectrales se constituyen como técnica no destructiva que combina imagen y espectroscopía para analizar el comportamiento espectral de distintos materiales y superficies terrestres a través del uso de sensores geoespaciales. Estos sensores adquieren tanto información espacial como espectral para un escenario y un rango espectral dados de tal forma sus unidades de representación gráfica (ya sean píxeles o puntos) registran las propiedades de la radiación reflejada para cada material o cobertura a estudiar y longitud de onda. Las imágenes multiespectrales no solo se limitan a las observaciones satelitales a las que tradicionalmente se vinculan, sino que tienen un campo de aplicación más amplio gracias a los estudios de rango cercano realizados a través del uso de sensores tanto embarcados en sistemas aéreos (planeadores, paramotores, drones, etc.) como a nivel terreno. Su utilidad ha sido demostrada en multitud de disciplinas; desde la topografía, geología, aerología, hasta la ingeniería forestal o la agricultura entre otros. La presente tesis se enmarca dentro de la teledetección de rango cercano aplicada a la ingeniería civil, el patrimonio cultural y los recursos naturales a través del análisis multiespectral de imágenes.

Concretamente, el principal objetivo de este trabajo de investigación consiste en el estudio y análisis del comportamiento radiométrico de distintas coberturas naturales y artificiales mediante el uso combinado de distintos sensores que registran información espectral en los rangos visible e infrarrojo del espectro electromagnético. Las líneas de investigación no se han limitado al análisis de datos bidimensionales (imágenes) sino que en algunos casos se han integrado datos de intensidad registrados en 3D a través de sensores activos (láser escáner terrestres) con datos 2D capturados con sensores pasivos (cámaras digitales convencionales y multiespectrales) con el objetivo de analizar diferentes materiales y posibles patologías asociadas a los mismos ofreciendo resultados más completos gracias a la métrica que los datos 3D aportan a los datos 2D.

Los trabajos comenzaron con la calibración radiométrica de los sensores por el método de calibración vicario. Las calibraciones fueron resueltas gracias al uso del software MULRACS, un software para la calibración radiométrica multiespectral desarrollado durante este periodo para tal fin (ver Apéndice B). Tras el proceso de calibración, se combinó el uso de sensores activos y pasivos para la diferenciación de distintos tipos de rocas sedimentarias y la detección de patologías, como humedades, en fachadas de edificios históricos y en estructuras de ingeniería civil. Finalmente, la Tesis Doctoral concluye con un capítulo teórico de libro en el cual se recopilan todos los conocimientos y experiencias adquiridos durante este periodo de investigación.

Acknowledgements

Life is a process of becoming, a constant combination of roads we have to choose and go through. The eternal question about whether we have chosen the right path is always raised, but the important thing is not the path but how we live and experience the chosen path. Four and a half years ago I was offered to start a PhD and I decided to embark on that adventure without knowing exactly what this would mean at all.

Professionally, the development of the Thesis involved a personal challenge considering that my background experience was linked to the field of Civil Engineering. This period has been rewarding in many ways. On the one hand, I have gained new knowledge and explored a new discipline, proving to be complementary to my background career. On the other, every obstacle has been an opportunity to know me better and be aware of the importance that values such as dedication and patience have to succeed in any project. I would say in summary that this period has been enriching in terms of scientific development and personal growth. But this would not have been possible without all your support. I want to thank you for helping me to make it possible.

First of all, I would like to thank my daily supervisors: Diego González Aguilera and Pablo Rodriguez Gonzálvez. Thank you for sharing all your scientific knowledge, unconditional support and advices during all these years. You have been a key figure not only for the development of this Thesis but also in many moments of ups and downs in which you have known how to motivate and encourage me to continue. You are the true example of wisdom, level-headedness and leadership; essential to the success and growth of any team. I admire your dedication and commitment; they are definitely out of the ordinary. My greatest admiration for both.

I also want to thank the assistance and collaboration received from all the members of the Institute of Regional Development (IDR) at the University of Castilla la Mancha, especially to David Hernández López and Beatriz Felipe García.

I would like to make a special mention and great recognition to the people of the Department of Geoscience and Remote Sensing of the Delft University of Technology (The Netherlands) which welcomed me with affection during a three-month research stay. Specially, I want to thank Roderik Lindenberh, my supervisor during the stay, all the assistance provided during this collaboration period. Roderik, thanks for opening the doors for me and for giving me the opportunity to work with you and your team. From the first moment I felt a warm welcome and felt at home. That stay, although it was short, gave me a personal and professional boost and created a before and after in my life. I will always be grateful to you.

A big thanks to all the members of the TIDOP Research Group of the University of Salamanca, in particular to my lab colleagues and friends who have suffered me every day and have always been willing to help me whenever they could. Thanks guys.

Special thanks to all my friends to follow my routine with the same passion as myself and to understand my absence at certain times. Thank you because as you know these four and a half years have not been easy at all. Thanks for listening to me, putting up with me and specially, for all the fun times. You are the best.

I would like also to thank Sita and Fernan, words are not needed.

Finally, I want to thank my family, my greatest treasure, specially my parents and brothers. Without your unconditional love, support and guidance I would not be who I am today. Thanks Mom and Dad for always believing in me and supporting me in all roads I have chosen these years. Thank you for your effort and dedication, for giving Gonzalo, Peque and me everything, for motivating us to grow and become better people. Always in my mind, forever in my heart.

Thank you all. Certainly, this work is part of all of you.

Agradecimientos

La vida es un devenir constante de decisiones y caminos que tomar y siempre se nos plantea la eterna duda de si habremos elegido o no el camino correcto. Pero lo importante no es el camino sino cómo vivimos el camino, sea cual sea este. Hace cuatro años y medio se me planteó la posibilidad de comenzar el Doctorado y decidí embarcarme en esta aventura sin saber muy bien lo que esto supondría en ningún sentido.

Profesionalmente, el desarrollo de la Tesis ha sido todo un reto personal teniendo en cuenta mi experiencia ligada al mundo de la Ingeniería Civil; resultando finalmente ser enriquecedor en todos los sentidos. Por un lado, he adquirido nuevos conocimientos explorando una nueva disciplina complementaria a mi carrera; y por otro, he encontrado en cada obstáculo una oportunidad para conocerme un poquito mejor y ser consciente de la importancia que tienen valores como la dedicación y la paciencia en el éxito de cualquier proyecto o meta. Esto no habría sido posible sin vuestra ayuda y apoyo y por eso quiero daros las gracias.

Quiero comenzar agradeciendo a mis Directores de Tesis: Diego González Aguilera y Pablo Rodríguez Gonzálvez. Gracias por todos los conocimientos que me habéis inculcado durante este periodo y vuestra ayuda y apoyo incondicionales. Habéis sido claves no solo para el desarrollo de esta tesis sino en muchos momentos de altibajos personales en los que habéis sabido motivarme para continuar. Sois el fiel ejemplo de sabiduría, ecuanimidad y liderazgo, esenciales para el éxito y el crecimiento de cualquier equipo, y que a menudo son tan difíciles de encontrar en consonancia. Admiro vuestra dedicación y compromiso, son definitivamente algo fuera de lo normal. Mi mayor admiración hacia los dos.

También quisiera agradecer la ayuda y colaboración recibidas por parte de los miembros del Instituto de Desarrollo Regional (IDR) adscrito a la Universidad de Castilla la Mancha y especialmente a David Hernández López y Beatriz Felipe García.

Índice

Capítulo I

INTRODUCCIÓN

1. INTRODUCCIÓN

Las imágenes multiespectrales se constituyen como técnica no destructiva gracias a la cual es posible adquirir información espectral de distintas cubiertas terrestres de forma remota y mediante el uso de: (i) sensores sensitivos a varias longitudes de onda (Zhang et al., 2006) o (ii) varios sensores al mismo tiempo. Esto es posible gracias al análisis de la respuesta radiométrica de cada material a cada longitud de onda para la que es capaz de capturar información el sensor o sensores empleados. El término radiometría abarca diversas materias, desde los conceptos básicos de flujo radiante, energía y su transferencia, hasta la calibración de los equipos para permitir su uso en diferentes campos de aplicación (Grum, 2012). El propósito de esta Tesis Doctoral consiste en abarcar equitativamente todos estos puntos apostando por la hibridación sensorial para ampliar el alcance que un solo sensor puede ofrecer, y por tanto, realizar estudios más amplios y completos. En este sentido, se hace uso de las imágenes multiespectrales como alternativa no destructiva a los métodos de inspección más expeditos en los campos de la ingeniería civil, el patrimonio cultural y los recursos naturales.

Esta técnica se basa en la interacción de la energía con cada material o superficie terrestre. Concretamente, se centra en el estudio de la proporción de energía reflejada por cada superficie para cada longitud de onda del espectro, es decir, el estudio de la firma espectral de cada material. La firma espectral es una reseña única de identidad de cada material (Shaw and Burke, 2003) y, por tanto, cualquier variación en ella puede dar constancia de cualquier alteración química o mecánica producida en dicho material.

Las imágenes multiespectrales se vinculan convencionalmente a las imágenes satelitales debido a que la Tierra ha sido estudiada y observada por este tipo de imágenes desde 1960 (Davis, 2007) a diferentes resoluciones espaciales, temporales y espectrales a través de sensores instalados en multitud de satélites. Gracias a estas imágenes es posible

llevar a cabo estudios que abarcan desde los recursos naturales hasta el sistema climático y sus cambios. La mayor ventaja radica su potencial para proporcionar observaciones a nivel global para un gran conjunto de cubiertas terrestres (Justice et al., 2002; Bartholomé y Belward, 2005). Mientras que hoy en día estas imágenes siguen siendo muy importantes para llevar a cabo estudios globales, las imágenes multiespectrales no se limitan a las observaciones satelitales sino que también se utilizan con éxito para ciertos estudios de coberturas que requieren mayor resolución y una adquisición más cercana. Esto es posible mediante el uso de diversas plataformas tanto a nivel aéreo como terrestre (Knoth et al., 2013; Brooke, 1989).

Este es el punto de partida del presente trabajo de investigación: el estudio multiespectral de rango cercano de diferentes cubiertas y materiales terrestres mediante el uso de sistemas aéreos y plataformas terrestres para sacar partido a las alternativas y soluciones que las nuevas geotecnologías ofrecen para realizar estudios de mayor resolución. A lo largo del desarrollo de esta Tesis Doctoral existe una clara apuesta por la fusión e integración de datos espectrales recogidos por diferentes sensores con el fin de obtener un registro más completo sobre las coberturas a examinar y una mayor precisión a la hora de evaluar los resultados que los que cabrían esperarse de los extraídos de un único sensor (Pohlc, 1998).

El objetivo del presente capítulo es servir de parte introductoria a la Tesis Doctoral donde se detallará el contexto, alcance, motivación, objetivos y estructura del trabajo de investigación desarrollado.

1.1. Fundamentos teóricos

1.1.1. Introducción a la teledetección y sus fundamentos

Cuando un objeto recibe radiación ya sea ésta emitida por el sol u otra fuente, dependiendo del tipo de objeto considerado y las características de su superficie, esta radiación puede seguir tres caminos: ser reflejada, absorbida o transmitida (Joseph, 2005). A la fracción de energía reflejada se le denomina reflectividad o albedo (ρ); a la fracción absorbida se le

denomina absortividad (α) y a la fracción transmitida transmisividad (τ), y cuya suma cumple la ley de conservación de la energía (Ecuación 1):

$$\rho + \alpha + \tau = 1 \tag{1}$$

Mediante la teledetección es posible estudiar este comportamiento de la radiación y derivar conclusiones acerca del estado físico y químico de los materiales. El término teledetección ha sido definido de muchas maneras dependiendo del propósito de la técnica. La definición que se muestra a continuación (Davis et al., 1978) es general y está en línea con los desarrollos y aplicaciones desarrollados en la presente Tesis Doctoral:

"La teledetección es la ciencia por la que a través de distintas mediciones realizadas de forma remota, es decir, sin llegar a entrar en contacto con los objetos de interés, se deriva información acerca de ellos. La magnitud medida con mayor frecuencia por estos sistemas de percepción remota es la energía electromagnética reflejada"

Existen dos tipos de técnicas de percepción remota para la adquisición de datos: los sistemas activos y los sistemas pasivos (Barret, 2013), ambos igualmente válidos y que ofrecen diferentes herramientas funcionales. En la *teledetección pasiva* se hace uso de sensores capaces de capturar la radiación solar reflejada o emitida por los distintos objetos. La región que abarca el visible, infrarrojo cercano e infrarrojo de onda corta (entre 0.4 µm y 3 µm) es el rango espectral reflexivo solar ya que la energía que el sol suministra a la superficie terrestre supera la emitida por la propia tierra en este rango (Schowengerdt, 2006). Por su lado, la *teledetección activa* hace uso de una fuente artificial de radiación para estudiar los materiales de tal forma que la señal reflejada por la superficie de los mismos, y que es registrada de vuelta en el sensor, caracteriza el tipo de material. La representación gráfica de los resultados finales procedentes de un sensor activo no tienen formato de imagen por lo que hibridar ambas técnicas de teledetección supone llevar a cabo un riguroso procesado y registro de los datos procedentes de ambas tecnologías.

1.1.2. Sensores

Los sensores empleados en teledetección óptica (rangos visible, infrarrojo cercano e infrarrojo de onda corta) convierten la radiación

entrante en una señal cuya salida es, en formato digital, proporcional a la distribución espacial de luminosidad recibida. En este punto se producen ciertas transformaciones de las características espaciales, radiométricas y geométricas de la radiación de entrada. Es importante estudiar cuidadosamente estas alteraciones para diseñar adecuadamente los algoritmos de procesamiento de los datos y hacer una correcta interpretación de los resultados (Schowengerdt, 2006). Los detectores empleados para capturar y registrar la radiación de entrada son detectores cuánticos fabricados con materiales semiconductores (Richtmeyer et al., 1968). Éstos convierten la radiación entrante en una señal electrónica que se amplifica y posteriormente se procesa por la electrónica del sensor. En la digitalización o conversión analógica-digital (A/D) la señal procesada se muestrea y cuantifica en niveles digitales[1] en función de la resolución radiométrica del sensor.

Los sistemas de teledetección se caracterizan no solo por su resolución radiométrica sino también por su resolución espacial, espectral y temporal (Parr et al., 2005). La *resolución radiométrica* como se ha comentado, es la resolución numérica asociada a la cuantificación de la radiación, es decir, la sensibilidad que tiene un sensor para discriminar distintas variaciones de luminosidad. Bajo el concepto de *resolución espacial* está la capacidad del sistema para distinguir objetos, es el tamaño del objeto más pequeño que puede ser distinguido por el sensor. Depende principalmente de la distancia objeto-sensor y del campo de visión. La *resolución espectral* es la sensibilidad de un sensor para discriminar cierto número y anchura de bandas del espectro electromagnético. Los sensores multiespectrales son aquellos sistemas que son capaces de registrar la radiación en varias longitudes de onda y a diferentes resoluciones espectrales. Finalmente, la *resolución temporal* se refiere al intervalo de tiempo transcurrido entre las distintas adquisiciones de datos.

En el caso concreto de las imágenes multiespectrales, los sensores usan sistemas multi-lente con combinación de filtros para adquirir simultáneamente imágenes para el rango espectral característico de cada filtro. Tienen la gran ventaja de que registran la radiación reflejada en

---

[1] 2^b niveles digitales, donde *b* es la resolución radiométrica del sensor en bits.

rangos discretos del espectro aunque el análisis simultáneo de esas imágenes no es un tema trivial (Colwell, 1961) tal y como se evidenciará durante el desarrollo de la presente Tesis Doctoral.

1.1.3. Calibración radiométrica de los sensores

Antes de comenzar con la descripción del proceso de calibración propiamente dicho, se debe hacer una pequeña introducción a ciertos conceptos que son necesarios para el estudio de las imágenes espectrales. La *irradiancia (E)* es la magnitud utilizada para caracterizar la energía luminosa incidente en una superficie por unidad de tiempo, normalmente se mide en W/m^2. La *reflectancia (ρ)* es un número adimensional entre 0 y 1, habitualmente expresado en porcentaje, que determina la proporción de luz reflejada por una superficie con respecto a la luz incidente. La reflectancia depende a su vez de parámetros como la longitud de onda, el ángulo de incidencia de la radiación y el ángulo de reflexión. La *radiancia (L)* es un concepto que no distingue entre la radiación que incide sobre una superficie y la que es reflejada por la misma, es simplemente la irradiancia normalizada por unidad de ángulo sólido (en estereorradianes) del observable en la dirección de propagación de la luz. Se mide comúnmente en W/m^2·sr. Si la radiancia está normalizada por longitud de onda (en µm), se le denomina *radiancia espectral,* y sus unidades son W/m^2·sr·µm. La Ecuación 2 muestra la relación que existe entre estos conceptos radiométricos.

$$\rho = \frac{L}{E} \cdot \pi \qquad\qquad (2)$$

Si bien los datos brutos procedentes de los sensores, en niveles digitales, pueden ser analizados y aplicados en muchos campos sin necesidad de realizar ningún procesamiento adicional (Robinove, 1982), esta metodología no exprime todas las posibilidades que pueden derivarse de haber realizado un proceso de calibración radiométrico previo. Para llevar a cabo estudios más completos de la mano de la hibridación sensorial, tanto el formato como la magnitud final que ofrezca cada sensor debe ser la misma, para ello, los niveles digitales brutos deben ser transformados a los correspondientes valores físicos de radiancia o reflectancia del material a estudiar. Estos valores físicos a nivel sensor se

obtienen tras aplicar los coeficientes de calibración radiométricos de cada banda espectral del sensor (Dinguirard and Slater, 1999). En el campo de la teledetección, existen dos métodos de calibración radiométrica: la calibración absoluta y la relativa (Lo and Yang, 1998). La *calibración radiométrica absoluta* determina para cada banda espectral en que registra el sensor los parámetros necesarios para transformar los niveles digitales a valores físicos. Normalmente, para el caso de los sensores pasivos se emplean modelos lineales (Richards y Richards, 1999) definidos por la pendiente de la recta y la ordenada en el origen, gain y offset respectivamente. Por su lado, *la calibración radiométrica relativa* consiste en normalizar los valores de salida del sensor cuando existe una radiación incidente uniforme. La calibración radiométrica absoluta puede resolverse mediante el *método basado en radiancias* o el *método basado en reflectancias*.

Los métodos de calibración radiométrica absoluta más conocidos son (Honkavaara et al., 2009): la calibración en laboratorio, a bordo de un vehículo o plataforma aérea, la calibración vicaria y la auto-calibración. La *calibración vicaria*, que es la que se aplica en la presente tesis, consiste en una calibración realizada en un campo de pruebas a partir de una serie de medidas de reflectancia o radiancia de una serie de superficies artificiales y naturales a través de un espectrorradiómetro calibrado (Thorne et al., 1997). Se basa en los modelos de transferencia radiativa limitados por la medida de los valores superficiales y las características atmosféricas del momento (Slater et al., 1996).

Una vez realizada la calibración del sensor, es posible extraer valores físicos de la superficie de cualquier material y en función de la resolución espectral de el(los) sensor(es) empleado(s), extraer su firma espectral y derivar información de utilidad acerca de las características del material estudiado.

1.1.4. Análisis multispectral de los datos

El análisis multiespectral de los datos consiste fundamentalmente en una *clasificación* de los píxeles de las imágenes para identificar áreas con distintas propiedades físicas. Si se quieren integrar datos procedentes de distintos sensores, se ha de realizar un proceso previo de unificación de

formatos. Es decir, si se combinan por ejemplo datos de intensidad procedentes de un sensor láser escáner (sensor activo) con datos procedentes de un sensor pasivo, los datos 3D procedentes del láser deben ser convertidos a imágenes 2D de tal forma que la resolución radiométrica y espacial final de ambos sensores sea la misma. Por lo tanto, antes de realizar el proceso de clasificación se han de aplicar ciertas rectificaciones geométricas y transformaciones radiométricas a los datos.

La clasificación se lleva a cabo normalmente para datos multi-banda, es decir, para conjuntos de imágenes registradas en distintas longitudes de onda. Así, una clase es asignada a un pixel particular en función de su radiometría y características espectrales para esas longitudes de onda analizadas. Los procedimientos más comunes de clasificación son el método supervisado y el no supervisado (Lillesand et al., 2014). En la *clasificación supervisada*, el analista comienza identificando subconjuntos de píxeles representativos de los diferentes tipos de cobertura de interés, las denominadas clases informacionales. Estas muestras conforman las áreas de entrenamiento y recogen toda la información radiométrica de los píxeles seleccionados (en niveles digitales o valores físicos, dependiendo de si el sensor ha sido previamente calibrado o no) para el conjunto de bandas espectrales analizadas. Esta información se utiliza para entrenar al algoritmo de clasificación empleado en el reconocimiento de similitudes espectrales (Campbell, 2002). Sin embargo para el caso de la *clasificación no supervisada,* el proceso descrito con anterioridad se invierte (Jensen and Lulla, 1987). En primer lugar, las imágenes se clasifican automáticamente mediante un proceso de agrupación iterativo creando distintas áreas, los llamados clusters. Los algoritmos empleados se basan únicamente en la información radiométrica del conjunto de los datos aunque por lo general el analista especifica primero el número de clusters a diferenciar. El resultado final del proceso de agrupación iterativo ofrece grupos de píxeles que el analista puede posteriormente combinar o eliminar. Los resultados ofrecidos por ambos métodos resultan de gran utilidad para muchas disciplinas que demandan estudios de materiales y superficies terrestres.

1.2. Motivación

No cabe duda de que las imágenes multiespectrales tomadas a corta distancia han experimentado un resurgimiento notable como complemento a la teledetección satelital (Zhou et al., 2009) permitiendo hacer estudios de mayor detalle y resolución, tanto espacial como temporal, de las superficies terrestres de interés. Si bien es cierto que los estudios multiespectrales de corto alcance llevan tiempo instaurados, explorar esta técnica desde la perspectiva del bajo coste evaluando los potenciales, errores y eficiencias derivadas de su uso en base a la calibración radiométrica de los sensores empleados fue la principal motivación de esta Tesis Doctoral. Por esta razón, se decidió establecer el punto de partida en la calibración radiométrica de un sensor multiespectral de bajo coste embarcado en un sistema aéreo no tripulado. La idea era desarrollar un protocolo completo y de bajo coste para modelar el comportamiento radiométrico de dicho sensor teniendo en cuenta la posible afectación atmosférica para finalmente emplear dicho sensor de forma robusta en diversos análisis y para distintas coberturas terrestres.

Dado que un proceso de calibración no se considera válido hasta que el sensor se evalúa en condiciones reales de campo, se planteó la necesidad de evaluar su eficacia en diferentes escenarios. Se propusieron tomas de datos tanto desde plataformas aéreas como a nivel terreno y para escenarios favorables, intermedios y desfavorables, según las características espectrales del sensor, para realizar una evaluación lo más completa posible de sus potenciales y limitaciones al respecto.

Finalmente, y dado que cualquier sensor tiene sus propias limitaciones derivadas tanto de su principio de funcionamiento como de su configuración, se planteó la hibridación de sensores con diferentes principios de funcionamiento y resoluciones espectrales como solución para estudiar contextos desfavorables en los que el sensor multiespectral calibrado pudiera estar limitado. Se propuso el uso combinado de este sensor multiespectral con otros sensores pasivos y activos con el objetivo de ampliar el campo de aplicación de los análisis. De esta manera, los productos finales se verían mejorados no solo en términos radiométricos

sino también en términos geométricos, ofreciendo productos muy atractivos y útiles para la Comunidad Científica Internacional.

1.3. Objectivos

En este contexto, el **objetivo general** de la investigación consiste en realizar análisis multiespectrales completos y rigurosos en los que se apueste por la hibridación sensorial con base en la calibración radiométrica vicaria de los sensores para realizar análisis espectrales de una mayor variedad de coberturas terrestres.

Para conseguir este objetivo general se establecen los siguientes **objetivos específicos**:

- Profundizar en el conocimiento de las leyes, teorías y conceptos de radiometría y ponerlos en práctica en la calibración radiométrica de una cámara multiespectral de bajo coste.

- Estudiar y corregir los posibles errores sistemáticos que puedan ser transmitidos a las imágenes finales derivados del uso de sensores de bajo coste

- Analizar la posibilidad de usar tarjetas artificiales de bajo coste como puntos de control radiométrico en el proceso de calibración de los sensores.

- Incluir estimadores robustos y pruebas estadísticas en el proceso de calibración que den cuenta de su precisión para validar el procedimiento.

- Comprender la relevancia que tiene el concepto de resolución, en general, para el análisis de imágenes y, de forma particular, la importancia que la resolución espacial, espectral, radiométrica y temporal tienen para cada caso de estudio concreto.

- Hacer una revisión de los métodos y procedimientos que la Comunidad Científica Internacional emplea para el procesado multiespectral de imágenes.

- ▪ Automatizar el proceso de calibración radiométrica vicaria y los procesos de fusión de datos multiespectrales para simplificar los análisis radiométricos de las imágenes.

- ▪ Analizar el potencial y limitaciones de un sensor multiespectral después de haber sido aplicado a un caso de estudio no favorable.

- ▪ Analizar espectralmente diferentes coberturas terrestres tal y como se presentan en su estado natural aplicando distintos algoritmos de clasificación de imágenes

- ▪ Calibrar radiométricamente un sensor activo (láser escáner terrestre) para analizar su comportamiento interno y compararle al comportamiento de los sensores pasivos.

- ▪ Analizar las mejoras que la calibración y correcciones radiométricas proporcionan al procesado de datos y resultados finales tanto para el caso de sensores activos como pasivos.

- ▪ Realizar hibridaciones sensoriales con éxito para dar solución al estudio radiométrico de coberturas terrestres cuya caracterización espectral sea característica de un rango espectral muy concreto y estrecho.

- ▪ Detectar y analizar patologías presentes en materiales de construcción para diferentes escenarios a través de la hibridación sensorial y los algoritmos de clasificación de las imágenes.

Establecer las limitaciones, necesidades y factores implicados en la adquisición y el estudio de datos multiespectrales dependiendo del tipo de sensor y plataforma utilizados.

1.4. Estructura de la Tesis Doctoral

Esta Tesis Doctoral se presenta en la modalidad de "compendio de artículos científicos" publicados en revistas internacionales de impacto de conformidad con el Reglamento de Doctorado de la Universidad de Salamanca. Consta de cinco artículos: cuatro publicados en revistas internacionales de alto impacto y uno publicado como capítulo de libro.

La Tesis Doctoral se organiza en cinco capítulos que siguen el orden lógico de investigación de acuerdo con los objetivos establecidos:

- ▪ Capítulo I: Introducción.

- ▪ Capítulo II: Calibración radiométrica vicaria de un sensor multiespectral.

- ▪ Capítulo III: Imágenes multiespectrales aplicadas al campo de la geología.

- ▪ Capítulo IV: Hibridación sensorial aplicada a los campos de la ingeniería civil y del patrimonio cultural.

- ▪ Capítulo V: Conclusiones generales.

Además, se han considerado dos apéndices de forma adicional. El Apéndice A que proporciona información sobre el factor de impacto de las revistas en las que los trabajos han sido publicados y el Apéndice B que resume las principales características y opciones del software MULRACS (propiedad intelectual registrada SA − 00/2015/4722) desarrollado por los autores para facilitar la calibración radiométrica de los sensores pasivos.

A continuación se detalla el contenido incluido en cada capítulo y la relación que existe entre los distintos capítulos de la tesis:

Capítulo I: Este capítulo sirve de capítulo introductorio y ofrece una visión general del estado del arte actual sobre el análisis multiespectral de imágenes desde la perspectiva más frecuente de la teledetección, pasando por las imágenes aéreas a través de vehículos aéreos hasta los estudios de corto alcance realizados a nivel terreno. También se establece el objetivo general y los objetivos específicos del trabajo de investigación y finalmente se concluye con la organización y la estructura de los capítulos restantes.

Capítulo II: Este capítulo actúa de marco de referencia para el resto de capítulos debido a que en él se trata la calibración radiométrica y se resuelve para el caso de una cámara multiespectral de bajo coste (la Mini MCA-6 de Tetracam®), sensor que se usa en el resto de estudios

posteriores. Los motivos por los que se decidió elegir este tipo de sensor, el campo de aplicación en el que fue analizado, la plataforma y la distancia de estudio están justificados dentro de este capítulo. Para finalizar, señalar que el proceso de calibración radiométrico se llevó a cabo gracias al software de calibración MULRACS (véase el Apéndice B) desarrollado por los autores para tal fin.

Capítulo III: Este capítulo está motivado por la realización de una estancia de colaboración en la Universidad Tecnológica de Delft (Países Bajos). Debido al interés mostrado por su Departamento de Ingeniería y Ciencias de la Tierra para testear la cámara multiespectral Mini MCA-6 calibrada (Capítulo II) en el reconocimiento de rocas. En este capítulo se desarrollan por tanto los trabajos realizados durante la estancia: la aplicación de este sensor multiespectral para el estudio y caracterización espectral de rocas sedimentarias sabiendo a priori que el rango espectral ofrecido por el sensor no era el idóneo para el caso de estudio planteado. De esta manera se analizaron sus potenciales y limitaciones al respecto.

Capítulo IV: Una vez conocido el comportamiento radiométrico de la cámara multiespectral de bajo coste y conocidos también su potencial y limitaciones derivados de su uso en diferentes coberturas y escenarios, en este capítulo se apuesta por la hibridación sensorial como herramienta para llevar a cabo análisis espectrales más completos aplicables a una gama más amplia de áreas de estudio. Concretamente, se propone el uso conjunto de la Mini MCA-6 junto a otros sensores activos y pasivos de cara a profundizar en el estudio de del funcionamiento radiométrico de sensores con distintos principios de funcionamiento y en el estudio de distintas técnicas de procesamiento de datos para la optimización de los resultados. El objetivo final consiste en conseguir una herramienta eficaz con la que sea posible realizar estudios espectrales de mayor variedad de superficies terrestres.

En este caso, y como se verá a través de los tres subcapítulos establecidos, la fusión sensorial se centra en la detección de humedades y otras patologías presentes en construcciones tanto civiles como del patrimonio cultural.

IV.1: Este subcapítulo aborda el tema de la hibridación sensorial de dos sensores calibrados radiométricamente y con principios de funcionamiento diferentes, un láser escáner activo y la cámara multiespectral de bajo coste analizada en los Capítulos II y III. Las imágenes multiespectrales de la Mini MCA-6 se combinaron con los datos de intensidad del láser escáner terrestre FARO Focus-3D® para la documentación espectral de una fachada con presencia de humedad. Gracias a la geometría 3D proporcionada por el láser fue posible crear ortoimágenes verdaderas y, por tanto, realizar análisis cuantitativos de las patologías detectadas. Finalmente, se señalan las ventajas y desventajas derivadas del uso de cada uno de los sensores para la detección de humedades subrayando las dificultades intrínsecas al proceso de hibridación.

IV.2: En este subcapítulo se establece un protocolo automático para la detección y mapeo de humedades en estructuras de hormigón. Se plantea la adquisición combinada de datos espectrales a través de cuatro sensores, dos sensores activos y dos pasivos, y el procesado conjunto de sus datos siguiendo una metodología de análisis simplificada. En este caso se decidió llevar a cabo un análisis radiométrico de los datos digitales brutos, sin aplicar la calibración radiométrica, con el fin de estudiar la viabilidad en la automatización del proceso de detección de este tipo de patologías. Tras realizar distintas transformaciones geométricas a los datos y gracias a la escala real que nos ofrece la geometría 3D de los sensores activos, como productos finales se obtienen imágenes clasificadas con propiedades métricas.

IV.3: En este subcapítulo se aborda la fusión sensorial de forma teórica y orientada al análisis multiespectral de patologías presentes en las construcciones en general. Se establecen por tanto los fundamentos, principios y métodos de adquisición y procesamiento de datos para tal fin.

Capítulo V: Esta tesis se cierra con la discusión y análisis de los principales resultados y conclusiones alcanzadas durante su desarrollo. También se establecen diferentes enfoques y líneas futuras abiertas a la continuidad de esta línea de investigación.

Chapítulo II

CALIBRACIÓN RADIOMÉTRICA VICARIA DE UN SENSOR MULTIESPECTRAL

2. CALIBRACIÓN RADIOMÉTRICA VICARIA DE UN SENSOR MULTIESPECTRAL

Este capítulo contiene el artículo *Vicarious radiometric calibration of a multispectral camera on board an unmanned aerial system* (Calibración radiométrica vicaria de una cámara multiespectral embarcada en un sistema aéreo no tripulado) publicado en Febrero de 2014 en la revista internacional *Remote Sensing*.

2.1. Resumen

Este artículo describe el procedimiento seguido para calibrar radiométricamente una cámara multiespectral de bajo coste (Mini MCA-6, Tetracam®) a bordo de un sistema aéreo no tripulado y a una altura de vuelo moderada (30 metros). Tanto la calibración como su posterior validación fueron resueltas mediante método vicario basado en radiancias (Slater et al., 1987) y haciendo uso del software MULRACS (apéndice B) desarrollado por los autores para tal fin. El objetivo principal fue determinar la respuesta espectral de la cámara, es decir, conocer la relación entre los datos de entrada (radiación reflejada por cada superficie) y los de salida (niveles digitales). Una vez conocida esta relación, la cámara multiespectral puede usarse para analizar el comportamiento radiométrico de cualquier superficie o material en valores físicos, ya sean radiancias o reflectancias, en lugar de niveles digitales.

El método vicario descrito requiere de: (i) un área de prueba en el que se dispongan varias superficies homogéneas y Lambertianas de interés (naturales y artificiales), (ii) un espectrorradiómetro cuyas mediciones sirvan de verdad terreno y (iii) realizar una adquisición simultánea de las imágenes multiespectrales y los datos con espectrorradiómetro. El espectrorradiómetro es el dispositivo con el que se mide la radiación reflejada (en este caso en valores de radiancia, $W \cdot m^{-2} \cdot sr^{-1} \cdot nm^{-1}$) por cada

superficie de interés y para las longitudes de onda para las cuales es capaz de registrar información de acuerdo con su resolución espectral. Por su parte, la cámara a bordo del sistema aéreo no tripulado captura, para cada una de sus seis bandas espectrales, la radiación reflejada por cada superficie. Esta radiación puede estar alterada por la absorción y dispersión de las partículas en suspensión de la atmósfera (Chan, 1960). Para eliminar la afección e influencia que una columna atmosférica de 30 metros pueda tener sobre la señal de entrada al sensor es necesario conocer algunos datos meteorológicos del momento de la captura (temperatura, espesor óptico, vapor de agua, etc.). Una vez eliminada esta afección, los datos de la cámara y del espectrorradiómetro ambos pueden ser analizados como si se hubieran tomado a la misma altura, sin atmósfera que influya de por medio. De esta manera, para cada banda espectral en la que registra la cámara, el comportamiento radiométrico de cada superficie de interés medido con espectrorradiómetro es comparado con los niveles digitales de salida de la cámara. La relación existente entre ambos valores para cada banda determina los coeficientes de calibración radiométrica de la cámara.

Debido a que los sensores de bajo coste son susceptibles de transmitir ciertos errores sistemáticos a las imágenes finales, el análisis y corrección de estos errores supuso un reto añadido a la calibración radiométrica. En este caso, se estudiaron y corrigieron las imágenes de ruido de fondo y viñeteo para cada una de las seis bandas espectrales. Para finalizar, todos estos aspectos fueron implementados en el software MULRACS y la calibración radiométrica de la cámara fue resuelta por el método de estimación robusto Danés propuesto por Krarup (Krarup et al., 1980).

Este trabajo sirvió por un lado para validar el uso vinilos y lonas de diferentes colores como superficies de calibración de bajo coste y por otro, para que distintas superficies naturales (suelo, paja seca y pinos) fueran utilizados como superficies de validación o chequeo. Nótese la alta correlación obtenida (error promedio del 1.8%) entre las radiancias medidas in situ con espectrorradiómetro calibrado y las obtenidas con la cámara tras su calibración para la superficie de chequeo "pino". Por otra parte, y después de evaluar la influencia atmosférica a través del modelo de transferencia radiativa 6S (modelo más utilizado por la Comunidad

Científica en el campo de la teledetección), se concluye que para una altura de vuelo de 30 metros y un cielo despejado, la influencia atmosférica es insignificante. Esto abre la posibilidad de analizar cualquier superficie terrestre cuya adquisición de datos tenga ciertas limitaciones de punto de vista (como puede ser el caso de las cubiertas forestales y los macizos rocosos), de tal forma que una toma de datos aérea sea una alternativa a las observaciones satelitales, suponiendo una mejora en resolución espacial y temporal. Finalmente se concluye que el software MULRACS garantiza robustez en la calibración radiométrica de sensores pasivos, quedando demostrado por el buen ajuste ($R^2 = 0,98$) que se obtiene de sus resultados.

remote sensing

Article

Vicarious Radiometric Calibration of a Multispectral Camera on Board an Unmanned Aerial System

Susana Del Pozo [1]**, Pablo Rodríguez-Gonzálvez** [1,]*****, David Hernández-López** [2]
and Beatriz Felipe-García [2]

[1] Department of Cartographic and Land Engineering, University of Salamanca, Hornos Caleros, Ávila 05003, Spain; E-Mail: s.p.aguilera@usal.es

[2] Institute for Regional Development (IDR), Albacete, University of Castilla La Mancha, Ciudad Real 13003, Spain; E-Mails: david.hernandez@uclm.es (D.H.-L.); bfelipe@jccm.es (B.F.-G.)

***** Author to whom correspondence should be addressed; E-Mail: pablorgsf@usal.es; Tel.: +34-920-353-500; Fax: +34-920-353-501.

Abstract: Combinations of unmanned aerial platforms and multispectral sensors are considered low-cost tools for detailed spatial and temporal studies addressing spectral signatures, opening a broad range of applications in remote sensing. Thus, a key step in this process is knowledge of multi-spectral sensor calibration parameters in order to identify the physical variables collected by the sensor. This paper discusses the radiometric calibration process by means of a vicarious method applied to a high-spatial resolution unmanned flight using low-cost artificial and natural covers as control and check surfaces, respectively.

Keywords: radiometric calibration; vicarious method; multispectral camera; UAS; low-cost targets; radiance; remote sensing

1. Introduction

Unmanned aerial systems (UASs) are gaining ground in the field of remote sensing as a new and versatile tool for data acquisition. In this sense, the interest of the international scientific community in them is steadily increasing. NASA has been a pioneer in the use of UASs, an example being

agricultural resource monitoring, such as coffee crops [1,2], or the analysis of vineyard crop vigor variables [3], among others.

In comparison with manned aircraft or satellite platforms, UASs provide unique advantages in the data captured: their low operating height enables the generation of data at a very high spatial resolution in small areas [4], up to 1 cm per pixel [5,6]. Furthermore, UAS platforms allow short revisit periods, in contrast to satellite platforms, with their unfavorable orbital coverage patterns [7]. In addition, this high temporal resolution in data capturing [8] and increased maneuverability allow remote data acquisition in small inaccessible areas or in hazardous environments [9]. For these reasons, together with their low operational costs, UASs are becoming a key tool to meet the requirements of satellite imagery and aerial photography users.

The progress of microelectronics in the field of digital sensors, navigation equipment (GNSS/IMU (Global Navigation Satellite System/inertial measurement unit)), along with the design of small aircraft and light-weight materials, has reduced the cost of the fundamental components of UASs [10]. Several authors have published works in which, using cameras on board small planes or radio-controlled helicopters, they have demonstrated the viability of such airborne vehicles as image acquisition platforms for scientific purposes [11–16]. With the increasing availability of commercial, low-cost components, research groups now have the option to develop their own projects based on UASs. Accordingly, they have the possibility of loading sensors with adequate spectral and radiometric resolution to satisfy their own research requirements.

The possibility of working with multispectral cameras on these platforms allows radiometric studies to be carried out. To this end, sensors must undergo a calibration that analyzes the radiometric behavior of each pixel in the different regions of the spectrum in which information has been recorded. This behavior depends on the weather conditions and the characteristics of the sensor [17]. Analyzing and comparing these magnitudes to other field measurements, a vicarious calibration model is achieved [18] following the empirical line approach [19]. As a result, vicarious calibration allows physical quantities to be known in units of radiance ($W\ m^{-2}\ sr^{-1}\ nm^{-1}$) for any pixel from a single image in a particular camera channel. The basis of this behavior is that each body has its own, different reflected/emitted energy pattern that sets it apart from other material when electromagnetic energy impinges on it [20].

This study aims to obtain the calibration parameters of a multispectral camera onboard a UAS using low-cost targets. To achieve this, different natural and artificial surfaces were used to determine radiance accurately at the sensor level through the use of a calibrated radiometer [21]. As result, it was possible to extract quantitative data from the multispectral imaging. Additionally, with the determination of the radiometric calibration parameters, several sensor corrections were applied to improve the data quality [22]. This workflow highlights the advantages, limitations and problems associated with radiometric capture using multispectral remote sensing onboard UASs.

The present work has the following structure and organization. First, the instruments employed are described, together with the flight planning for data gathering (Section 2) and the radiometric and geometric corrections made to the camera (Section 3). We then discuss the proposed calculation process of the radiometric calibration (Section 4). Thirdly, the field campaign of the case study is explained, and the results achieved are analyzed and validated (Section 5). Finally, we outline the conclusions and future work (Section 6).

2. Materials

The instruments employed included a multispectral camera, an aerial platform and the spectroradiometer, which will set the ground truth in the form of radiances over artificial control surfaces and natural check surfaces. In the case of the UAS, the flight planning needs to be considered to optimize the data gathering step.

2.1. Instruments

A Mini-MCA camera with 6 channels was used as the multispectral sensor [23] (Figure 1); its low weight suggested that it was suitable for loading on a UAS. The specifications of the multispectral camera are listed in the following table (Table 1).

Figure 1. Mini-MCA multispectral camera.
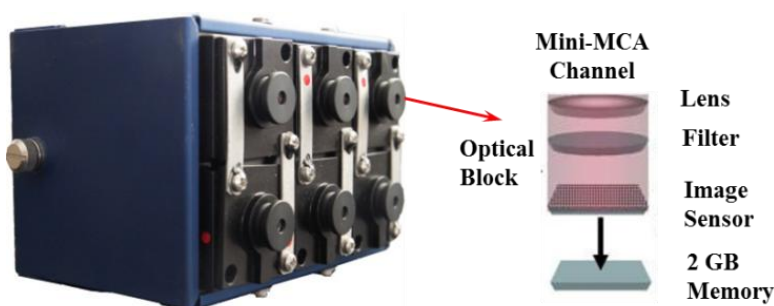
Table 1. Characteristics of the Mini-MCA multispectral camera.

Parameter	Value
Number of channels	6
Weight	700 g
Geometric resolution	1280×1024
Radiometric resolution	10 bits
Speed	1.3 frames/s
Pixel size	5.2 μm
Focal length	9.6 mm

Each of the six channels of the camera is constituted by a CMOS (complementary metal-oxide-semiconductor) sensor and a filter with a pre-set performance against the spectral range. Such filters are characterized by a central wavelength in the range of 531 to 801 nm.

The spectral response of the CMOS is not uniform, due to quantum efficiency and sensitivity. In turn, filters do not have the same transmittance. The combination of CMOS and the 6 filters is reflected by a reduction in the radiance captured by the camera. These responses are defined in the following graphic (Figure 2), according to the manufacturer's data (Andover Corporation; Salem, NH, USA and Tetracam Inc.; Chatsworth, CA, USA).

Figure 2 shows the spectral range covered by the camera (green, red and near-infrared). The exposure time of each filter is different for the same capture and has the following relationship (Table 2):

Figure 2. Complementary metal-oxide-semiconductor (CMOS) and filter spectral performance of the Mini-MCA multispectral camera.
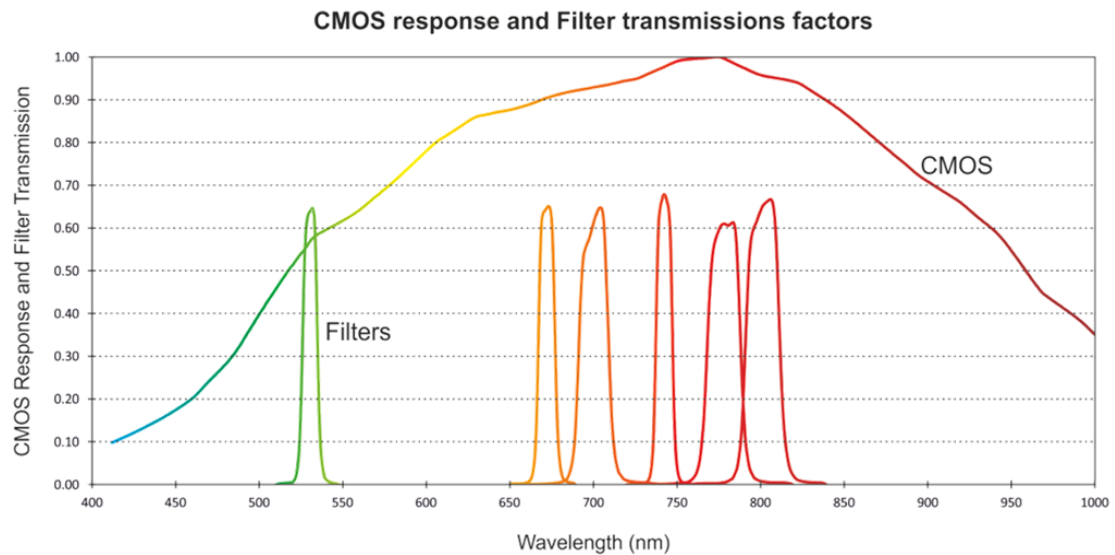
Table 2. Characteristics of the six channels of the camera and their corresponding exposures times.

Channel	λ_{min} (nm)	λ_{max} (nm)	Band Width (nm)	Exposure Time (%)
0	740	820	80	100
1	510	550	40	130
2	650	690	40	125
3	660	740	80	100
4	720	760	40	100
5	760	840	80	100

The unmanned aerial system was an eight-rotor Oktokopter [24] (Figure 3), which has a gimbal stabilized with two degrees of freedom. This multi-rotor has an IMU system with 10 degrees of freedom and a GNSS, thanks to which scheduled flight paths can be established. The most relevant characteristics are specified in Table 3.

Figure 3. Oktokopter.

Table 3. Unmanned aerial systems (UAS) characteristics.

Parameter	Value
Weight without batteries	1880 g
Battery weight (5000 mAh-14.8 V)	540 g
Multispectral camera weight	1025 g
Full system weight	3445 g
Maximum range transmission	1000 m
Recommended range transmission	750 m
Estimated flight time	12 min
Maximum horizontal speed	4 km/h

The spectroradiometer used to carry out the calibration was the FieldSpec 3 ASD (Analytical Spectral Devices) spectroradiometer. This is a general-purpose spectroradiometer used in different areas of application that require reflectance, transmittance, radiance and irradiance measures, and it is especially designed to acquire spectral measurements in the visible to short-wave infrared range.

The spectroradiometer is a compact, portable instrument that allows one to capture spectral data in the region from 350 nm to 2500 nm, with a spectral resolution of 1 nm. The spectroradiometer is configured by three detectors, separated by appropriate filters to eliminate the light of lower orders. The electromagnetic radiation projected onto a holographic diffraction grating is captured through an optical fiber. This grid separates and reflects wavelength components, to be measured independently by detectors. The visible/near-infrared (350–1000 nm) portion of the spectrum is measured by a 512-channel silicon photodiode array overlaid with an order separation filter. The short-wave infrared (SWIR) portion of the spectrum is acquired with two scanning spectrometers: for wavelength ranges of 1000–1830 nm and 1830–2500 nm. Each SWIR spectrometer consists of a concave holographic grating and a single thermo-electrically cooled indium gallium arsenide (InGaAs) detector with a 2-nm sampling interval.

The incoming light to the device is captured through a 3-m optical fiber, whose field of view (FOV) is modified by various foreoptics.

2.2. Flight Planning

Proper planning of UAS flights is an important aspect in order to ensure that the data capture fits the theoretical parameters and user requirements pursued and optimizes the available resources. Furthermore, risks to humans are avoided, and higher quality images can be obtained.

This planning takes into account all the limitations and restrictions that are required by the final images themselves to meet the objectives of the study, acting as a guarantee in the photo capture process. The values that can be specified include the position and attitude of the camera, the flight path, the design of the different image blocks, the determination of the overlaps between the different images, the required camera angles, the scale (through the choice of the pixel size on the ground (GSD (Ground sampling distance)) and control of the time of flight, among others. The theoretical GSD value, which sets the geometric resolution of the study, is defined as:

$$GSD = \frac{h \times S}{f} \tag{1}$$

where *h* is the flight height, *S* the pixel size and *f* the camera focal length.

One of the most important factors is the overlap between images, since this will ensure greater robustness of the geometry captured, determining the image orientations and the reconstruction of the object with greater accuracy and reliability [25]. A UAS flight without the proper flight planning will merely lead to a waste of resources, since the local topography will modify the theoretical flight parameters (GSD, forward and side overlap, *etc.*), causing them to move away from optimal values. A local increase in height in the study area will lead to a higher spatial resolution (a decrease in *h*), but also decrease in image overlap, and gaps may appear between the strips.

For this study, the planned flight was carried out (Figure 4) with a flight height of 30 m and a GSD of 16 mm, allowing the radiometric calibration of the camera to be resolved correctly. The flight path was calculated with the UFLIP (UAS Flight Planning) software (developed by the Tidop research group), which allows the above photogrammetric flight planning parameters to be taken into account.

Figure 4. Photogrammetric flight planning using an orthoimage of the study area.

3. Multispectral Camera Correction

The use of a multispectral sensor requires a series of corrections prior to the radiometric calibration process: background error and vignetting. Furthermore, an additional geometric correction (geometric calibration) necessary for correct channel fusion is considered. All these corrections are determined in a single laboratory analysis and only need to be checked periodically to ensure their stability or when the camera is modified.

3.1. Background Error Correction

Image noise sources can be classified as signal-dependent noise (photon shot noise) and signal-independent noise (dark current, amplifier noise, quantization error) [26]. Some of these noise sources, such as the quantization error, may be negligible, as long as the noise does not exceed the

quantization interval of the ADC (Analog to Digital Converter). However, a multispectral camera may be affected by non-random errors [27], which will degrade the final image quality.

This study analyzed the background error recorded by the camera, whose bimodal behavior was different for each channel and more pronounced on high-reflectance surfaces and is not related to the random noise caused by the sensor electronics (dark current). The systematic error has two configurations: on the one hand, a series of periodic horizontal bands, due to the blockage of the diaphragm; and on the other hand, a pseudo-texture in the distribution of digital levels. This systematic error is assessable in a completely dark room in the absence of light, where only the random noise component is to be expected.

To eliminate both effects, a laboratory analysis was undertaken in the absence of light, evaluating the average response of the camera per channel under different exposure times. The maximum background error for this study involved a 0.49% increment in the digital level value.

3.2. Vignetting

The term vignetting refers to the effect of the brightness attenuation of an image as we depart from its principal point radially. This phenomenon occurs due to the effective size of the camera lens aperture. Vignetting is decreased proportionally to lens aperture (or inversely to the f-number). Furthermore, vignetting is related to the focal length, since the angle of the light incidence on the sensor causes a dimming, such that wider-angle lenses are more affected by this phenomenon.

Since this condition affects the image radiometry, it was corrected to ensure that each pixel would contain the correct digital level. The study was conducted in a laboratory, with uniform illumination, acquiring a series of photographs of a white pattern with low-specular reflection [27,28] (Figure 5).

Figure 5. (**a**) NIR image of vignetting study; (**b**) 3D vignetting representation of Channel 6.

(**a**)   (**b**)
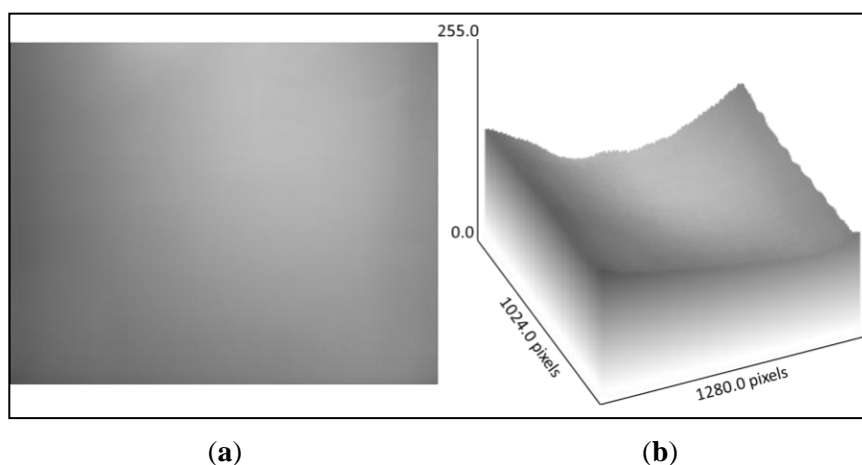
3.3. Geometric Distortion

Geometric distortion caused by the camera lens can be considered as a supplementary aspect to the radiometric calibration process. Moreover, the processing of geometric distortion involves an alteration of digital levels, due to the resampling process, and hence, its correction (direct or reverse) should be carried out in the final stage.

The goal is to determine the geometric (principal point coordinates, x_p, y_p, and principal distance, f) and physical (radial and tangential distortion) parameters that define the internal orientation of the camera, using a laboratory calibration.

This aim can be achieved thanks to a protocol in which image shots are convergent to a pattern or grid of known dimensions and by applying the collinearity, which relates image points with ground points. In particular, an open source tool, Bouguet [29], was used. More specifically, a set of images with a planar checkerboard pattern were acquired under different roll and pitch angles. The images ensured that the pattern covered the largest area of the image in order to model the geometric distortions without extrapolations.

Table 4 shows the results of the 6-sensor camera (Tetracam Mini-MCA) calibration, expressed in the balanced model [30]. This distortion model fits the effect of radial distortion (Δr) through the coefficients, a_0, a_1 and a_2, whereas the coefficients, P_1 and P_2, model the tangential component (Δt), according to the mathematical model of Equation (2):

$$\Delta r = a_0 r' + a_1 r'^3 + a_2 r'^5$$
$$\Delta t_x = P_1 \left(r'^2 + 2\left(x' - x_p\right)^2 \right) + 2P_2 \left(x' - x_p\right)\left(y' - y_p\right)$$
$$\Delta t_y = P_2 \left(r'^2 + 2\left(y' - y_p\right)^2 \right) + 2P_1 \left(x' - x_p\right)\left(y' - y_p\right)$$

(2)

where r' stands for the radial distance of the real image (in contrast to the radial image of the ideal or undistorted image). The coefficients, a_0, a_1 and a_2, are functions of the radial distance from the principal point of symmetry. Additional information about the geometric calibration can be found in [31].

Table 4. Radial and tangential distortion parameters of the six MCA channels.

Channel	Balanced Principal Distance (mm)	Radial Distortion			Tangential Distortion	
		a_0	a_1	a_2	P_1	P_2
778 nm	9.971	0.01508	−0.00234	6.16E−05	1.45E−04	−2.74E−04
530 nm	9.849	0.01560	−0.00231	5.01E−05	2:06E−05	−1.31E−04
672 nm	9.961	0.01556	−0.00177	−1.55E−05	1.57E−04	−4.82E−04
700 nm	9.945	0.01464	−0.00206	3.35E−05	3:20E−04	−2.44E−04
742 nm	9.974	0.01817	−0.00184	−4.55E−05	5.41E−05	−1.79E−04
801 nm	9.955	0.01648	−0.00178	−2.85E−05	−1.02E−05	−1.37E−04

The differences in construction between the sensors are also shown in Figure 6, where the maximum discrepancy reaches 18 pixels, illustrating the relevance of this geometric correction for individual image fusion.

Since the multispectral camera has six non-collinear objectives, the image fusion has to take into account, not only the calculated intrinsic camera parameters (specific for each sensor), but also the extrinsic parameters of the sensors; the three-axis orientation and spatial position. The distance, or baseline, among the optical centers of the sensors will cause a parallax [32] in the image fusion. This effect can usually be neglected in real applications (due to the height of the flight). However, for

laboratory experiments or very low flights, this parallax can be considered by resampling the images according to the coefficients of the fundamental matrix [33].

Figure 6. Graphic representation of geometric distortion of the six channels of the MCA.
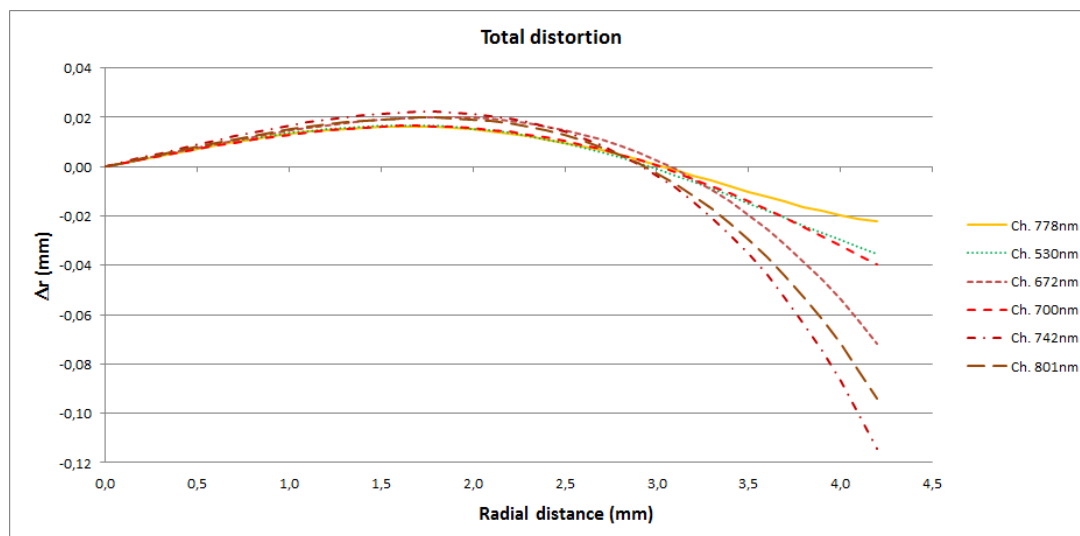
4. Radiometric Calibration

4.1. Calibration Method

Analyses derived from data captured by multispectral cameras require previous knowledge of the radiometric calibration parameters of each channel. According to Dianguirard and Slater [34], radiometric calibration processes can be classified as:

- Laboratory calibration before the flight (preflight calibration). This procedure involves a rigorous calibration of sensors.
- Satellite or airborne calibration (onboard calibration), implementing checks during image acquisition. Lamps or solar-diffuser panels are used in this kind of calibration.
- Calibration through *in situ* measurement campaigns (vicarious calibration). This entails an absolute radiometric calibration in flight conditions other than those found in the laboratory. Within this modality, the absolute method based on radiance or reflectance is included.

The radiance-based method is theoretically more accurate, and its uncertainty is approximately 2.8% *versus* 4.9% for the reflectance-based method [35]. This low value arises from the calibration and stability of the spectroradiometer required for calibration [34].

Among the different calibration methodologies, we chose a vicarious calibration based on the absolute radiance method (Figure 7), considering that the digital level that defines each pixel has a direct relationship with the radiance detected by the sensor [27,36].

Thus, for each spectral channel of the camera, a linear model is established that relates the digital level to the radiance captured by the sensor.

Radiometric calibration processes require homogeneous and Lambertian surfaces. Among the possible materials that could function as control surfaces, we chose low-cost elements: a canvas with 6 different tones of grey and 6 PVC (polyvinyl chloride) vinyl sheets with different colors.

Figure 7. Workflow of the radiometric calibration process.
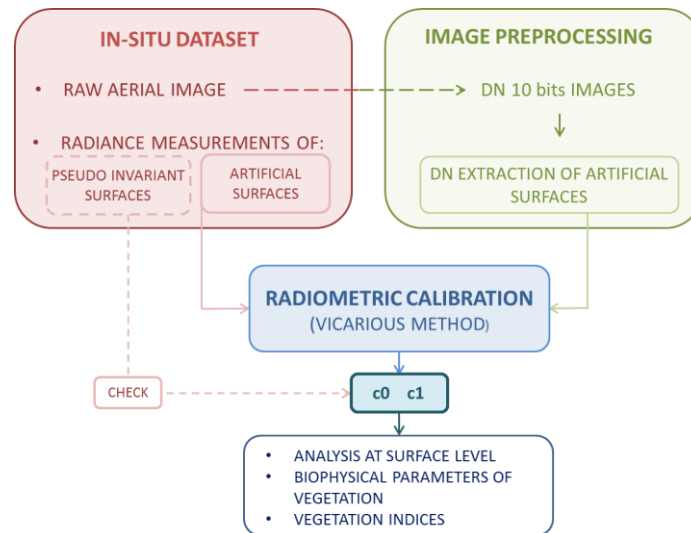
For this calibration workflow, artificial targets were chosen instead of pseudo-invariant features, since they have proven to be more appropriate [18,37,38]. The critical factor for this selection is the requirement of uniform reflectivity with respect to the viewing direction and wavelength [38]. In the case of pseudo-invariant objects, these are not suitable, because their radiometric properties change over time [39,40]. Pseudo-invariant features were only employed as check surfaces.

Digital levels (DL) of artificial targets are extracted from the aerial images to calculate the relationship between them and the radiance of the surfaces (obtained with the spectroradiometer). The simplified radiative transfer model is defined according to the following equation:

$$L_{sensor} = c_0 + c_1 \times DL \tag{3}$$

Since several images are involved in the calibration adjustment, a luminance homogenization factor between photos was taken into account. This factor absorbs exposure differences (due to changes in lighting between different shots) and the inherent shutter time of each channel.

$$L_{sensor} = c_0 + c_1 \times DL \times F_h \tag{4}$$

where c_0 and c_1, offset and gain, are the calibration coefficients of each camera channel. The variable, F_h, is the homogenization factor of digital levels, defined as follows,

$$F_h = \frac{F_{eq}}{F_v} \tag{5}$$

where F_{eq} is the exposure factor and F_v the shutter opening time factor.

Furthermore, because the images are affected by different types of radiometric distortion generated by the sensor (see Section 3), these corrections were taken into account in adjustment Equation (5), obtaining the final calibration model:

$$L_{sensor} = c_0 + c_1 \times DL \times F_h \times R(x, y) \times V(x, y) \tag{6}$$

where R is the systematic background error correction and V the vignetting correction; both variables are functions of the pixel position in the image.

In classical aerial photogrammetry, aiming at the determination of physical parameters at the surface level and not at the sensor level, the 6S atmospheric model [41] has been applied. The modeling of the influence of the atmosphere on the propagation of radiation for a height of 1 m (spectroradiometer data captured) and 30 m (UAS flight height) shows no discrepancy. More specifically, the difference has an order of magnitude of $<1 \times 10^{-9}$ W cm^{-2} sr^{-1} nm^{-1}. Therefore, it could be suggested that in UAS photogrammetry, the influence of the surface to sensor component of the atmosphere is minimal, since radiation passes through a very small atmospheric column. Due to its reduced value, the relative atmospheric correction can be neglected in the adjustment model, as reported in [42].

Finally, the results of the radiometric calibration process were validated by checking the surface: natural covers, such as vegetation, soil-covered land and bare soil.

4.2. Fitting Model

From multiple artificial targets collected in several images, a least squares adjustment was applied.

A robust estimation was chosen instead of an ordinary least squares (OLS) method, since OLS is highly sensitive to outliers, because real measurements of error distributions have larger tails than the Gaussian distribution [43]. In our case, we chose the Danish Method proposed by Krarup [44], which, applied iteratively, gives a series of weights according to the residual values of the previous iteration.

In the first iteration, the weight matrix, **W**, is set as the identity matrix:

$$w_{ii} = 1 \; ; \; w_{ij} = 0 \;\; with \; i \neq j$$
$$x = (\mathbf{A}^T \cdot \mathbf{W} \cdot \mathbf{A})^{-1} \cdot (\mathbf{A}^T \cdot \mathbf{W} \cdot \mathbf{K}) \tag{7}$$

where x is the vector of calibration coefficients, **A** is the design matrix (digital levels) and **K** is the matrix of independent terms (radiance). The residual vector v is:

$$v = \mathbf{A} \times x - \mathbf{K} \tag{8}$$

whose *a posteriori* variance is:

$$\hat{\sigma}^2 = \frac{v^T \times \mathbf{W} \times v}{m - n} \tag{9}$$

where m is the number of equations and n the total number of unknowns.

From the first adjustment of residuals, new weights are calculated individually for each equation, based on the following weight function of the Danish estimator:

$$w(v_i) = \begin{cases} 1 & for \; |v_i| \leq 2\sigma \\ ke^{-cv_i^2} & for \; |v_i| > 2\sigma \end{cases} \tag{10}$$

where c is a constant that varies between 2 and 3, depending on the redundancy of the adjustment and data quality.

The convergence selection criterion of the iterative process is established based on the fulfillment of one of the following conditions:

- Standard deviation estimator < 0.001;
- Change in variance < 0.01;
- When there are more than 20 iterations.

In the adjustment, an additional unknown was added per image to the x vector to absorb the heterogeneity regarding the possible variations in irradiance between images; this is more likely to occur in unstable weather conditions.

5. Experimental Results

5.1. Radiometric Campaign

The study area is located in Gotarrendura, a village close to Avila (Castilla y León, Spain). Data collection was carried out on 27 July 2012, on a pine plot of 2.52 ha, which was overflown at a height of 30 m. The pine species was *Pinus pinaster*, with a density of 1330 trees per hectare and a height between 1.5 and 2.1 m.

As control surfaces, a 5 m × 1 m greyscale canvas (GS) and six 0.55 m × 0.35 m vinyl sheets of different colors (red, gray, white, black, blue and green) were selected, similar to [42]. These artificial surface sizes guaranteed at least 21 pixels (up to 61 pixels), which exceeds the minimum of three times the GSD to rule out neighbor effects. The check surfaces, corresponding to natural covers (pseudo-invariant features), are highlighted with the yellow, orange and red circles in Figure 8.

Figure 8. Aerial image of the control and check surfaces.

The low-cost colored artificial targets provide a transportable test field as an alternative to a permanent radiometric calibration field. They also avoid the problems of painted targets associated with permanent test fields, caused by environmental conditions [45]. In the radiometric study, calibration surfaces were characterized using the spectroradiometer as a detector of the radiant flux that is reflected from such covers. During data acquisition, it was necessary to take into account that the incidence angle that the spectroradiometer gun formed with the surfaces was as orthogonal as possible, taking two spectral measurements per cover. Prior to each sample measurement, the

calibrated white reference (Labsphere, Inc. Spectralon™, North Sutton, NH, USA) was measured. The spectra were measured in absolute radiance mode. Each spectral measurement is the average result of 120 individual spectra, following the protocol shown in [42].

In parallel, a planned UAS flight was conducted over the study area, capturing multispectral images (Figure 9) and choosing those in which the maximum numbers of control and check surfaces were visible.

Figure 9. An example of a multispectral 10-bit image (sixth channel image, 801 nm).
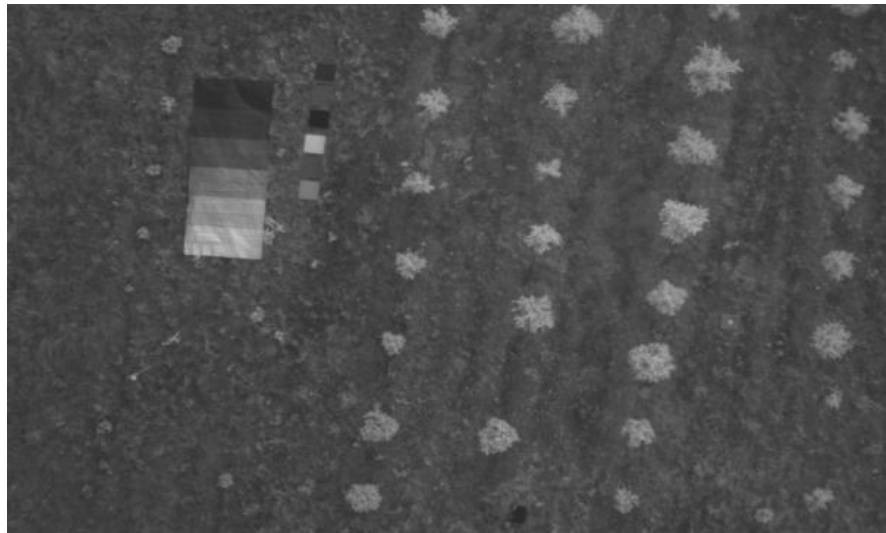
The selected radiance control surfaces were obtained from the spectroradiometer.

Figure 10 shows the spectral signatures of the vinyl sheets used in the radiometric calibration. The reflectance of these surfaces was obtained as the ratio between the reflected radiance of each cover and the radiance of a white reference target (Spectralon 99%), both measured with the spectroradiometer.

Figure 10. The spectral signature of the control surfaces (vinyl sheets) used in the radiometric calibration process.
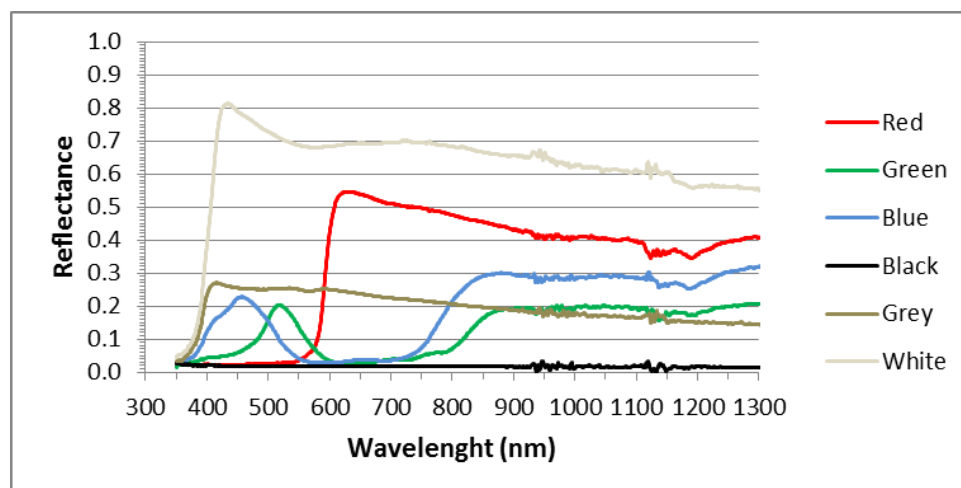
To compare the radiometric measurements with digital levels, it is important to note that the radiance obtained with the radiometer lies between the 350 and 2500 nm spectral range with a 1-nm resolution, whereas the Mini-MCA is capable of recording digital levels in its six channels, each one

characterized by a particular response (Figure 2), due to the differential responses of the filter and CMOS at each wavelength. Therefore, it was necessary to adapt and standardize the radiometric measurements to the spectral resolution of the camera, together with the camera spectral response (R_C). The spectral camera response includes the CMOS response, as well as the filter transmission function. Equation (11) shows the integration process for the measured reflectivity (ρ) of a target (t) with a white reference panel:

$$\rho_t(\lambda) = \frac{\int_{\lambda_1}^{\lambda_2} \rho_t(\lambda) R_C(\lambda) d\lambda}{\int_{\lambda_1}^{\lambda_2} R_C(\lambda) d\lambda} \tag{11}$$

The equation was also applied to obtain the target radiance values involved in the calibration model (Equation (6)).

5.2. Analysis and Validation of Results

The Radiometric Calibration was resolved with the support of software developed for this purpose in MATLAB.

The control surfaces used have a typical radiance response for each of the multispectral camera channels, and based on these, the vicarious calibration relationship was established. The following figure (Figure 11) shows this feature for each of the control surfaces used in the calibration process.

Figure 11. Average radiance for artificial targets. GS, greyscale canvas.
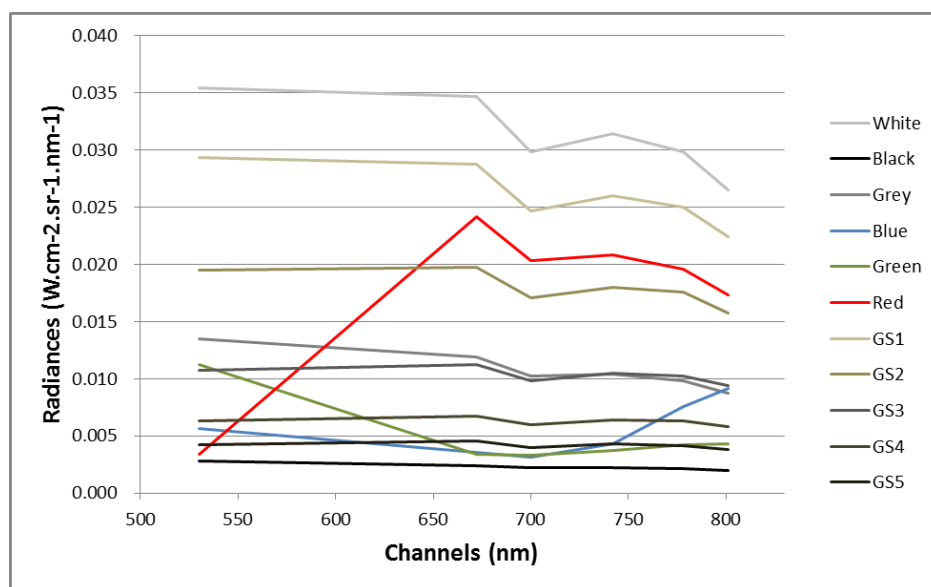
Regarding the radiometric calibration parameters for an altitude of 30 m for each of the six channels of the Mini-MCA onboard the UAS, Table 5 shows the final results of this study. The R^2 fitting coefficient was 0.9833 for a simultaneous block adjustment of six channels. Table 5 also shows the coefficients for the same fitting model, but with an individual channel adjustment. In this second case, the results are fairly similar, as is the determination coefficient, with no significant discrepancies between the two fitting methodologies.

Table 5. Mini-MCA calibration coefficients.

| Channel	Block Adjustment			Individual Channel Adjustment		
	C_0	C_1	R^2	C_0	C_1	R^2
778 nm	−0.000992	0.047175		−0.001510	0.047292	0.9846
530 nm	0.000704	0.057802		0.000264	0.057718	0.9816
672 nm	−0.000307	0.049919	0.9833	−0.000795	0.050005	0.9823
700 nm	−0.000345	0.041242		−0.000861	0.041353	0.9820
742 nm	−0.000688	0.074146		−0.001205	0.074335	0.9843
801 nm	−0.000319	0.047655		−0.000834	0.047656	0.9827

It should be noted that the C_0 value (intercept) is very small (compatible with zero), such that it could be excluded from the calculation.

In this sense, the statistical test used for the validation of the results was the average of the errors in radiance, expressed as percentages (with respect to 10 bits) per control surfaces and per channel (Figure 12).

Figure 12. Average radiance calibration error (percent).
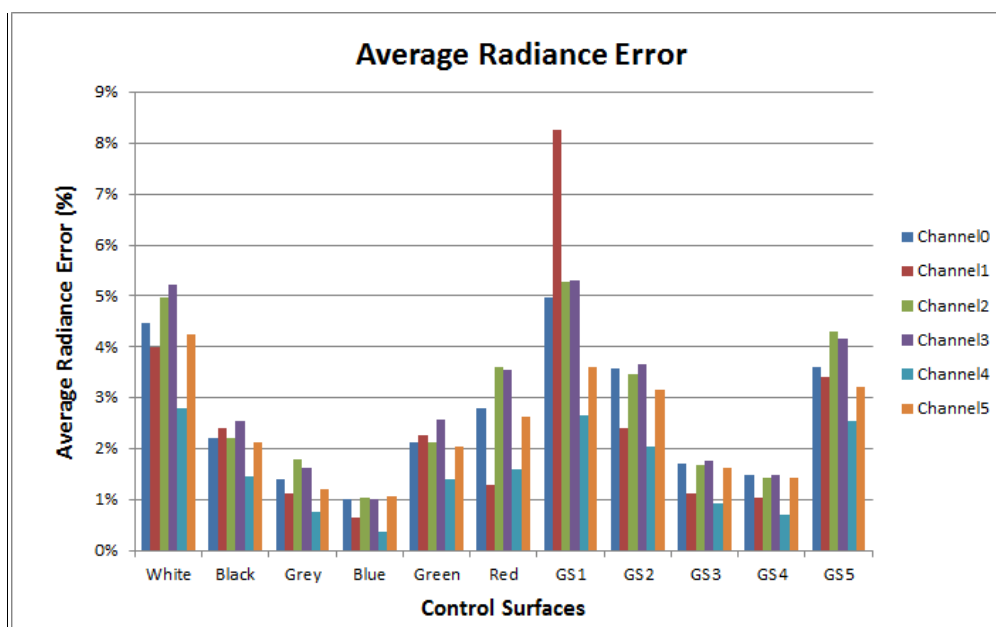
In the above figure, it may be seen that the control surfaces with the greatest error in their radiance estimation are those with the highest reflectance, *i.e.*, the white vinyl and the second lightest color, the greyscale canvas. Furthermore, this error is noteworthy in channel 1 (530 nm), which has the lowest performance, due to the low CMOS response (Figure 2). However, this maximum error means an error of 8%, which can be considered acceptable, since it is an isolated value, as shown in Figure 13, the average residues (2.5%) remaining within the range of error estimated for this calibration mode.

In order to validate the radiometric calibration process, calibration coefficients were applied to the digital levels of natural surfaces to obtain the radiance. The following figure (Figure 13) shows the setting of the radiance measurements considered as "ground truth" (spectroradiometer) for the case of

a pine and their corresponding values obtained after applying calibration coefficients to the pine digital levels.

Figure 13. Pine radiance from the spectroradiometer and from the calibrated Mini MCA.
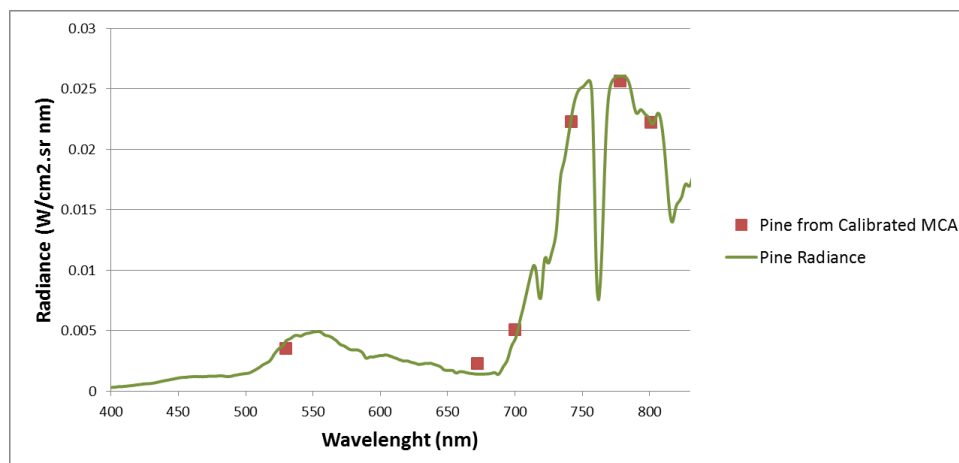
In this case, a strong correlation can be seen between the calculated radiances and *in situ* measurements, it being possible to calculate the pine radiance for each of the six camera channels with a relative error of only 1.8%.

6. Conclusions

This study shows the validity of a vicarious radiance-based calibration for the Mini-MCA onboard a UAS through the use of low-cost covers as control surfaces. The correlation of 0.98 between ground radiance and that derived from the digital level shows the degree of consistency achieved. Furthermore, despite the complexity of the data, the average error of 2.5% is very encouraging.

In addition, after several laboratory and field studies, the validity of using low-cost surfaces for the calibration process was confirmed. Moreover, low-cost covers show an invariant reflectivity for a certain period of time in which they remain unaffected by deterioration.

Another important contribution of high-spatial resolution remote sensing at low flight heights, as provided by this study, is that the relative surface-sensor atmospheric effects on UAS *versus* ground truth measurements are negligible, thus simplifying the workflow.

Finally, in view of the high spatial, spectral and temporal resolution achieved for UAS remote sensors, these platforms can generate high value products at reduced costs as compared to satellite or manned aerial platforms. UAS remote sensing is proving to be a valuable non-invasive technique for the recognition and analysis of different types of strata, crops and rocks, among others. Furthermore, not only qualitative results are obtained, physically relevant quantitative results derived from the digital levels of UAS images can be obtained, as well, and are most relevant.

Acknowledgments

Author Contributions

Susana Del Pozo, Pablo Rodríguez-González, David Hernández-López and Beatriz Felipe-García acquired the data in the radiometric field campaign. David Hernández-López and Beatriz Felipe-García aided with the research design and results interpretation. Susana Del Pozo processed the data, implemented the mathematical model and interpreted the results. Susana Del Pozo and Pablo Rodríguez-González carried out the camera corrections. Susana Del Pozo, Pablo Rodríguez-González and David Hernández-López wrote the manuscript.

Conflicts of Interest

The authors declare no conflict of interest.

References

1. Herwitz, S.R.; Dunagan, S.; Sullivan, D.; Higgins, R.; Johnson, L.; Jian, Z.; Slye, R.; Brass, J.; Leung, J.; Gallmeyer, B.; *et al.* Solar-Powered UAV Mission for Agricultural Decision Support. In Proceedings of the 2003 IEEE International Geoscience and Remote Sensing Symposium (IGARSS), Worcester, MA, USA, 21–25 July 2003; pp. 1692–1694.
2. Herwitz, S.R.; Johnson, L.F.; Dunagan, S.E.; Higgins, R.G.; Sullivan, D.V.; Zheng, J.; Lobitz, B.M.; Leung, J.G.; Gallmeyer, B.A.; Aoyagi, M.; *et al.* Imaging from an unmanned aerial vehicle: Agricultural surveillance and decision support. *Comput. Electron. Agric.* **2004**, *44*, 49–61.
3. Johnson, L.; Herwitz, S.; Dunagan, S.; Lobitz, B.; Sullivan, D.; Slye, R. Collection of Ultra High Spatial and Spectral Resolution Image Data over California Vineyards with a Small UAV. In Proceedings of the 30th International Symposium on Remote Sensing of Environment, Honolulu, HI, USA, 10–14 November 2003.
4. Dunford, R.; Michel, K.; Gagnage, M.; Piégay, H.; Trémelo, M.L. Potential and constraints of Unmanned Aerial Vehicle technology for the characterization of Mediterranean riparian forest. *Int. J. Remote Sens.* **2009**, *30*, 4915–4935.
5. Scaioni, M.; Barazzetti, L.; Brumana, R.; Cuca, B.; Fassi, F.; Prandi, F. RC-Heli and Structure & Motion Techniques for the 3-D Reconstruction of a Milan Dome Spire. In Proceedings of the 3rd ISPRS International Workshop 3D-ARCH, Trento, Italy, 25–28 February 2009.
6. Hunt, E.R.; Hively, W.D.; Fujikawa, S.; Linden, D.; Daughtry, C.S.; McCarty, G. Acquisition of NIR-Green-Blue digital photographs from unmanned aircraft for crop monitoring. *Remote Sens.* **2010**, *2*, 290–305.

7. Berni, J.; Zarco-Tejada, P.J.; Suarez, L.; Fereres, E. Thermal and narrowband multispectral remote sensing for vegetation monitoring from an unmanned aerial vehicle. *IEEE Trans. Geosci. Remote Sens.* **2009**, *47*, 722–738.

8. Laliberte, A.S.; Rango, A.; Herrick, J.E.; Fredrickson, E.L.; Burkett, L. An object-based image analysis approach for determining fractional cover of senescent and green vegetation with digital plot photography. *J. Arid Environ.* **2007**, *69*, 1–14.

9. Everaerts, J. The Use of Unmanned Aerial Vehicles (UAVs) for Remote Sensing and Mapping. In Proceedings of the International Archives of the Photogrammetry, Remote Sensing and Spatial Information Sciences, Beijing, China, 5–7 July 2008; pp. 1187–1192.

10. Pastor, E.; Lopez, J.; Royo, P. UAV payload and mission control hardware/software architecture. *IEEE Aerosp. Electron. Syst. Mag.* **2007**, *22*, 3–8.

11. Zhao, H.; Lei, Y.; Gou, Z.; Zhang L. The Characteristic Analyses of Images from the UAV Remote Sensing System. In Proceedings of the 2006 IEEE International Conference on Geoscience and Remote Sensing Symposium (IGARSS), Denver, CO, USA, 31 July–4 August 2006; pp. 3349–3351.

12. Esposito, F.; Rufino, G.; Moccia, A. 1st Mini-UAV Integrated Hyperspectral/Thermal Electro-Optical Payload for Forest Fire Risk Management. In Proceedings of the AIAA InfotechAerosp Conference, Rohnert Park, CA, USA, 7–10 May 2007; pp. 653–665.

13. Lambers, K.; Eisenbeiss, H.; Sauerbier, M.; Kupferschmidt, D.; Gaisecker, T.; Sotoodeh, S.; Hanusch, T. Combining photogrammetry and laser scanning for the recording and modelling of the Late Intermediate Period site of Pinchango Alto, Palpa, Peru. *J. Archaeol. Sci.* **2007**, *34*, 1702–1712.

14. Nebiker, S.; Annen, A.; Scherrer, M.; Oesch, D. A Light-Weight Multispectral Sensor for Micro UAV—Opportunities for Very High Resolution Airborne Remote Sensing. In Proceedings of the XXIst ISPRS Congress, Beijing, China, 3–11 July 2008; pp. 1193–2000.

15. Xiang, H.; Tian, L. Development of a low-cost agricultural remote sensing system based on an autonomous unmanned aerial vehicle (UAV). *Biosyst. Eng.* **2011**, *108*, 174–190.

16. Turner, D.; Lucieer, A.; Watson, C. Development of an Unmanned Aerial Vehicle (UAV) for Hyper Resolution Vineyard Mapping Based on Visible, Multispectral, and Thermal Imagery. In Proceedings of the 34th International Symposium on Remote Sensing of Environment, Hobart, Australia, 28–29 June 2011.

17. Biggar, S.F.; Thome, K.J.; Wisniewski, W. Vicarious radiometric calibration of EO-1 sensors by reference to high-reflectance ground targets. *IEEE Trans. Geosci. Remote Sens.* **2003**, *41*, 1174–1179.

18. Hernández López, D.; Felipe García, B.; González Piqueras, J.; Alcázar, G.V. An approach to the radiometric aerotriangulation of photogrammetric images. *ISPRS J. Photogramm. Remote Sens* **2011**, *66*, 883–893.

19. Moran, M.S.; Bryant, R.; Thome, K.; Ni, W.; Nouvellon, Y.; Gonzalez-Dugo, M.P.; Qi, J.; Clarke, T.R. A refined empirical line approach for reflectance factor retrieval from Landsat-5 TM and Landsat-7 ETM+. *Remote Sens. Environ.* **2001**, *78*, 71–82.

20. Chuvieco, E.; Huete, A. *Fundamentals of Satellite Remote Sensing*; CRC Press Inc: Boca Raton, FL, USA, 2009.

21. Honkavaara, E.; Arbiol, R.; Markelin, L.; Martinez, L.; Cramer, M.; Bovet, S.; Chandelier, L.; Ilves, R.; Klonus, S.; Marshal, P.; *et al.* Digital airborne photogrammetry—A new tool for quantitative remote sensing?—A state-of-the-art review on radiometric aspects of digital photogrammetric images. *Remote Sens.* **2009**, *1*, 577–605.

22. Hefele, J. Calibration Expierence with the DMC. In Proceedings of the International Calibration and Orientation Workshop EuroCOW 2006, Castelldefels, Spain, 25–27 January 2006.

23. Tetracam Inc. Digital Camera and Imaging Systems Design—Mini Multiple Camera Array. Available online: http://www.tetracam.com/Products-Mini_MCA.htm (accessed on 6 December 2013).

24. HiSystems GmbH. Mikrokopter. Available online: http://www.mikrokopter.com/en/home (accessed on 6 December 2013).

25. Fernández-Hernandez, J.; González-Aguilera, D.; Rodríguez-Gonzálvez, P.; Mancera-Taboada, J. A new trend for reverse engineering: Robotized aerial system for spatial information management. *Appl. Mech. Mater.* **2012**, *152*, 1785–1790.

26. Li, F.; Barabas, J.; Mohan, A.; Raskar, R. Analysis on Errors Due to Photon Noise and Quantization Process with Multiple Images. In Proceedings of the 44th Annual Conference on Information Sciences and Systems (CISS), Princeton, NJ, USA, 17–19 March 2010; pp. 1–6.

27. Kelcey, J.; Lucieer, A. Sensor correction of a 6-band multispectral imaging sensor for UAV remote sensing. *Remote Sens.* **2012**, *4*, 1462–1493.

28. Zheng, Y.; Lin, S.; Kambhamettu, C.; Yu, J.; Kang, S.B. Single-image vignetting correction. *IEEE Trans. Pattern Anal. Mach. Intell.* **2009**, *31*, 2243–2256.

29. Bouguet, J.-Y. Camera Calibration Toolbox for Matlab. Available online: http://www.vision.caltech.edu/bouguetj/calib_doc/ (accessed on 6 December 2013).

30. Light, D.L. The new camera calibration system at the US Geological Survey. *Photogramm. Eng. Remote Sens.* **1992**, *58*, 185–188.

31. Gonzalez-Aguilera, D.; Gomez-Lahoz, J.; Rodriguez-Gonzalvez, P. An Automatic approach for Radial Lens distortion correction from a single image. *IEEE Sens. J.* **2011**, *11*, 956–965.

32. Kraus, K.; Jansa, J.; Kager, H. *Advanced Methods and Applications*. Dümmler: Bonn, Germany, 1997.

33. Hartley, R.; Zisserman, A. *Multiple View Geometry in Computer Vision*; Cambridge University Press: Cambridge, UK, 2003.

34. Dinguirard, M.; Slater, P.N. Calibration of space-multispectral imaging sensors: A review. *Remote Sens. Environ.* **1999**, *68*, 194–205.

35. Biggar, S.F.; Slater, P.N.; Gellman, D.I. Uncertainties in the in-flight calibration of sensors with reference to measured ground sites in the 0.4–1.1 μm range. *Remote Sens. Environ.* **1994**, *48*, 245–252.

36. Hiscocks, P.D.; Eng, P. Measuring Luminance with a Digital Camera. Available online: http://www.ee.ryerson.ca/~phiscock/astronomy/light-pollution/luminance-notes.pdf (accessed on 6 February 2014).

37. Moran, M.S.; Bryant, R.B.; Clarke, T.R.; Qi, J. Deployment and calibration of reference reflectance tarps for use with airborne imaging sensors. *Photogramm. Eng. Remote Sens.* **2001**, *67*, 273–286.

38. Pagnutti, M.; Holekamp, K.; Ryan, R.; Blonski, S.; Sellers, R.; Davis, B.; Zanoni, V. Measurement Sets and Sites Commonly Used for Characterizations. In Proceedings of the Integrated Remote Sensing at the Global, Regional and Local Scale Denver, Denver, CO, USA, 10–15 November 2002; pp. 159–164.

39. Moran, M.; Clarke, T.; Qi, J.; Barnes, E.; Pinter, P.J., Jr. Practical Techniques for Conversion of Airborne Imagery to Reflectances. In Proceedings of the 16th Biennial Workshop on Color Photography and Videography in Resource Assessment, Weslaco, TX, USA, 29 April–1 May 1997; pp. 82–95.

40. Davranche, A.; Lefebvre, G.; Poulin, B. Radiometric normalization of SPOT-5 scenes: 6S atmospheric model *versus* pseudo-invariant features. *Photogramm. Eng. Remote Sens.* **2009**, *75*, 723–728.

41. Vermote, E.F.; Tanre, D.; Deuze, J.L.; Herman, M.; Morcette, J.J. Second simulation of the satellite signal in the solar spectrum, 6S: An overview. *IEEE Trans. Geosci. Remote Sens.* **1997**, *35*, 675–686.

42. Hernández-López, D.; Felipe-García, B.; Sánchez, N.; González-Aguilera, D.; Gomez-Lahoz, J. Testing the radiometric performance of digital photogrammetric images: Vicarious *versus* laboratory CALIBRATION on the Leica ADS40, a study in Spain. *Photogramm. Fernerkund. Geoinf.* **2012**, *2012*, 557–571.

43. Triggs, B.; McLauchlan, P.F.; Hartley, R.I.; Fitzgibbon, A.W. Bundle Adjustment—A Modern Synthesis. In *Vision Algorithms: Theory and Practice*; Springer: Berlin, Germany, 2000; pp. 298–372.

44. Krarup, T.; Juhl, J.; Kubik, K. Götterdammerung over Least Squares Adjustment. In Proceedings of the XIV Congress of International Society of Photogrammetry, Hamburg, Germany, 13–25 July, 1980; pp. 369–378.

45. Honkavaara, E.; Peltoniemi, J.; Ahokas, E.; Kuittinen, R.; Hyyppa, J.; Jaakkola, J.; Kaartinen, H.; Markelin, L.; Nurminen, K.; Suomalainen, J. A permanent test field for digital photogrammetric systems. *Photogramm. Eng. Remote Sens.* **2008**, *74*, 95–106.

Capítulo III

IMÁGENES MULTIESPECTRALES APLICADAS A ESTUDIOS GEOLÓGICOS

3. IMÁGENES MULTIESPECTRALES APLICADAS A ESTUDIOS GEOLÓGICOS

Este capítulo contiene el artículo *Discrimination between sedimentary rocks from close-range visible and very-near infrared images* (Distinción de rocas sedimentarias mediante imágenes de rango cercano en el rango visible e infrarrojo cercano del espectro) publicado en Julio de 2015 en la revista internacional *Plos One*.

3.1. Resumen

El objetivo de este artículo consistió en validar el uso de la cámara Mini MCA-6 calibrada (ver Capítulo II) para estudiar y diferenciar distintos tipos de rocas sedimentarias dispuestas en su estado natural. La principal dificultad de esta investigación radica en validar el uso de un rango espectral no idóneo, ofrecido por la cámara multiespectral (visible e infrarrojo cercano), para el análisis espectral de cubiertas rocosas, caracterizables en el rango infrarrojo de onda corta del espectro (Hunt, 1982). Mediante el análisis multiespectral de un conjunto de 12 formaciones geológicas con diferentes porcentajes de calizas, margas y areniscas de la región de Ródano-Alpes, en Francia, se evaluó el potencial y las limitaciones vinculadas a esta cámara para la diferenciación de rocas sedimentarias.

La firma espectral es característica e inherente a cada material y muestra de forma gráfica cómo interactúa la energía electromagnética con la materia en términos de radiación reflejada. En concreto, representa la cantidad de energía reflejada por la superficie de un material (en términos de porcentaje) para cada longitud de onda del espectro. Dado que el objetivo consistía en encontrar diferencias significativas entre los 12 tipos de formaciones geológicas para el rango espectral ofrecido por la cámara, las imágenes capturadas en niveles digitales debían ser convertidas a valores de reflectancia (ρ). Para ello, fue necesario no sólo

conocer los parámetros de calibración de la cámara para cada banda (offset y gain, $c0$ y $c1$ respectivamente), sino también la irradiancia solar en el momento de la adquisición (E, $W \cdot m^2 \cdot sr^{-1} \cdot nm^{-1}$). Estos parámetros se relacionan con la reflectancia y la radiancia (L) según la Ecuación 2 siguiendo la hipótesis Lambertiana. La irradiancia solar fue obtenida gracias al uso de un Spectralon®, un panel de reflectancia conocida y calibrada en laboratorio (Bruegge et al., 2001). Se colocó el Spectralon® en cada afloramiento de tal forma que apareciera en todas las imágenes multiespectrales realizadas a los macizos rocosos. Dado que la reflectancia es el ratio entre la radiancia y la irradiancia solar (Equation 2), y dado que tanto la reflectancia como la radiancia reflejadas por el panel calibro son conocidos, la irradiancia puede ser calculada a través de la Ecuación 3. Una vez la irradiancia solar es conocida, es posible transformar los niveles digitales (DL) a reflectancias.

$$E = \frac{L}{\rho} \cdot \pi = \frac{c0 + c1 \cdot DL}{\rho} \cdot \pi \qquad (3)$$

Una vez se tiene el conjunto de imágenes multiespectrales en valores de reflectancia, comienza el proceso de análisis para evaluar la capacidad discriminatoria de la cámara en el campo de la geología.

En primer lugar, se obtuvieron las firmas espectrales de los tres tipos de roca sedimentaria (arenisca, caliza y marga) de las que se componían los 12 tipos de formaciones geológicas. Posteriormente, se llevó a cabo una clasificación supervisada de las imágenes aplicando el algoritmo de máxima verosimilitud y en base a los resultados de las firmas espectrales obtenidas. Cuatro clases informacionales fueron evaluadas: caliza, marga, vegetación y sombras. La arenisca fue excluida del proceso de clasificación dado que su firma espectral se superpone a la firma de la piedra caliza en el rango espectral visible e infrarrojo cercano.

Tras analizar los resultados se concluye que la cámara multiespectral Mini MCA-6 es capaz de encontrar diferencias espectrales entre dos de los tres tipos de roca analizada, entre calizas y la margas, no siendo posible en la actualidad diferenciar entre calizas y areniscas. Hay que señalar que los resultados de firmas espectrales obtenidos para los tres tipos de roca son consistentes con el comportamiento espectral de sus

composiciones minerales y tamaños de grano. Si bien es cierto, que añadido al hecho de que el rango espectral de esta cámara no es el adecuado para realizar estudios espectrales de rocas, existen otro tipo de dificultades asociadas al estudio de este tipo concreto de cobertura. Los afloramientos rocosos suelen tener superficies heterogéneas que causan variaciones en la reflexión de la radiación que incide sobre ellas. Además, esta geometría superficial favorece la creación de sombras que son capturadas por la cámara. Es por ello que para el estudio de este tipo de coberturas se recomienda realizar la toma de datos en días nublados donde la luz es lo más difusa posible y se favorece la transición progresiva entre zonas bien iluminadas y zonas en sombra. De esta forma se conseguirían análisis más exhaustivos y resultados más consistentes.

Finalmente se concluye que tanto: (i) la hibridación sensorial entre esta cámara multiespectral y otro sensor capaz de adquirir información espectral en el rango infrarrojo de onda corta como (ii) el estudio de la función de distribución de reflectancia bidireccional (BRDF) de este tipo de cubiertas redundaría en análisis exitosos y completos para el caso de afloramientos rocosos.

Discrimination between Sedimentary Rocks from Close-Range Visible and Very-Near-Infrared Images

Susana Del Pozo[1], Roderik Lindenbergh[2], Pablo Rodríguez-Gonzálvez[1], Jan Kees Blom[2], Diego González-Aguilera[1]*

1 Department of Cartographic and Land Engineering, University of Salamanca, Polytechnic School of Avila, Avila, Spain, 2 Department of Geoscience and Remote Sensing, Delft University of Technology, Delft, The Netherlands

* daguilera@usal.es

Abstract

Variation in the mineral composition of rocks results in a change of their spectral response capable of being studied by imaging spectroscopy. This paper proposes the use of a low-cost handy sensor, a calibrated visible-very near infrared (VIS-VNIR) multispectral camera for the recognition of different geological formations. The spectral data was recorded by a Tetracam Mini-MCA-6 camera mounted on a field-based platform covering six bands in the spectral range of 0.530–0.801 µm. Twelve sedimentary formations were selected in the Rhône-Alpes region (France) to analyse the discrimination potential of this camera for rock types and close-range mapping applications. After proper corrections and data processing, a supervised classification of the multispectral data was performed trying to distinguish four classes: limestones, marlstones, vegetation and shadows. After a maximum-likelihood classification, results confirmed that this camera can be efficiently exploited to map limestone-marlstone alternations in geological formations with this mineral composition.

Introduction

The knowledge of the mineralogical composition of sedimentary rocks is relevant to many disciplines and sectors. In the fields of Geology and Orogeny to discover this composition is the key for interpreting plate tectonic settings. Many regions have been destroyed and the only record lies in the sediments of the area. Thus, the relationship between the mineralogical composition of sediments and the tectonic plates provides a powerful tool for recognizing ancient tectonic settings [1]. However, ascertaining composition of geological formations in ancient sedimentary basins is generally difficult due to chemical and physical modification of source materials during weathering, erosion, transport and deposition [2]. For other fields such as Environmental Economics, the study of outcrops threatened by human activity and natural hazards as erosion, salinization and landslides is an important contribution. The clay and calcium carbonate contents of the soil are used to describe soil types and reveal their vulnerability to erosion [3, 4].

The past decade has seen the rapid adoption of digital measurement techniques in Geology due to the great advantages that they provide in contrast to expensive traditional techniques. Global navigation satellite systems (GNSS), photogrammetry, laser detection and ranging (LIDAR) and remote sensing satellite imaging systems have all been used for digital mapping and interpretation at multiple scales [5]. Focusing on the field of remote sensing, the shortwave infrared (SWIR) spectral range enable highly effective geological mapping [6], because rocks and minerals have their own inherent spectral pattern in this range [7, 8]. Multispectral satellite data is acquired at 10–30 m spatial resolution. For this resolution, satellite acquired signal in a pixel frequently corresponds to a mixture of several types of ground covers. Close-range remote sensing solves this spatial resolution problem avoiding such mix-up of covers. Collecting high spatial resolution data in a more flexible way and without inadequate temporal resolution due to orbital coverage patterns are some of the advantages of this technique. But it provides many other benefits as several authors [9–11] highlight: the ability to inspection restricted areas and not only the top of the outcrops, allowing real-time registration data for any configuration and orientation of the rock formation. Thus, by analysing close-range remote sensing data acquired from a versatile field-based platform it is possible to obtain more rigorous analysis or even improve the classification of multi-temporal satellite imagery.

Photogrammetric outcrop models [12] provide the framework for geological mapping and interpretation, which become indispensable to perform stratigraphic and structural analysis [13]. Some studies have proven the ability to discriminate between different sedimentary rocks and classify images from some outcropping terrains through the integration of multiple spatial and spectral close-range data. Hyspectral imagery and terrestrial LIDAR data fusion is a good example because they have proven to be a perfect combination to analyse different carbonate-rich outcrops [14–16]. Other works [17] demonstrate the feasibility of lithological interpretations and clay content predictions in sedimentary rocks by analysing the intensity from different wavelength terrestrial laser scanners. For all these works, sensors that cover the SWIR range (1.300–2.600 μm) have been used.

In this article the use of a 6-band multispectral camera covering the VIS and VNIR spectral range (0.530–0.801 μm) is proposed to demonstrate its ability to discriminate sedimentary rocks. A set of 12 geological formations with different percentages of clay and carbonate minerals were studied showing the potential of low-cost sensing for noncontact measurements in this field. In this way, geomorphology, geological mapping, exploration, geochemical hazards and other geological applications could be remotely assessed by using passive sensor technologies at ground level. The paper is organized as follows: Section 2 describes study area where the radiometric campaign took place; Section 3 explains the instruments used for data acquisition, and the data processing in which the protocol followed is also described; Section 4 describes and analyses the results achieved after the data processing, that is, the spectral signatures of different rock types, and the classified multispectral images. Finally, Section 5 includes the conclusions arising from the use of this sensor in this field and the future work.

Study Area

The radiometric campaign was carried out in June 2014 in the Drôme department of France, in the southeastern part of the Rhône-Alps region (Fig 1). This area is lithologically characterized by sedimentary deposits of the Upper Jurassic-Lower Cretaceous interval. In these periods, carbonate sedimentation was deposited at different water depths: a few meters only of depth in shallow-marine areas [18], and up to several hundred meters of water depth in pelagic marine areas. During these periods there were different deposition processes which gave rise to the current outcrops mainly consisting of carbonate minerals with trace amounts of silica (limestones)
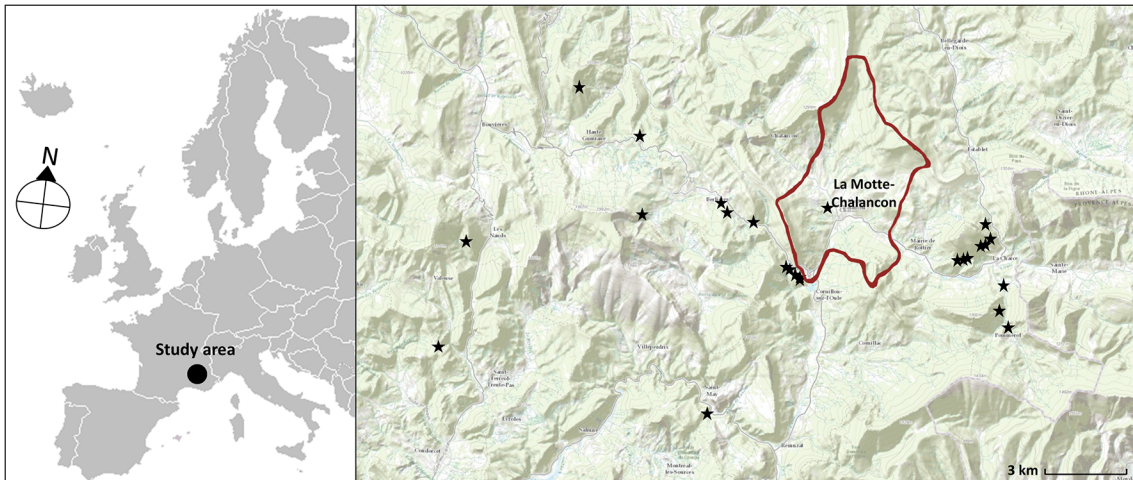
Fig 1. Location of the study area and the studied outcrops (the Drôme department, France).

and clay minerals (marlstones) with different degrees of uniformity across the layers of strata. On one hand, there were heterogeneous formations with limestone-marlstone alternations formed during the Kimmerdigien, Valanginian or Hauterivian ages (see Fig 2). On the other, there were more homogeneous massive outcrops from the Tithonian and Turonian ages. And finally, marlstone outcrops formed during the Oxfordian, Aptian and Albian ages [19]. The geology, geo-chemistry and mineralization of the study area are well described in the literature [20, 21].

It was possible to identify 12 different geologic formations, which together make up the stratigraphic column of the area (Fig 2). These outcrops are composed of limestone-marlstone alternations, with occasional sandstone beds, with different thicknesses and percentages. In all, the total stratigraphy is made up of three rock types: limestone, marlstone and sandstone, with variations of mineral content and different degrees of weathering. In this regard, the investigation presents some difficulties and challenges due to the mentioned variety of the rock masses.

Since only two of the twelve rock formations, Formation 2 and 4 (Fig 2), were composed of sandstone (100% and 10% respectively), the analysis was mainly focused on the discretization between the other two rock types: limestone and marlstone. In this case eleven of the twelve existing formations were composed of these two rock types.
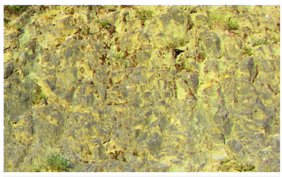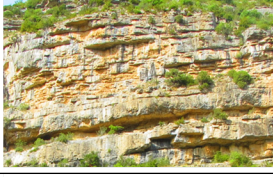
It was decided to perform a first analysis focusing on the discrimination of the pure formations due to the considerable variety in their composition and the spectral range and resolution limitations of the multispectral camera employed. Formation 1, 3 and 9 were analysed as pure limestones, Formation 2 as pure sandstone and Formation 12 as pure marlstone. Two mixture formations, Formation 4 and 6 were also analysed after a supervised classification. At first sight, and for a non-specialist user in this field, Formation 4 and Formation 12 seem to be the same; so one extra goal was to assess different spectral behaviours of them within the recording spectral rage.

Material and Methods

Equipment

For the geological data acquisition the Tetracam Mini MCA-6 multispectral camera (Fig 3) and several complementary devices for supporting the data collection were used. The 6-bands multispectral camera is mounted on a special platform and fixed to an adapter swivel to allow

Fig 2. Stratigraphic column of the 12-different Mesozoic geologic formations from newest to oldest.

getting stable shots during the data acquisition. This sensor consists of six bands covering the visible and very-near infrared range (0.530–0.801 μm) of the spectrum and collects the reflected solar radiation from each rock formation at 10-bits radiometric resolution. Each band is formed by a filter and a CMOS sensor (Complementary Metal-Oxide Semiconductor) providing each band its individual behaviour regarding the captured wavelength and the transmittance. The technical specifications of this sensor are shown in Table 1.

In order to obtain images with physical values (reflectance) from raw digital images two essential parameters must be known, the radiometric calibration parameters of each of the six bands (offset and gain, c_0 and c_1), and the solar irradiance (E) of the capture moment. Since the multispectral camera was radiometrically calibrated in a previous field campaign, c_0 and c_1 per band were known [22]. This calibration was a radiometric vicarious calibration based on the radiance method and closely related to the empirical line correction approach [23, 24]. On
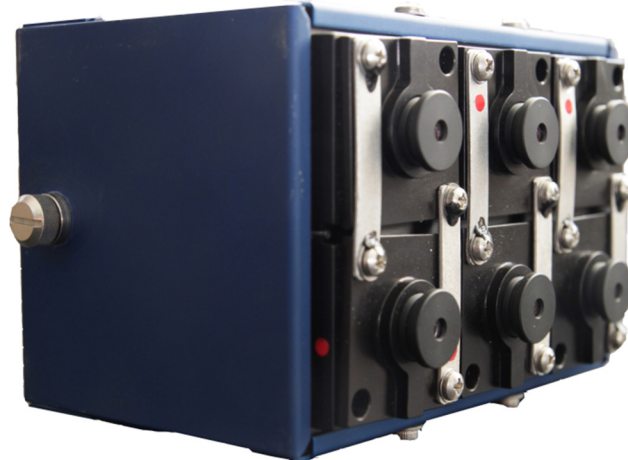
Fig 3. Tetracam Mini MCA-6 multispectral camera.

doi:10.1371/journal.pone.0132471.g003

the other hand, the solar irradiance for each capture moment was obtained by using a standard calibrated reflection target (Spectralon, Labsphere) as will be explained below. The calibrated Spectralon used in this study (Fig 4) consisted of four different panels of 99%, 50%, 25% and 12% reflectance. The spectral behaviour of each Spectralon panel was certified in laboratory.

Finally and because this camera is originally designed to be load on board unmanned aerial systems (UASs), auxiliary equipment becomes necessary for fixing the camera and all its devices to use it at ground level. For this purpose, a special platform to gather all the equipment was designed (see Fig 5). This platform along with a tripod and a swivel provided stability and allowed to rotate the camera in all three degrees of freedom to accommodate and level its position to the orientation of the outcrops.

Data acquisition protocol

During the field work a total of 40 images were acquired to cover the 12 different geologic formations in different scenarios of light and time of the day in order to have sufficient representative samples under different conditions. Fig 1 shows the exact location of all the outcrops that were sampled around the principal village, La Motte-Chalancon.

At each outcrop considered, the Spectralon was placed on the wall of the rock mass with the same orientation as the exposed surface (Fig 5), after which the ideal place to position the multispectral equipment was determined. Parameters as distance, orientation relative to the face of the rock and sun orientation were taking into account for that purpose. The distance is a significant parameter because both spatial resolution and the parallax between images depend on it.

Table 1. Characteristics of the Mini MCA-6 multispectral camera.

Features	Bandwidth
Number of bands: 6	Band 1 (0.530 µm): 40 nm
Distance between lenses: 34.5 mm	Band 2 (0.670 µm): 40 nm
Geometric resolution: 1280 x 1024	Band 3 (0.700 µm): 80 nm
Radiometric resolution: 10 bits	Band 4 (0.740 µm): 40 nm
Pixel size: 5.2 µm	Band 5 (0.780 µm): 80 nm
Focal length: 9.6 mm	Band 6 (0.801 µm): 80 nm

doi:10.1371/journal.pone.0132471.t001
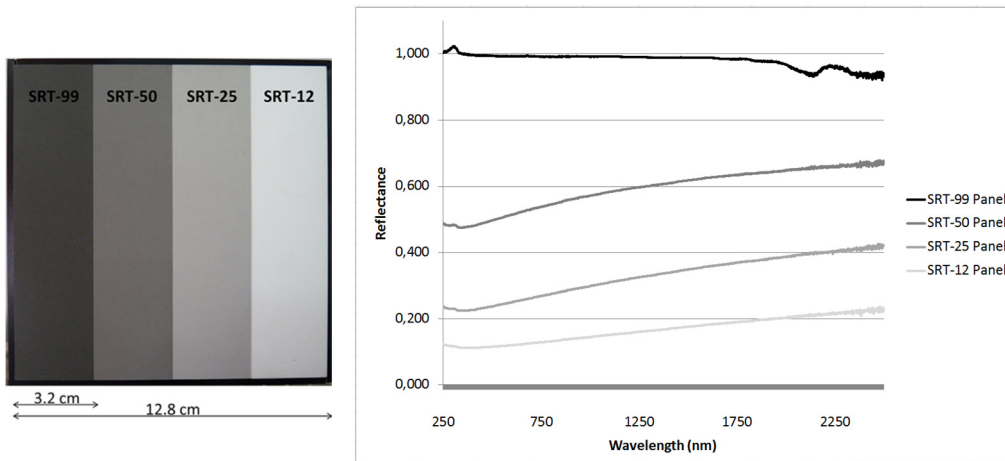
Fig 4. Hemispherical spectral reflectance factor of each Spectralon panel.

The Ground Sample Distance (*GSD*) is determined as the size of the pixel when the image is projected to the ground surface. The *GSD* value is affected by distance as characterized in Eq (1). Since the six camera lenses are not collinear, there is a parallax that affects images depending on this parameter. The greater the distance, the less parallax, until a limit is reached beyond which the parallax is becoming negligible. This limit is 64 m according to Eq (1). Note that the distance between objectives is 34.5 mm according to the manufacturer (see Table 1). As a consequence, the *GSD* has to be greater than 34.5 mm to avoid significant influence of parallax.

$$GSD = \frac{D \cdot S}{f} \qquad (1)$$
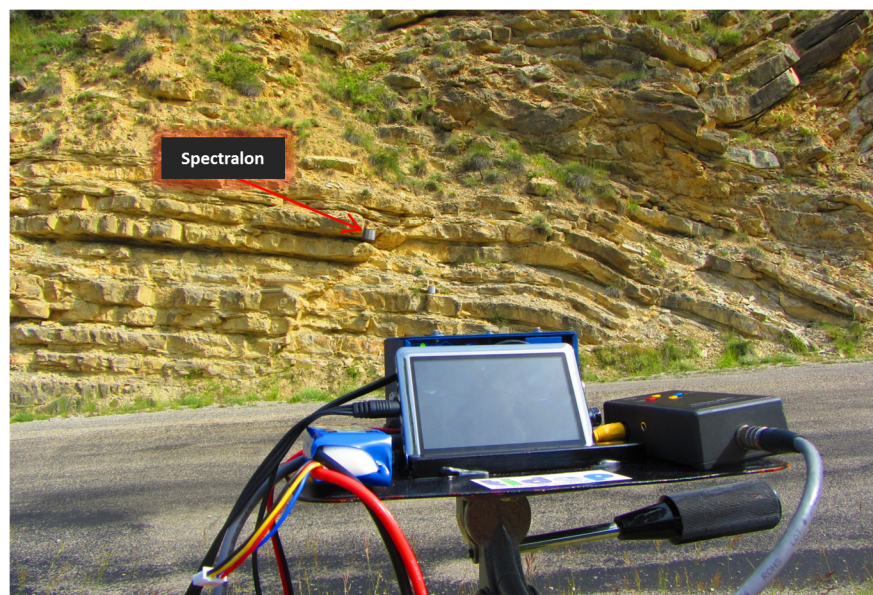
Fig 5. Positioning of the multispectral camera with respect to a rock formation including the Spectralon placed on the wall of the rock.

where D is the distance between the camera and the outcrop, S the pixel size of the sensor and f the focal length (see Table 1).

Thus, a balance between spatial resolution and the minimization of the parallax effect was sought. At that distance and with the right orientation thanks to the tripod swivel, visible and very near infrared images were taken such that all the exposed face was covered, whenever possible.

Data processing

Data processing involved three main phases: obtaining the solar irradiance at the moment of capture, transforming raw digital images into reflectance images (Fig 6) and performing super-vised classifications trying to draw conclusions from the composition differences among the geological formation analysed.

Solar irradiance at the moment of capture. Since data were collected at different locations and moments of the day, they were affected by the particular solar radiation at the moment of capture. It is necessary to eliminate the influence of this variability when extracting joint infor-mation from the data. In order to obtain images with pixel values independent of sunlight (reflectance images), digital levels (DL) of the raw spectral images have to be converted into surface reflectance values. This transformation requires the knowledge of the solar irradiance (E) at the precise moment of the image capture and the radiometric calibration parameters of each camera band ($c0_{band}$ and $c1_{band}$). The solar parameter was calculated from the reflected solar radiation of a Spectralon (Fig 4). For this purpose, the Spectralon was placed in every outcrop so that it appeared in each multispectral image (Fig 5). In the image processing phase, and making use of its 4 reflectance panels, an average of the raw pixel values panel was deter-mined. Thereby, 4 representative values of each reflectance panel per band ($DL_{(STR-99),band}$, $DL_{(STR-50),band}$, $DL_{(STR-25),band}$ and $DL_{(STR-12),band}$) were estimated. These values, together with the radiometric calibration parameters of each camera band, allowed the radiance values calcu-lation (Eq (2)). The calibration parameters were known beforehand since a vicarious radiomet-ric calibration of the camera [22] was previously performed. A set of 4 radiance values per band ($L_{i,band}$), one for each Spectralon panel, were estimated.

$$L_{i,band} = c0_{band} + \frac{c1_{band} \cdot DL_{i,band}}{T_{band}} \qquad (2)$$

With these parameters and according to Eq (3), an average of the solar irradiance ($\overline{E_{band}}$ [W. m2.sr-1.nm-1]) was estimated for each capture moment and band as an average of the four DL
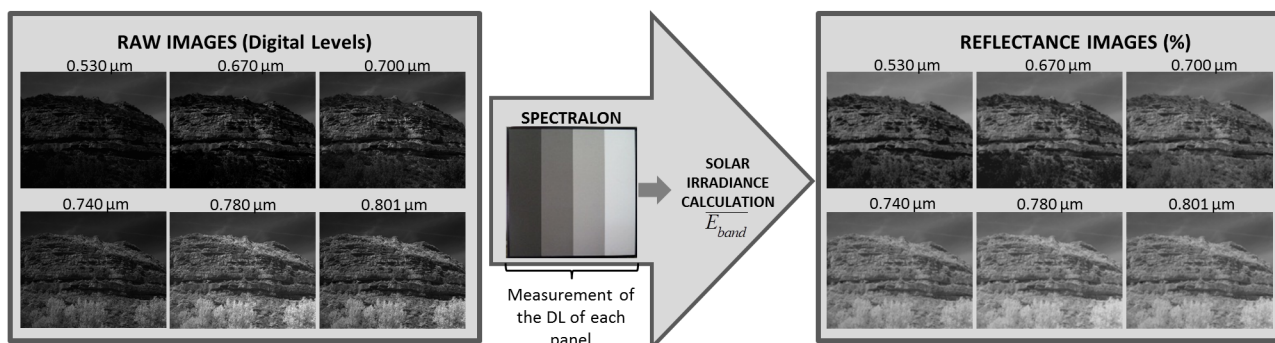
Fig 6. Workflow for obtaining images in reflectance values.

doi:10.1371/journal.pone.0132471.g006

values.

$$\overline{E_{band}} = \frac{1}{4} \cdot \sum_{i=1}^{4} \frac{L_{i,band}}{T_{band}} \cdot \pi \qquad (3)$$

where $c0_{band}$ and $c1_{band}$ are the radiometric calibration coefficients, of each camera band, T_{band} is the exposure time per band at each moment of the image capture and DL_i are the digital levels of each reflectance panel of the Spectralon.

Reflectance images. After this processing step, the first results of the research, spectral signatures of the outcrops, were obtained. Getting reflectance images involves transforming, digital levels of the raw images into reflectance values. In this way, assuming the outcrop as a rocky Lambertian surface (uniform reflectivity), the following Eq (4) is applied to every pixel of each six multispectral images.

$$R_{band(\%)} = \frac{c0_{band} + c1_{band} \cdot DL}{\overline{E_{band}}} \cdot \pi \qquad (4)$$

where $R_{band(\%)}$ is the reflectance value of each pixel in percentage. $c0_{band}$, $c1_{band}$ and $\overline{E_{band}}$ are the calibration parameters of the camera and the solar irradiance, respectively.

Once the reflectance images were obtained, multispectral images were created and stored as 6-dimensional matrixes (1024 pixels x 1280 pixels x 6 images) where reflectance values per band can be extracted just by clicking a pixel (Figs 7 and 8). If these reflectance pixel values are plotted on the y-axis and the respective wavelengths of the camera on the x-axis, spectral signatures of each geological formation are obtained. Taking into account the mean values and standard deviations of the outcrops, conclusions about the discrimination potential of the camera in this field were derived.

Classified images. The third step classifies the multispectral images into 4 classes: limestone, marlstone, vegetation and shadows; resulting in an easy-to-interpret classified image that will help to assess the use of this sensor in the characterization and recognition of rocks. For this purpose, a supervised classification based on the maximum likelihood (ML) algorithm [25] was performed after masking image pixels belonging to sky and/or road.

The ML classifier quantitatively evaluates both the variance and covariance of the category spectral response patterns when classifying an unknown pixel (x). Four different sets were prepared to train the process assuming that the distribution of the pixels forming the category training data is Gaussian. This assumption of normality is generally reasonable for common spectral response distributions. Under this assumption, the distribution of a category response pattern (k) can indeed be completely described by the mean vector and the covariance matrix.
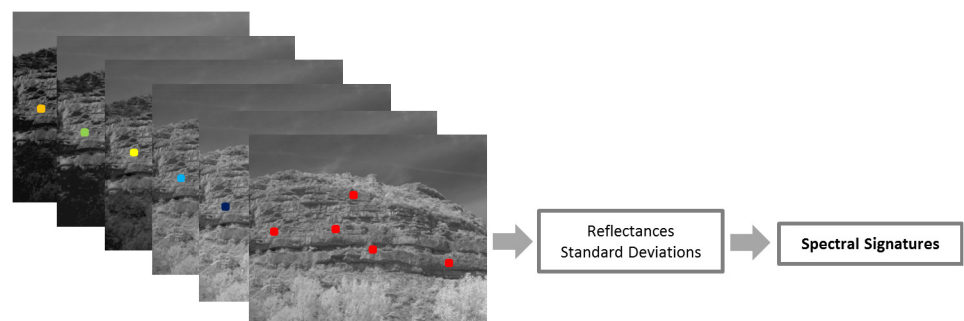
Fig 7. Reflectance per band of a specific rock formation.

doi:10.1371/journal.pone.0132471.g007
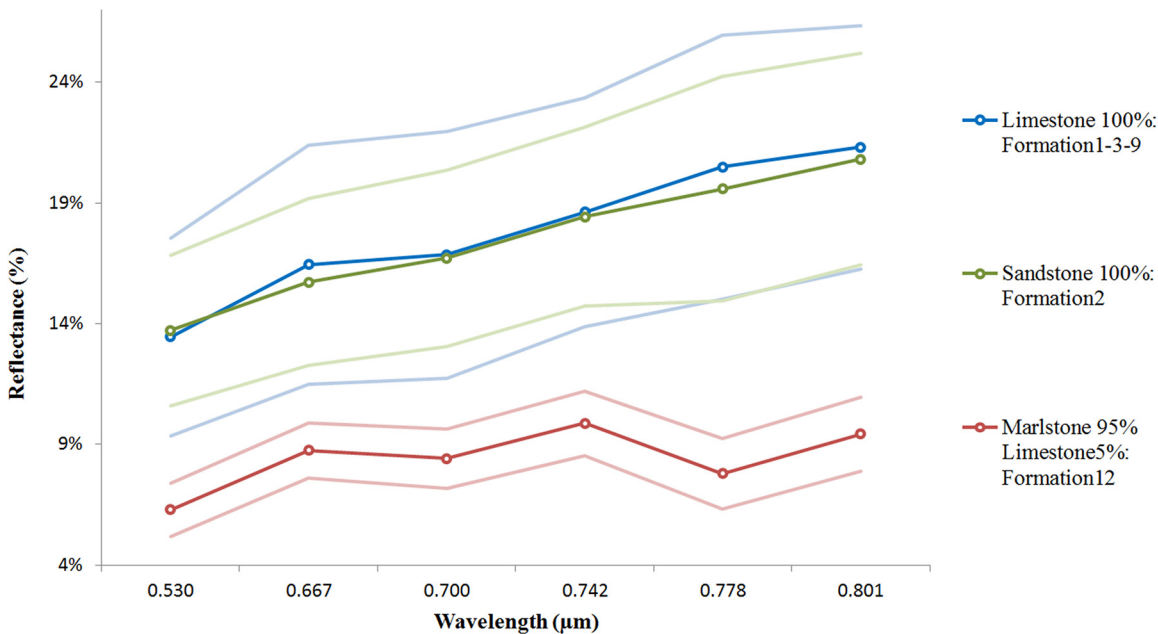
Fig 8. Spectral signatures of the three rock types and the standard deviation of their measurements.

With these parameters, the statistical probability of a given pixel value being a member of a particular land cover class ($P(x / k)$) can be computed. The resulting bell-shaped surfaces are called probability functions (Eq (5)), and there is one such function for each spectral category [26].

$$P(x/k) = -\ln\left|\sum k\right| - (x - \mu_k)^T \sum k^{-1}(x - \mu_k) \tag{5}$$

where $|\Sigma k|$ is the covariance matrix and μ_k the mean vector of the training data belonging to each class.

In this way, a class is assigned to a pixel when the probability of belonging to this class in Eq (5) is maximal.

Experimental Results

Spectral signatures

This research covers the study of 12 geological formations composed of three types of sedimentary rocks, sandstone, limestone and marlstone. Fig 8 depicts the spectral signatures of the geological formations with higher percentages of each of these rocks: Formation 1, Formation 2, Formation 3, Formation 9 and Formation 12 (compare Fig 2). Formation 1, 3 and 9 were analysed as pure limestones, Formation 2 as pure sandstone and Formation 12 as pure marlstone. For each rock formation manually representative pixels were selected, sampling areas clear of vegetation and shadows. For each selected pixel, reflectance values of the 5x5 nearest neighbours (involving 25 pixels) were stored. Finally, the average reflectance and standard deviation of the stored values were calculated with the support of software developed using Matlab.

For the considered samples the lowest standard deviation value (with an average of 1.3%) appears for the Formation 12 (95% marlstone). This behaviour is consistent with the hypothesis that experts support, errors in spectral measurements increase when the grain size increases [27]. A large grain has a greater internal path where photons may be absorbed [28]. Indeed

marlstones have the smallest grain size of the three types of rocks (< 0.06 mm) due to the clay minerals composition [29]. On the other hand, the highest deviation value occurred for limestones (with an average of 4.5%) very close to sandstones (with an average of 3.6%). In this case, there is much variability in the grain size due to the different composition of its fragments; but also because the spectral signature of limestones was calculated as an average of three different formations. Finally, another source of variability in the reflectance of a rock is the degree of mechanical weathering [30], so depending on the massivity and the degree of homogeneity of the formation more or less errors were obtained in the measurements.

By analysing the reflectivity of the examined formations it can be confirmed that the spectral signatures are coherent with the reflectance behaviour of their minerals. Eleven of the twelve geological formations are composed of different proportions of limestone and marlstone. Only Formation 2 and 4 are composed of sandstone (100% and 10% respectively). For that reason, the analysis was mainly focused on the discretization between these two rock types (limestones and marlstones). Limestones are composed mainly of calcium carbonate. Moreover, marlstones are composed of clay. Due to the reflective properties of these materials (higher reflectance in the case of calcium carbonate [31]) depending on the percentage of these components, more or less reflectance was obtained. Fig 8 shows that the spectral signature of sandstones and limestones in the 0.530–0.801 μm spectral range is quite similar. In addition, Fig 8 indicates that it is possible to discriminate between limestones and marlstones because, in spite of the high variability of limestone measurements, both spectral signatures do not overlap.

As pointed out in Section 2, obtaining any difference between Formation 4 and Formation 12 was a challenge because these formations, at first sight, look the same. As shown in Fig 9, and despite of the reflectivity differences between these two formations, we may not be able to obtain good results from a classification based only on these two formations due to their spectral patterns overlap (taking into account the standard deviations). Nevertheless, their spectral signatures are consistent with their composition; Formation 4 has more reflectivity because it
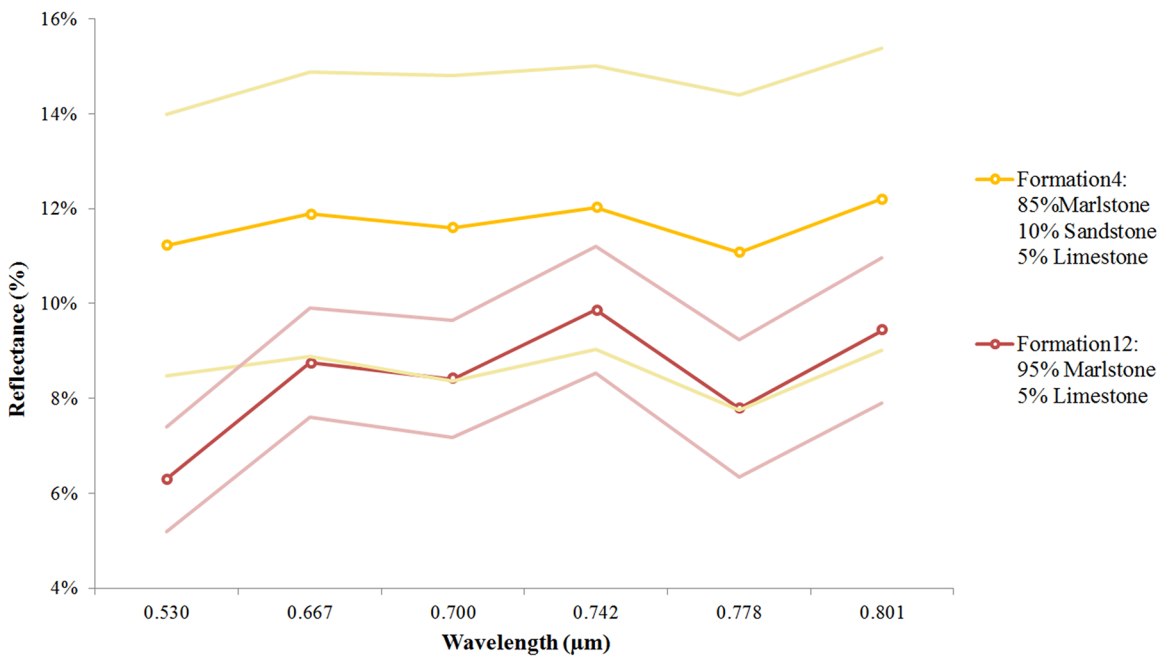
Fig 9. Spectral signatures of Formation 4 and 12 and the standard deviation of the measurements.

contains sandstone. Regarding the deviation degree of measurements (an average of 3.1% in Formation 4), the explanation lies in the fact that the greater variability in the composition, the greater deviation in the measurements.

Classification results

In the third step of data processing a supervised classification was performed. Four different training sets were chosen to classify final reflectance images into 4 classes: limestone, marlstone, vegetation and shadow. Sandstone was excluded from the classification process as only two formations, Formation 2 and 4, were composed of this material and because the results in Fig 8 indicate that the spectral response of sandstone in the spectral range covered by the sensor is almost identical to that of the pure limestone formation. Formation 1, 3 and 9 were selected to represent pure limestone and Formation 12 representing pure marlstone. Fig 10 illustrates the resulting classified images for the case of four geological formations, pure limestone and marlstone (Formation 1 and Formation 12) and two mixed formations (Formation 4 and Formation 6). In the classified images white pixels represent pixels masked previously to be out of this process.

The classified images were obtained after calculating the probability of belonging to each of the 4 classes. This probability was graphically represented for each class as an 8-bit grey scale image where the maximum probability was represented in white (value of 255) and the minimum in black (value of 0). These probability images are shown in order in Fig 10B: probability of belonging to the limestone, marlstone, vegetation or shadow class. It is observed that vegetation areas are perfectly discriminated except in the case of the Formation 12 where some vegetation areas were classified as limestone. This fact happens due to the pre-set configuration of the camera filters. The wavelengths of each filter were chosen for previous vegetation studies. Vegetation absorbs red and reflects green and infrared radiation. So by analysing red and infrared wavelengths we can provide information about the vegetation´s health [32].

Regarding the mixed formations, in the case of Formation 4 there was a higher percentage of blue pixels (limestone) even though their real percentage is 5%. A possible explanation was the presence of sandstone (10%) and because the slope of the outcrop influenced the way the light was reflected.

To evaluate the separability between classes the transformed divergence based on means and variance-covariance matrix [33] was used as a quantitative estimator for the 4 training samples. Table 2 shows the separability between the 4 classes (without considering the background or null class).

As Table 2 shows, results from class separability confirm that the main goal of this study has been achieved, a high separability between limestone and marlstone (99.99%). It must be pointed out that for this results a proper radiometric calibration of the multispectral camera and different lenses corrections [22] were applied to work in reflectance values (characteristic values of each material). The worst case was for marlstone and shadows (90.42% of separability) but remained within an acceptable range. This fact would be explained due to the low reflectivity of this sedimentary rock. In this way, there were some areas where the classification was less efficient than it should be. To conclude, it is also worth noting that whenever vegetation was compared to another class, separability results were quite good. This was expected because the configuration of the wavelengths makes the camera ideal for vegetation studies.

Conclusions

In this paper a visible-very near infrared multispectral camera was tested and analysed in a field campaign in the Drôme department of France. As a result, its ability and limitations to
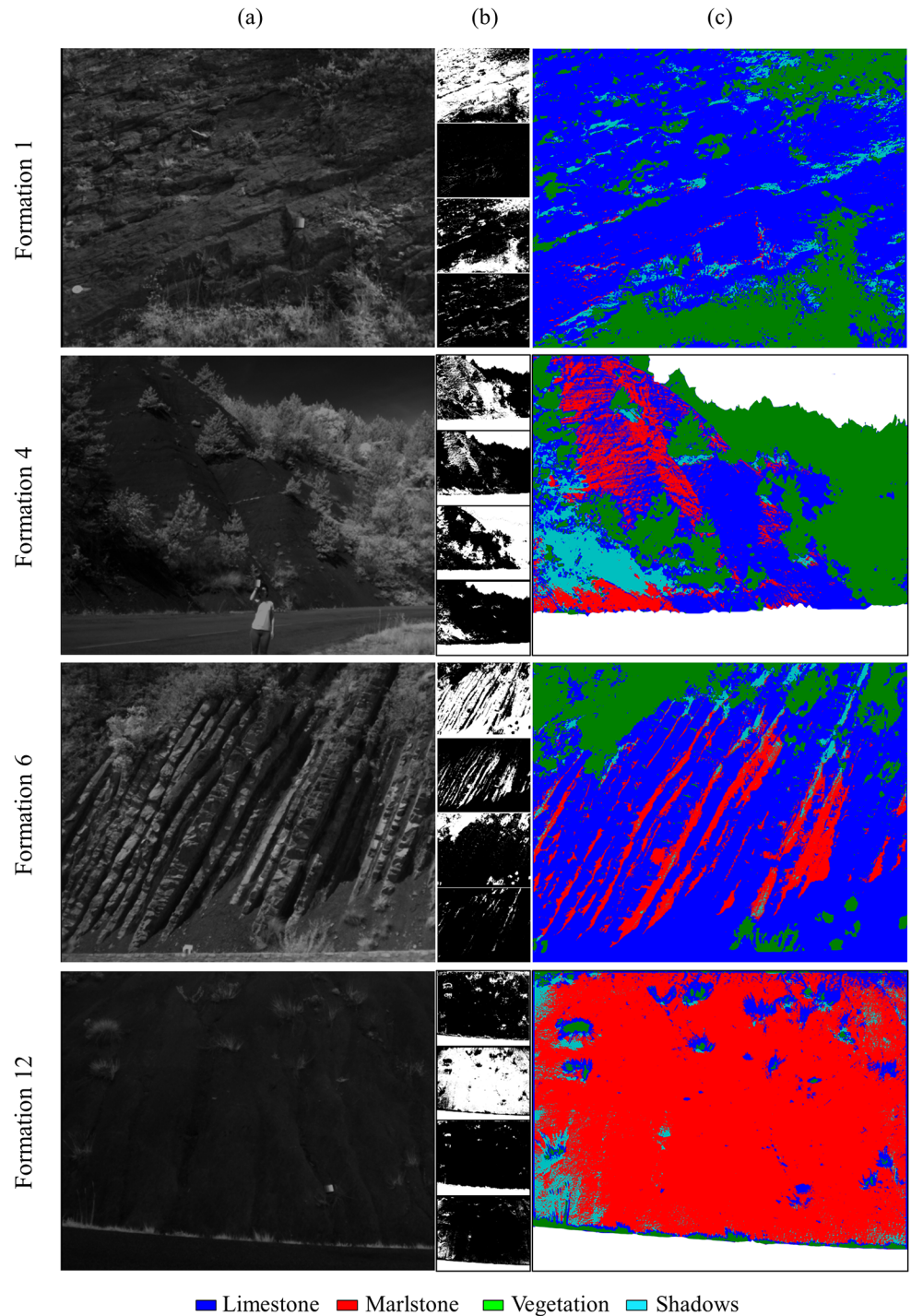
Fig 10. (a) Band-5 reflectance images. (b) Images of probability. (c) Final classified images.

doi:10.1371/journal.pone.0132471.g010

discretize sedimentary rock formations were evaluated regarding the spectral range of the camera (0.530–0.801 μm) and the homogeneity of the rock surfaces.

Regarding the spectral signatures of the most pure geological formations (Fig 8) it is concluded that although it is not possible to completely discriminate between all of them, the

Table 2. Transformed divergence (0–2).

	Limestone	Marlstone	Vegetation
Marlstone	1.999834	-	-
Vegetation	1.999739	2.000000	-
Shadow	1.917816	1.808445	1.988555

spectral signatures are consistent with their composition. The highest reflectivity response was obtained for sandstones and limestones, which usually consist of quartz and calcite grains respectively. Finally Formation 12, composed mostly of marlstones, obtained the lowest reflectivity. Due to the percentage of sandstone in the Formation 4 (10%) it had higher reflectance than Formation 12 although both mostly had the same grain size and similar degree of weathering.

As these geological formations were mainly composed by 2 of the 3 types of sedimentary rocks analysed (limestone and marlstone), a maximum likelihood supervised classification was performed by distinguishing 4 classes: limestone, marlstone, vegetation and shadows. After comparing the classified images (Fig 10) with their corresponding geological formation composition (Fig 2), it is possible to conclude that this multispectral camera is able to discriminate between these 2 types of sedimentary rocks. It has been demonstrated that limestones and marlstones have different spectral patterns in the 0.530–0.801-μm spectral range. By contrast, it is not possible to find notable differences between the response patterns of limestones and sandstone. The spectral range of this camera does not allow the discrimination between them. It would be possible by using a capture sensor that works in the SWIR range of the spectrum (1.4–3μm).

Derived from this analysis, some conclusions are listed on the difficulties we found in the radiometric analysis of rocks in general and the limitations arising from the use of this camera in particular:

- The orientation of the outcrop complicates radiometric analysis because different orientations and roughness reflect light in different directions [34]. Even if the camera is properly stationed, it will pick different reflectances from the same rock due to the different orientation of their faces.

- The homogeneity of the geological formation is a relevant property. In this study the most homogeneous lithological mass belongs to the Formation 12 [35], the "Terres Noires" formation, which had the lowest standard deviation in its measurements.

- Greater homogeneity in sunlight results in a better radiometric analysis because the rock will be evenly illuminated without the presence of shadows or glare in different parts. Therefore, cloudy days are the most suitable days for data collection.

- The spectral range of the camera is not the most suitable for characterizing different types of geological formations, although results in the discrimination of rock types are encouraging.

Future improvements in methods and equipment will help to achieve better results. With respect to methods, Bidirectional Reflectance Distribution Function (BRDF) studies could be incorporated to study how light is reflected at each geological formation and moment. In this way, reflectance results will improve as it is no longer necessary to assume that the surfaces scatter in a Lambertian way and depend on the slope of the outcrop. Regarding the equipment, the combined use of different remote sensors such as terrestrial laser scanners, will

complement spectral information and will provide 3D models giving scale, slope and surface roughness. This information may help improve the final classification process.

Acknowledgments

Author Contributions

References

1. Bhatia MR, Crook KA. Trace element characteristics of graywackes and tectonic setting discrimination of sedimentary basins. Contributions to mineralogy and petrology. 1986; 92(2):181–93.

2. Johnsson MJ. The system controlling the composition of clastic sediments. Geological Society of America Special Papers. 1993; 284:1–20.

3. Yl Bissonnais. Aggregate stability and assessment of soil crustability and erodibility: I. Theory and methodology. European Journal of Soil Science. 1996; 47(4):425–37.

4. Lagacherie P, Baret F, Feret J-B, Madeira Netto J, Robbez-Masson JM. Estimation of soil clay and calcium carbonate using laboratory, field and airborne hyperspectral measurements. Remote Sensing of Environment. 2008; 112(3):825–35.

5. McCaffrey K, Jones R, Holdsworth R, Wilson R, Clegg P, Imber J, et al. Unlocking the spatial dimension: digital technologies and the future of geoscience fieldwork. Journal of the Geological Society. 2005; 162(6):927–38.

6. Kurz TH, Dewit J, Buckley SJ, Thurmond JB, Hunt DW, Swennen R. Hyperspectral image analysis of different carbonate lithologies (limestone, karst and hydrothermal dolomites): the Pozalagua Quarry case study (Cantabria, North-west Spain). Sedimentology. 2012; 59(2):623–45.

7. Kobayashi C, Orihashi Y, Hiarata D, Naranjo J, Kobayashi M, Anma R. Compositional variations revealed by ASTER image analysis of the Viedma Volcano, southern Andes Volcanic Zone. Andean Geology. 2010; 37(2):433–41.

8. Clark RN. Spectroscopy of rocks and minerals, and principles of spectroscopy. Manual of remote sensing. 1999; 3:3–58.

9. Feng Q, Röshoff K. In-situ mapping and documentation of rock faces using a full-coverage 3d laser scanning technique. International Journal of Rock Mechanics and Mining Sciences. 2004; 41:139–44.

10. Haneberg WC, Norrish NI, Findley DP, editors. Digital outcrop characterization for 3-D structural mapping and rock slope design along interstate 90 near Snoqualmie Pass, Washington. Proceedings, 57th annual highway geology symposium, Breckenridge, Colorado; 2006.

11. Tonon F, Kottenstette J, editors. Laser and photogrammetric methods for rock face characterization. Report on a workshop held in Golden, Colorado; 2006.

12. Xu X, Aiken CL, Bhattacharya JP, Corbeanu RM, Nielsen KC, McMechan GA, et al. Creating virtual 3-D outcrop. The Leading Edge. 2000; 19(2):197–202.

13. Bellian JA, Kerans C, Jennette DC. Digital outcrop models: applications of terrestrial scanning lidar technology in stratigraphic modeling. Journal of Sedimentary Research. 2005; 75(2):166–76.

14. Kurz TH, Buckley SJ, Howell JA, Schneider D. Integration of panoramic hyperspectral imaging with terrestrial lidar data. The Photogrammetric Record. 2011; 26(134):212–28.

15. Kurz TH, Buckley SJ, Howell JA. Close-range hyperspectral imaging for geological field studies: workflow and methods. International Journal of Remote Sensing. 2013; 34(5):1798–822.

16. Buckley SJ, Kurz TH, Howell JA, Schneider D. Terrestrial lidar and hyperspectral data fusion products for geological outcrop analysis. Computers & Geosciences. 2013; 54:249–58.

17. Franceschi M, Teza G, Preto N, Pesci A, Galgaro A, Girardi S. Discrimination between marls and limestones using intensity data from terrestrial laser scanner. ISPRS Journal of Photogrammetry and Remote Sensing. 2009; 64(6):522–8.

18. Boulila S, Galbrun B, Hinnov LA, Collin PY, Ogg JG, Fortwengler D, et al. Milankovitch and sub-Milankovitch forcing of the Oxfordian (Late Jurassic) Terres Noires Formation (SE France) and global implications. Basin Research. 2010; 22(5):717–32.

19. Reichelt K. Late Aptian-Albian of the Vocontian Basin (SE-France) and Albian of NE-Texas: Biostratigraphic and paleoceanographic implications by planktic foraminifera faunas: Universität Tübingen; 2005.

20. Rameil N. Early diagenetic dolomitization and dedolomitization of Late Jurassic and earliest Cretaceous platform carbonates: a case study from the Jura Mountains (NW Switzerland, E France). Sedimentary Geology. 2008; 212(1):70–85.

21. Antoine P, Giraud A, Meunier M, Van Asch T. Geological and geotechnical properties of the "Terres Noires" in southeastern France: weathering, erosion, solid transport and instability. Engineering Geology. 1995; 40(3):223–34.

22. Del Pozo S, Rodríguez-Gonzálvez P, Hernández-López D, Felipe-García B. Vicarious Radiometric Calibration of a Multispectral Camera on Board an Unmanned Aerial System. Remote Sensing. 2014; 6(3):1918–37.

23. Moran M, Bryant R, Thome K, Ni W, Nouvellon Y, Gonzalez-Dugo M, et al. A refined empirical line approach for reflectance factor retrieval from Landsat-5 TM and Landsat-7 ETM+. Remote Sensing of Environment. 2001; 78(1):71–82.

24. Smith GM, Milton EJ. The use of the empirical line method to calibrate remotely sensed data to reflectance. International Journal of Remote Sensing. 1999; 20(13):2653–62.

25. Richards JA, Richards J. Remote sensing digital image analysis: Springer; 1999.

26. Lillesand TM, Kiefer RW, Chipman JW. Remote sensing and image interpretation: John Wiley & Sons Ltd; 2004.

27. Lillesand TM, Kiefer RW, Chipman JW. Remote sensing and image interpretation: John Wiley & Sons Ltd; 2004.

28. Van der Meer FD, Van der Werff HM, van Ruitenbeek FJ, Hecker CA, Bakker WH, Noomen MF, et al. Multi-and hyperspectral geologic remote sensing: A review. International Journal of Applied Earth Observation and Geoinformation. 2012; 14(1):112–28.

29. Roser B, Korsch R. Determination of tectonic setting of sandstone-mudstone suites using content and ratio. The Journal of Geology. 1986:635–50.

30. Dematte JAM, Garcia GJ. Alteration of soil properties through a weathering sequence as evaluated by spectral reflectance. Soil Science Society of America Journal. 1999; 63(2):327–42.

31. Viscarra Rossel R, Cattle S, Ortega A, Fouad Y. In situ measurements of soil colour, mineral composition and clay content by vis–NIR spectroscopy. Geoderma. 2009; 150(3):253–66.

32. Turner W, Spector S, Gardiner N, Fladeland M, Sterling E, Steininger M. Remote sensing for biodiversity science and conservation. Trends in ecology & evolution. 2003; 18(6):306–14.

33. Davis SM, Landgrebe DA, Phillips TL, Swain PH, Hoffer RM, Lindenlaub JC, et al. Remote sensing: the quantitative approach. New York, McGraw-Hill International Book Co, 1978 405 p. 1978; 1.

34. Olkkonen M, Bra Brainard DH. Joint effects of illumination geometry and object shape in the perception of surface reflectance. i-Perception. 2011; 2(9):1014. doi: 10.1068/i0480 PMID: 23145259

35. Phan TSH. Propriétés physiques et caractéristiques géotechniques des Terres Noires du Sud-Est de la France 1993.

CAPÍTULO IV

FUSIÓN SENSORIAL APLICADA A LOS CAMPOS DE LA INGENIERÍA CIVIL Y EL PATRIMONIO CULTURAL

4. FUSIÓN SENSORIAL APLICADA A LOS CAMPOS DE LA INGENIERÍA CIVIL Y EL PATRIMONIO CULTURAL

4.1. Detección de patologías en fachadas a partir de teledetección activa y pasiva

Este subcapítulo contiene el artículo *Multispectral radiometric analysis of façades to detect pathologies from active and passive remote sensing,* (Análisis radiométrico multispectral de fachadas para la detección de patologías a partir de teledetección activa y pasiva) publicado en Enero de 2016 en la revista internacional *Remote Sensing*.

4.1.1. Resumen

El propósito de este trabajo consistió en conseguir la fusión de dos sensores geomáticos con distintos principios de funcionamiento, uno pasivo y uno activo, para detectar posibles patologías presentes en los materiales de construcción de fachadas. Es decir, conseguir determinar, en primer lugar, qué principio de funcionamiento y rango espectral es el más adecuado para la detección de patologías como la humedad, la colonización biológica (musgos, hongos, etc.) o posibles alteraciones químicas de los materiales y, en segundo lugar, evaluar el grado de mejora derivado del uso de sensores calibrados radiométricamente. Para tal fin, la cámara multiespectral Mini MCA-6 (ver Capítulo II) y el láser escáner terrestre FARO® Focus3D fueron analizados.

Los sensores pasivos capturan la radiación natural reflejada por la superficie de las cubiertas mientras que los sensores activos emiten su propia fuente de radiación con el fin de escanear los objetos (Kaasalainen et al., 2005). Si bien es cierto que el uso del láser escáner terrestre está más extendido para el caso de estudios geométricos y de medición de

distancias, en este caso la intensidad procedente de su señal de retorno es utilizada para analizar radiométricamente distintas coberturas terrestres. La principal ventaja de la teledetección activa es que es menos influenciable por las condiciones atmosféricas que la pasiva y que puede ser empleada tanto de día como de noche.

Para combinar los datos crudos procedentes de ambos sensores y analizaros en términos de variables físicas (reflectancias en este caso), han de aplicarse primeramente una serie de transformaciones y correcciones. En el caso de las imágenes multiespectrales, estas deben ser corregidas de dos errores radiométricos sistemáticos que se transmiten a las imágenes finales, el error de ruido de fondo y el efecto de viñeteo (ver Capítulo II). Por su parte, los distintos escaneos láser deben ser alineados y posteriormente filtrados para eliminar información redundante.

Después de este pre-procesamiento, y gracias el uso de un Spectralon® durante la adquisición de datos (ver Capítulo III), los valores crudos procedentes de cada sensor fueron transformados a valores de reflectancia. En el caso de la cámara multiespectral, esta fue previamente calibrada en otro trabajo de campo (ver Capítulo II), por lo que sólo fue necesario conocer la irradiancia solar en el momento de cada adquisición. En el caso del láser, se llevó a cabo una calibración radiométrica vicaria por el método de reflectancias (Palmer, 1993) previa a la campaña de campo. En ella se analizó la relación existente entre la intensidad de la señal de retorno procedente del escaneado del Spectralon® y sus valores de reflectancia conocidos y calibrados a priori.

Finalmente, y de cara a analizar los datos de ambos sensores de forma conjunta, tanto los datos 3D como las imágenes multiespectrales fueron transformados a ortoimágenes verdaderas gracias a la métrica proporcionada por el láser escáner y tras el cálculo previo de orientación externa de cada imagen multiespectral. Estas ortoimágenes fueron clasificadas de forma no supervisada y de forma supervisada tanto en valores de niveles digitales como en reflectancias, concluyéndose que:

- El sensor para el que se obtuvieron mejores resultados fue el láser escáner terrestre debido a que, por un lado, no se ve influenciado por los cambios en las condiciones de iluminación y, por otro, a

que la patología que principalmente presentaba la fachada (humedad), se caracteriza mejor en la longitud de onda ofrecida por este sensor. Por su parte, los resultados de la cámara multiespectral estaban condicionados tanto por el registro de sus seis bandas para la generación de las ortoimágenes como por la influencia de las variaciones de iluminación. Cabría esperar mejores resultados del sensor pasivo si la adquisición de datos se hubiera llevado a cabo un día nublado con luz difusa.

- Hay que mencionar el valor añadido que aporta el láser escáner a los datos radiométricos. Proporciona escala y como resultado no solamente es posible cuantificar las patologías detectadas sino también detectar otros posibles problemas estructurales tales como grietas, descamaciones, etc.

Para ambos sensores se lograron mejoras significativas derivadas de su uso calibrado. Se obtuvo una mejora mínima del 34% en el coeficiente Kappa (Cohen, 1960) después de calibrar radiométricamente ambos sensores.

Article

Multispectral Radiometric Analysis of Façades to Detect Pathologies from Active and Passive Remote Sensing

Susana Del Pozo [1],*, Jesús Herrero-Pascual [1], Beatriz Felipe-García [2], David Hernández-López [2], Pablo Rodríguez-Gonzálvez [1] and Diego González-Aguilera [1]

[1] Department of Cartographic and Land Engineering, University of Salamanca, Hornos Caleros, 05003 Ávila, Spain; sabap@usal.es (J.H.-P.); pablorgsf@usal.es (P.R.-G.); daguilera@usal.es (D.G.-A.)
[2] Institute for Regional Development (IDR), Albacete, University of Castilla La Mancha, 02071 Albacete, Spain; bfelipe@jccm.es (B.F.-G.); david.hernandez@uclm.es (D.H.-L.)
* Correspondence: s.p.aguilera@usal.es; Tel.: +34-920-353-500; Fax: +34-920-353-501

Abstract: This paper presents a radiometric study to recognize pathologies in façades of historical buildings by using two different remote sensing technologies covering part of the visible and very near infrared spectrum (530–905 nm). Building materials deteriorate over the years due to different extrinsic and intrinsic agents, so assessing these affections in a non-invasive way is crucial to help preserve them since in many cases they are valuable and some have been declared monuments of cultural interest. For the investigation, passive and active remote acquisition systems were applied operating at different wavelengths. A 6-band Mini-MCA multispectral camera (530–801 nm) and a FARO Focus3D terrestrial laser scanner (905 nm) were used with the dual purpose of detecting different materials and damages on building façades as well as determining which acquisition system and spectral range is more suitable for this kind of studies. The laser scan points were used as base to create orthoimages, the input of the two different classification processes performed. The set of all orthoimages from both sensors was classified under supervision. Furthermore, orthoimages from each individual sensor were automatically classified to compare results from each sensor with the reference supervised classification. Higher overall accuracy with the FARO Focus3D, 74.39%, was obtained with respect to the Mini MCA6, 66.04%. Finally, after applying the radiometric calibration, a minimum improvement of 24% in the image classification results was obtained in terms of overall accuracy.

Keywords: cultural heritage; multispectral camera; laser scanning; radiometric calibration; remote sensing; close range photogrammetry; multispectral classification

1. Introduction

Historical buildings and monuments are valuable constructions for the area where they are placed. The degradation of their construction materials is caused mainly by environmental factors such as pollution and meteorological conditions. Specifically, the presence of water plays an important role in stone deterioration processes [1]. It accelerates the weathering processes contributing to dissolution and frost/thaw cycles among others [2] allowing the formation of black crust on the rock surface resulting in mechanical and chemical degradations of stones. For that reason the use of non-contact and non-destructive technologies to study stone damages is important for the preservation of buildings and for the choice of the best technique for restoration [3,4].

Terrestrial laser scanners and multispectral digital cameras are two different technologies that are suitable for these studies. They are non-destructive and non-invasive sensors that allow researchers to

acquire massive geometric and radiometric information across the building with high accuracy and in a short acquisition time. The geometrical information provided by laser scanner technology has been successfully applied in a large number of fields such as archaeology [5], civil engineering [6], geology [7] and geomorphological analysis [8]. On the other hand, radiometric information, provided by the laser intensity data and the multispectral digital cameras, is used less frequently. Even so, its high potential for classification tasks and recognition of different materials has been demonstrated [9]. Nowadays, in the literature, one can find works related to this issue ranging from methodologies of radiometric calibration [10] to corrections of intensity values [9,11] including applications of the intensity data [12]. Spectral classification methods are based on the properties of the reflected radiation from each surface and the fact that each specific material has wavelength dependent reflection characteristics. There are many classification methods, which vary in complexity. These methods include hard and soft classifiers, parametric and non-parametric methods and supervised and unsupervised techniques [13]. There are several works related to the application of these techniques to the identification of damage on building surfaces [14–18].

The main objective of this paper is the classification and mapping of pathologies and materials of a historical building façade from reflectance values at different wavelengths by combining intensity calibrated data from a FARO Focus3D laser scanner and calibrated images from a 6-band Mini-MCA multispectral camera. Additional goals were evaluating the degree of automation in the pathology detection process of façades. To achieve these objectives, the paper is divided into the following sections: Section 2 gives the details and specifications of the equipment employed and thoroughly describes the methods employed in the workflow methodology. Section 3 shows the classification maps and accuracy results for both unsupervised and supervised classifications, closing with Section 4 which summarizes the main conclusions and findings drawn from the study.

2. Material and Methods

The methodology developed to reach the objectives of the paper consists of three main stages: the data acquisition, the pre-processing and the processing of data as is outlined in Figure 1. For the data acquisition, two sensors with different operating principles were implemented: a passive multispectral camera and an active terrestrial laser scanner. The pre-processing step involved data filtering and several corrections applied to the spectral information to finally obtain data in reflectance values. During the last step and taking advantage of the metrics from the scan points, reflectance orthoimages were generated for both the multispectral images and the laser intensity. These orthoimages were the input for two different classifications processes: a clustering classification with data from each sensor and a supervised classification with the set of all data from both sensors.
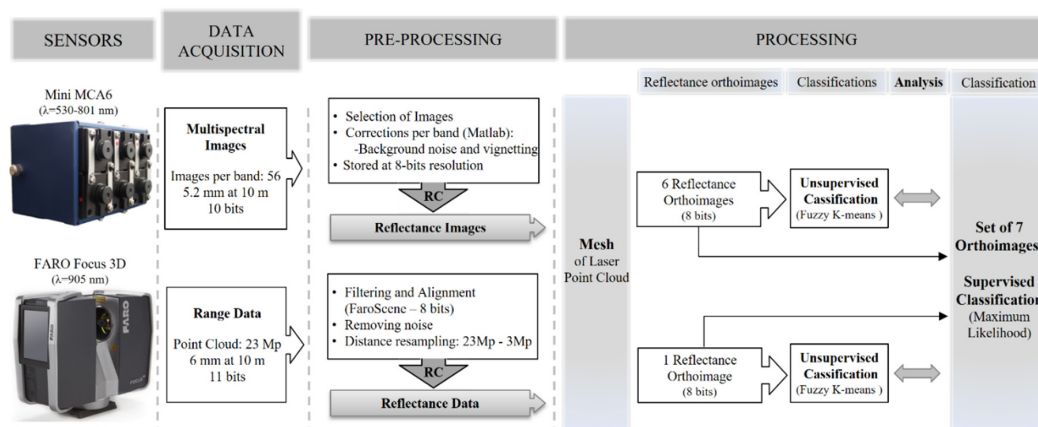
Figure 1. The workflow of the methodology presented. Acronyms: RC = Radiometric calibration and Mp = Millions of points.

2.1. Equipment

For the documentation of the façade, the following equipment was used: two radiometrically calibrated sensors with different characteristics and data acquisition principles, a passive multispectral camera and an active terrestrial laser scanner. Figure 1 shows the main characteristics of them and the different stages of the workflow followed in this research.

For the multispectral data acquisition, a calibrated lightweight Multiple Camera Array (MCA-Tetracam) was employed. This low-cost sensor allows versatility in data acquisition; however it requires the radiometric and geometric corrections to ensure the quality of the results [19]. It includes a total of 6 individual sensors with filters for the visible and near infrared spectrum data acquisition. More specifically, the individual bands of 530, 672, 700, 742, 778 and 801 nm were used. The longest wavelength was chosen taking into account that the multispectral sensor is not externally cooled. In spite of its 1280 × 1024 pixels of image resolution, the camera has a radiometric resolution of 10 bits. The focal length of 9.6 mm and the pixel size of 5.2 μm yield a façade sample distance (FSD) of 5.4 mm for a distance of 10 m, which should be taken into account for the pathology detection performance in small elements. The main limitation of this camera is the field of view (38° × 31°), so several captures were needed to keep the FSD.

The FARO Focus3D is a phase shift continuous wave terrestrial laser scanner (TLS) operating at a wavelength of 905 nm. It is not common to use this kind of sensor to perform radiometric studies but it guarantees a comprehensive data acquisition whose results are not influenced by changes in light. This device measures distances in a range of 0.60–120 m with a point measurement rate of 976,000 points per second. It has an accuracy of 0.015° in normal lighting and reflectivity conditions and a beam divergence of 0.19 mrad, equivalent to 19 mm per 100 m range. The field of view covers 320° vertically and 360° horizontally with a 0.009° of angular resolution and the returning intensity is recorded at 11 bits. This laser scanner includes, in addition, a double compensator in the horizontal and vertical axis that can be used as constraint for the scan alignment.

Additionally, a high resolution spectroradiometer (ASD FieldSpec3) (Figure 2) was used as a remote detector of radiant intensity from the visible to the shortwave infrared ranges (350 to 2500 nm with a maximum spectral resolution of 3 nm and ±1 nm wavelength accuracy) to validate the spectral results of the study [20]. Equipped with optical fiber cables, it measured reflectances from the different materials and covers of the façade with a 25° field of view. Measures were made by positioning the spectroradiometer gun (Figure 2a) as orthogonal as possible and at a distance of approximately 10 cm from the sample, trying to cover a relatively homogeneous area of the material.
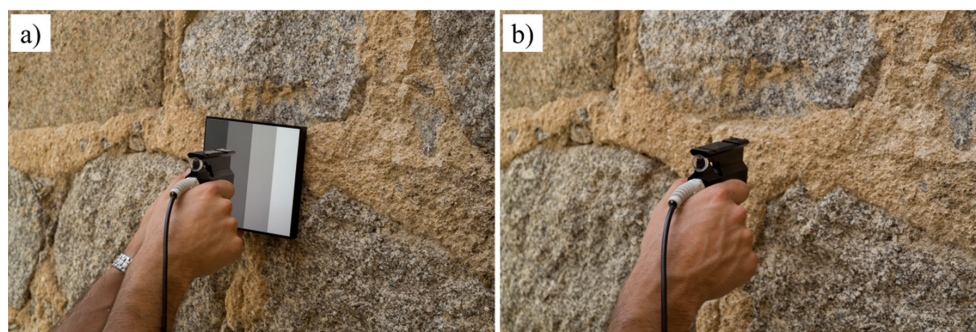
Figure 2. ASD FieldSpec3 spectroradiometer collecting spectral radiation reflected from (**a**) the Spectralon target and (**b**) mortar between contiguous stones of the examined façade.

2.2. Data Acquisition

Since each material has a unique reflectance behavior depending of the wavelength, the presence of pathologies on façades, such as moisture, moss or efflorescence, is likely to be successfully detected by analyzing the reflected visible and very near infrared radiation from the façades in reflectance

values instead of digital levels (output digital format of the device). That is why these two sensors were radiometrically pre-calibrated and used to obtain orthoimages with surface reflectance values instead of digital levels. Since reflectance, for the specific case of a passive sensor, is a function of the solar incident radiance, a standard calibrated reflection target (Spectralon, Labsphere) was required and placed on the façade (Figure 2a), thus it appeared in every multispectral image to be able to calculate the solar irradiance (*E*) of each capture moment.

Illumination is a crucial parameter for data acquisition with passive sensor, particularly when several shot positions are required to cover the object of study. For that reason and to ensure the greatest resolution, taking fewer photos as far as possible was prioritized in this study. A total of 56 captures were collected with a FSD of 5.4 mm for the worst case so that the standard calibrated reflection target appeared in all of them.

On the other hand, the laser scanner data acquisition was designed so that the effect of the laser beam incidence angle [21,22] was minimized. Intensity data at 11-bit resolution was collected at an average distance of 10 m through three scans with scan area restrictions. Thus, 7 m of façade were covered for each of the scans assuming a maximum incidence angle error of 5.6% regarding the maximum oblique angle of incidence (19.29°). In addition, scanning positions were selected according to the different technical specifications of the scanner for an spatial resolution of 6 mm at the working distance. The laser network was adapted and filtered due to the presence of obstacles that hinder a single station data acquisition.

2.3. Pre-Processing

Before the reflectance orthoimage generation some corrections to raw data were applied to avoid error propagation in the radiometric calibration process. In this section, these radiometric corrections and the final radiometric calibration were described as well as the orthoimages generation process. Finally, the orthoimages were classified to obtain maps of different pathologies and building materials.

2.3.1. Multispectral Images Corrections

Low-cost sensors, such as the Mini MCA6, are more likely to be affected by different noise sources so that the actual value of radiation collected by them is altered (Equation (1)) [23]. Specifically, the Mini MCA6 was affected by two different sources errors: a background noise and a vignetting effect [20]. Both errors were studied under precise laboratory controlled conditions for each wavelength band.

The background noise is a systematic error caused by the sensor electronics of the camera. It was analyzed in a completely dark room in the absence of light determining the noise per band depending on the exposure time. For this study, the maximum background error was for the 801-nm band and involved a 1.07% increment of the actual digital level value. Regarding the vignetting effect [24], the radial attenuation of the brightness was studied taking images of a white pattern with uniform lighting conditions. Digital levels of each multispectral image were corrected for these two effects through a script developed in Matlab to improve the data quality before the radiometric calibration.

$$DL_{raw} = DL_{radiance} + (DL_{bn} + DL_v) \tag{1}$$

where DL_{raw} are the digital levels of the raw images, $DL_{radiance}$ are the digital levels from the radiance component, DL_{bn} are the digital levels from background noise and DL_v are the digital levels from the vignetting component.

2.3.2. Filtering and Alignment of the Point Clouds

The raw laser scanner data were filtered and segmented in order to remove those points that were not part of the object of study (adjacent building, artificial elements, trees, *etc.*). The individual point cloud alignment was done by a solid rigid transformation by the use of external artificial targets (spheres). The spheres were stationed in tripods at the plumb-line plane surveyed by the global navigation satellite system (GNSS). The laser local coordinate system could be transformed to a global

coordinate system (UTM30N in ETRS89), allowing the geo-referencing of the subsequent classification for a global analysis and interpretation. This proposed workflow allowed a final relative precision of the coordinates of the artificial targets of 0.01 m and an absolute error of 0.03 m after post-processing. As a result, a unique point cloud in a local coordinate system with 11 mm precision (due to the error propagation of inherent error sources of laser scanner [25] and the error associated to the definition of the coordinate system) was generated.

2.3.3. Radiometric Calibrations

To perform the radiometric calibration of both sensors, auxiliary equipment such as lambertian surfaces with known spectral behavior (Spectralon) and/or a spectroradiometer are needed to solve the calibration. Thus, after the calibration process images values, in the case of the camera, and points' intensities, in the case of the laser scanner, correspond to the radiation emitted by the surface expressed in radiance or reflectance. The Mini MCA6 multispectral camera was calibrated in a previous field campaign [20] through *in situ* spectroradiometer measurements of artificial surfaces, with known and unknown reflectance behavior (Spectralon and polyvinyl chloride vinyl sheets respectively). Regarding the radiometric calibration of the TLS, it was carried out in laboratory by using a Spectralon and in absence of light.

The multispectral camera was calibrated by the radiance-based vicarious method [26–28], being the transformation equation from raw images into images with reflectances values Equation (2):

$$\rho_{MCA} = \frac{c0_\lambda + c1_\lambda \cdot DL/Fv_\lambda}{E_\lambda} \cdot \pi \tag{2}$$

where $c0_\lambda$ and $c1_\lambda$, offset and gain, are the calibration coefficients of each camera band, Fv_λ the shutter opening time factor and E_λ the solar irradiance at the ground level. Table 1 summarizes the multispectral camera calibration coefficients and the R^2 determination coefficient achieved per band.

Table 1. Calibration coefficients of the Mini MCA6 per band.

Bands	$c0_\lambda$	$c1_\lambda$	R^2
530 nm	0.000264	0.057718	0.9816
672 nm	−0.000795	0.050005	0.9823
700 nm	−0.000861	0.041353	0.9820
742 nm	−0.001205	0.074335	0.9843
778 nm	−0.001510	0.047292	0.9846
801 nm	−0.000834	0.047656	0.9827

In order to obtain reflectance values directly from laser data, a reflectance-based radiometric calibration [28] consisting of analyzing the distance-behavior of the intensity data (Figure 3) was performed (Equation (3)).

$$\rho_{FARO} = e^{a \cdot d} \cdot b \cdot d^2 \cdot e^{c1_F \cdot DL_F} \tag{3}$$

where a and b were the empirical coefficients related to the signal attenuation and internal TLS conversion from the received power to the final digital levels, d the distance between the laser scanner and the object, $c1_F$ the gain of the TLS and DL_F the raw intensity data in digital levels (11 bits). Please note that the empirical coefficients were obtained by a laboratory study, since the TLS internal electronics and intermediate signal processing is not disclosed.

In this case, a laboratory experiment from 5 to 36 m at one-meter intervals provided enough information to study the FARO Focus3D internal behavior (Figure 3). It was conducted in low-light conditions at a controlled temperature of 20 °C to model and simulate the system behavior. By positioning a Spectralon at each distance increment, intensity data were acquired at a quarter

of the maximum resolution of the laser scanner (6 mm). The calibrated surface (Figure 2a) consists of four panels of 12%, 25%, 50% and 99% reflectance and it was assembled on a stable tripod to ensure its verticality. The raw intensity data from each reflectance panel were obtained by averaging the intensity values of the points belonging to each panel. The mean intensity value was plotted per panel and distance resulting in the Figure 4.
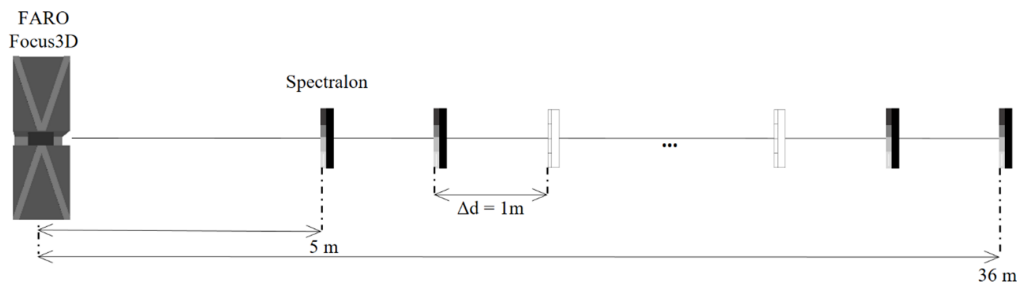
Figure 3. Sketch of the test performed to analyze the internal radiometric behavior of the FARO Focus3D.
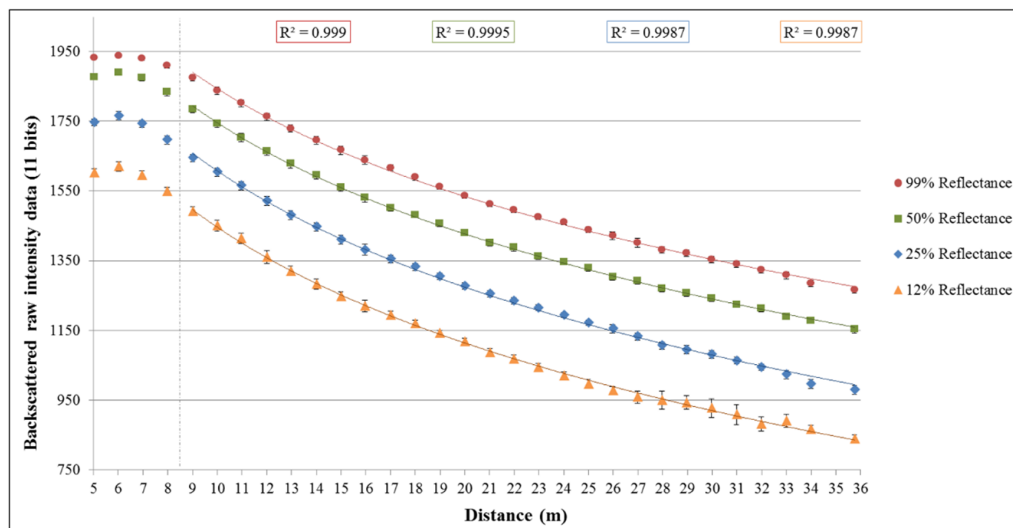
Figure 4. FARO Focus3D backscattered intensity behavior for the measurements of the four Spectralon panels at 1 m distance increments related to the signal attenuation (Equation (3)).

Figure 4 shows the signal attenuation of the FARO Focus 3D with distance as well as the logarithmic model that the measurements follow for distances up to 9 m. This particular behavior was noted in previous research works with similar sensors [29] and it is explained by the lidar equation [30]. By knowing the calibrated reflectance values of each Spectralon panel for 905 nm, the wavelength of the laser scanner, field measurements could be related with these reflectance values at each studied distance. Being 0.992, 0.560, 0.287 and 0.139 the normalized (0–1) reflectance values for the panel of 99%, 50%, 25% and 12% of reflectance respectively. Figure 5 shows how these values relate at a 10 m distance, and follow an exponential relationship which is shown in Equation (3). This distance was chosen as a threshold since for lower distances the calibration model changes due to the internal measurement system, involving alternative mathematical models.

As Figure 4 shows, the greater the distance the greater the intensity errors in the measurements. This behavior is related to the decrease of the received power due to the distance attenuation and signal scattering. Since the effective range of the employed TLS is higher than the studied distance, this error only appears significantly in the lower reflectance surface (12% panel).
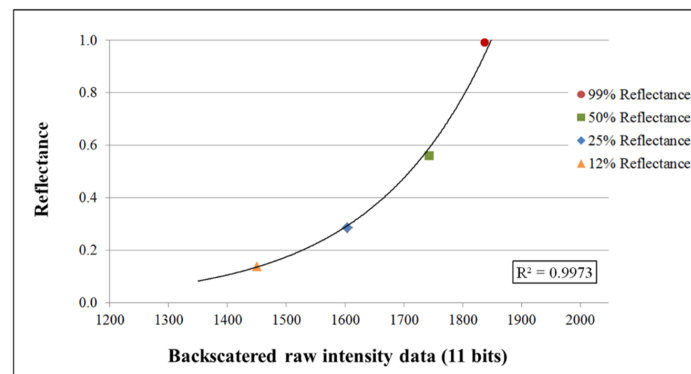
Figure 5. Relationship between TLS raw intensity data and reflectance for each spectralon panel at 10 m distance.

Based on the empirical study of the laser response, the attenuation of the signal with the distance (Figure 4) and the logarithmic behavior of the sensor [29], the relationship between digital levels and reflectances was finally approximated according to the Equation (4).

$$\rho_{FARO} = e^{0.214 \cdot d} \cdot 3.907 \cdot 10^{-7} d^2 \cdot e^{0.005415 \cdot DL_F} \tag{4}$$

This empirical equation can be applied only to objects at a distance over than 8 m since as can be shown in Figure 4, the FARO Focus3D has a completely different behavior for shorter distances.

2.4. Processing

In this subsection reflectance products are joined to achieve the orthoimages at each wavelength and they are finally classified to obtain maps of different building materials and pathologies.

2.4.1. Orthoimages Generation

Once the final point cloud was filtered, aligned and calibrated, a triangulation was applied to create the digital façade model (DFM). This step was required in order to generate continue 2D products (in the form of true orthoimages) and carry out the pathology detection by the classification process. For the DSM generation the incremental triangulation Delaunay algorithm was applied [31]. The output was refined to avoid artifact, meshing gaps, and other errors [32].

Orthoimages are highly demanded products that offer many benefits: metric accuracy and radiometric information useful to analyze different information quantitatively and qualitatively.

For the orthoimage generation, it was necessary to know the external orientation of the images with respect to the coordinate system of the laser point cloud model. For that purpose an average of 20 corresponding points between the point cloud and images were manually established. The image projection was characterized by a rigid transformation (rotation and translation) together with the internal camera parameters.

Orthoimages were generated based on the anchor point method [33]. This method consists of applying an affine transformation to each one of the planes formed by the optimized triangular mesh, which was obtained from the point cloud determined by the laser. Through the collinearity condition [34], the pixel coordinates of the vertices of the mesh were calculated, and the mathematical model of the affine transformation directly relates the pixel coordinates of the registered image and of the orthoimage.

2.4.2. Orthoimages Classifications

In order to categorize the orthoimages in different informational classes a previous automatic unsupervised classification and a posterior supervised classification were performed. The unsupervised classification was based on the Fuzzy K-means clustering algorithm where each

observation can concurrently belong to multiple clusters [35]. For a set of *n* multidimensional pixels, the automatic management in *l* clusters iteratively minimizes the Equation (5) [36]:

$$J_m = \sum_{i=1}^{n} \sum_{l=1}^{\lambda} u^m{}_{i,l} \| x_i - c_l \|^2 \; ; \; 1 \leqslant m < \infty \tag{5}$$

where *m* represents any real number greater than 1, x_i the *i*-th of *d*-dimensional measured data, u_{il} the degree of membership of x_i *in* the cluster *l*, c_l the *d*-dimensional center of the cluster and $\| ** \| =$ Euclidean norm expressing the similarity between any measured data and the center.

Fuzzy partitioning is carried out through an iterative optimization of the objective function shown above, with the update of membership and the cluster centers by Equation (6).

$$u_{il} = \frac{1}{\sum\limits_{k=1}^{c} \left[\frac{\| x_i - c_l \|}{\| x_i - c_k \|} \right]^{\frac{2}{m-1}}} \; ; \; c_l = \frac{\sum\limits_{i=1}^{n} u_{il}^m \cdot x_i}{\sum\limits_{i=1}^{n} u_{il}^m} \tag{6}$$

This iteration will stop when $\max_{il} \left\{ \left| u_{il}{}^{(k+1)} - u_{il}{}^{(k)} \right| \right\} < \varepsilon$, where ε is the stop criterion between 0 and 1 and *k* represents the iteration steps.

After this classification, a first approach of the spectral classes and different construction materials was obtained. With a subsequently supervised classification and applying the expert knowledge of some classes, the final results improved. Furthermore, this supervised classification will serve as reference to discuss which sensor is the ideal one for detecting materials and pathologies in façades.

In this case, a maximum likelihood (ML) classification algorithm [37] was applied. The ML classifier quantitatively evaluates both the variance and covariance of the category spectral response patterns when classifying an unknown pixel. The resulting bell-shaped surfaces are called probability functions, and if the prior distributions of this function are not known, then it is possible to assume that all classes are equally probable. As a consequence, we can drop the probability in the computation of the discriminant function *F*(g) (Equation (7)), and there is one such function for each spectral category [38].

$$F(g) = -\ln \left| \Sigma_p \right| - (g - \mu_p)^T \Sigma_p{}^{-1} (g - \mu_p) \tag{7}$$

where *p* is the *p*-th cluster, Σ_p is the variance-covariance matrix and μ_p represents the class mean vector and *g* the observed pixel.

3. Experimental Results

The study area was the Shrine of San Segundo declared World Cultural Heritage in 1923 [39] (Figure 6). This Romanesque shrine is located in the west of the city of Ávila (Spain) and was built in the 12th century with unaltered grey granite plinths and walls with the alternation of granite blocks with different alteration degrees. The unaltered granite is mainly present in the blocks of low areas because of its high compressive strength and resistance to water absorption.

The field work was carried out on 27 July 2012 around the southern façade of the church (Figure 6), the most interesting façade from a historical point of view because it preserves the Romanesque main front. The five archivolts and capitals are decorated with plant and animal motifs. A total of 3 stations for the case of laser scanner were performed to cover the façade at a distance of 10 m (see Figure 6 right). The resolution of the data capture of the FARO Focus3D was a quarter of the full resolution provided by the manufacturer, 6 mm at 10 m. Moreover, the façade was photographed at the same distance with the Mini MCA6 multispectral camera with a FSD of 5.4 mm. A selection of 9 multispectral images of the 56 (7 per station) were used for the orthoimages generation. This selection was related with the most suitable images regarding the area of study and the optimal sharpness and quality of the set of

images. The total volume of information generated amounted to 10.7 GB, where the great part was due to the meshes and orthoimages generation projects. Figure 7 shows the set of the 7 final orthoimages with a 6 mm FSD.
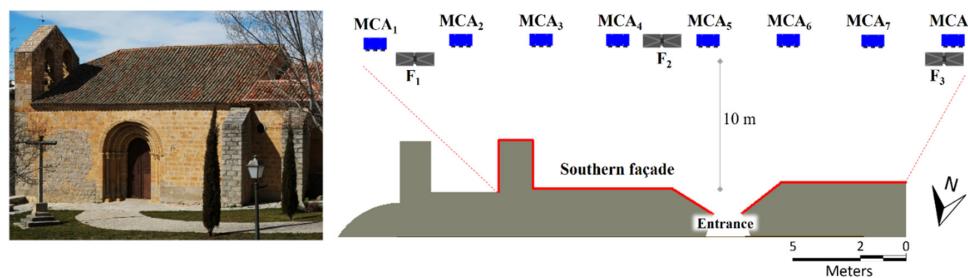
Figure 6. South façade of the Church of San Segundo in Ávila (Spain) (**left**) and a sketch of the acquisition setup with the different sensor's stations (MCA6-multispectral camera, FARO Focus3D) (**right**).
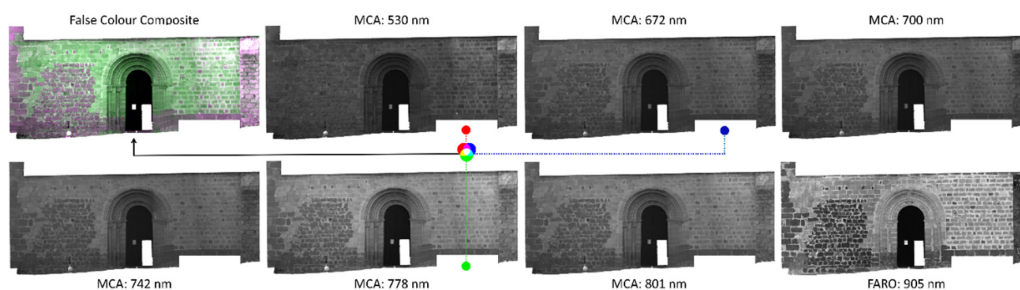
Figure 7. Set of 7 orthoimages of the façade in reflectance values from the two analyzed sensors (MCA6 multispectral camera and FARO Focus3D) and a false colorcolor composite orthoimage.

3.1. Reflectance Orthoimages

In order to compare the discrimination capability of both technologies to distinguish building materials and pathologies a first unsupervised classification of the orthoimages belonging to each sensor was performed (Figures 8 and 9). A final supervised classification with the complete set of 7 orthoimages was carried out. For each informational class manually representative areas distributed throughout the façade (between 5 and 10 polygons per class) were selected. This last classification serves as a reference with which to compare each individual unsupervised classification. The steps followed by the workflow are shown in Figure 1.
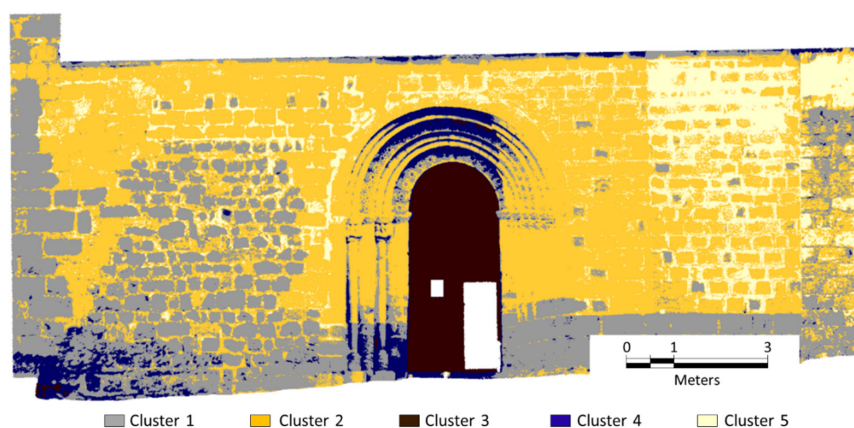
Figure 8. Mini MCA6 map for the 5-clusters unsupervised classification.

Figure 9. FARO Focus3D map for the 5-clusters unsupervised classification.

3.2. Orthoimages Classifications

Ten predefined clusters were used in each case for the unsupervised classification algorithm. In all of them, the resulting map showed the existence of affected areas. Post-analysis reduced the number of clusters. The number of clusters decreased from 10 (initial clusters) to 5 thematic classes with real meaning: (1) unaltered granite; (2) altered granite; (3) wood (door of the church); (4) areas with moisture evidences (caused by capillarity or filtration water) and (5) mortar between blocks.

It is noteworthy that results from Mini MCA6 are not fully satisfactory due to large variability in lighting conditions during the data acquisition. As mentioned at the beginning of Section 3, the fieldwork took place on 27 July 2012, with a 6-h total acquisition time. Although radiometric calibration reduces the effects of the lighting variability between different data acquisition time, passive sensors are really sensitive to shady areas. These areas could be seen in Figure 7, specifically in the orthoimages from the Mini MCA6, and also in the classification results of the entrance area in Figure 8 (blue color). However, this is not the case for the active sensor, FARO Focus3D, where the continuity of materials and pathologies is a remarkable aspect.

Comparing the results with a visual inspection, results correspond quite well to reality for both types of existing granites (unaltered and altered) and wood by three well differentiated clusters in all classification maps (Figures 8 and 9). Regarding pathologies detection, it was not possible to draw final conclusions with these first unsupervised classifications. However, this process served to perform a better defined supervised classification.

With the aim of having a reference with which to compare both unsupervised classification maps, a supervised classification of the full set of 7 orthoimages in reflectance values was performed (Figure 10) taking into account the two existing variants of granite, their pathologies derived primarily from moisture and the other informational classes.

The best overall accuracy for the Fuzzy K-means unsupervised classifications was 74.39%, achieved for the FARO Focus3D map in contrast with the 66.04% accuracy for the Mini MCA6 map. This indicates that the best correlation between the number of pixels correctly classified and the total number of pixels occurred for this near infrared active sensor.

Table 2 contrasts the results of the supervised classification (based on training areas) with the unsupervised classification for each sensor. The table shows the sum of pixels belonging to each class for each of the classifications performed. The count is expressed as a percentage of the total number of classified pixels (1,154,932 without taking the background class into account).

Figure 10. Multisensory map for the 5 informational classes supervised classification.

Table 2. Pixels computation belonging to each thematic class.

Class	Reference Map	Multispectral Map	Laser Map
Unaltered granite	30.04%	28.53%	27.33%
Altered granite	42.60%	48.06%	47.27%
Wood	5.35%	5.67%	5.82%
Moisture	1.88%	4.74%	1.31%
Mortar	20.13%	13.00%	18.27%

In a quantitative analysis for the estimation of the two types of granite and wood, results of both sensors are quite similar and really close to the reference map while intensity data from laser scanner are the closest to the reference map results for the estimation of moisture and mortar. Results show higher pixels classified as moisture in the case of multispectral map (2.86% higher with respect to the reference map) and few pixels classified as mortar (7.13% lower than the reference map) due mainly to the altered granite count (whose spectral response has the greatest similarity). Results from the laser sensor are quite similar, greater amount of altered granite by reducing the unaltered granite and mortar detected classes. Note that the best results for moisture detection are achieved with the FARO Focus3D, since humidity has a major interference with this wavelength [40]. Since the pathological classes (moisture and altered granite) are better recognized by the laser scanner and it is the most comprehensive sensor with results closer to the reference, it can be concluded that the active sensor has proven to be the best option to study and detect pathologies and different construction materials for studies with high variability in light conditions where passive sensors are greatly affected.

To evaluate the separability between classes the transformed divergence indicator [41], ranging from 0 to 2, was used as the most widely used quantitative estimator for this purpose [42]. Table 3 shows the separability between the final 5 classes.

Table 3. Transformed divergence for the supervised classification.

	Unaltered Granite	Altered Granite	Wood	Moisture
Altered granite	1.87	-	-	-
Wood	2.00	2.00	-	-
Moisture	1.99	1.99	2.00	-
Mortar	1.98	1.42	2.00	2.00

In general, a high separability was achieved for all 5 classes, highlighting the good separability between the spectral signatures of the two granite types. The worst results were for the mortar and the altered granite classes. This fact is explained by two reasons: on the one hand, the façade sample distance (FSD) of the orthoimages (11 mm in the worst case) was not enough to detect façade areas with smaller thickness of mortar; and on the other, altered granite class presented the closest spectral behavior regarding mortar. With respect to the moisture of the façade, it appeared in lower areas of the shrine (capillarity rising damp) and in the buttress, acting as a filter system for the water from the roof (filtration moisture). These areas are built with unaltered granite blocks since lower areas need to support the loads of the whole building (also in buttress). The radiometric misunderstanding between moisture and unaltered granite did not occur in the case of altered granite since the latter is part of the center of the façade, a low humidity area.

3.3. Accuracy Assessment

In order to assess the accuracy of the unsupervised classifications, the supervised classification approach based on maximum likelihood algorithm served as reference. Five classes and the seven bands available were considered in the classification process. Accuracy results for the case of the Mini MCA6 multispectral camera and the FARO Focus3D laser scanner were 66.04% and 74.39% respectively as mentioned above, and according to the Cohen's Kappa coefficient [43] the level of agreement was 0.50 and 0.621 respectively (excluding the null class).

Furthermore, as mentioned in Section 2.1, an ASD FieldSpec3 spectroradiometer was used to measure several samples of granite for a parallel study. Those measures, in this study, have been used as reference and as a complement to the above analysis to compare the spectral signatures of these construction materials with the discrete reflectance results obtained from the Mini MCA6 and the FARO Focus3D (Figure 11). The spectral signatures and deviations of the two types of granite present in the façade are plotted for the wavelength range covered by both sensors (530–905 nm).

In Figure 11, the graph continuous lines show at any wavelength the mean value of the reflectances of unaltered and altered granite samples distributed along the façade and measured with the spectroradiometer (a total of 6 and 7 samples of granite, respectively). On the other hand, the colored areas represent the standard deviation of that spectroradiometer measurements. Regarding the discrete values of reflectance achieved with the sensors (discrete points) they result from the mean reflectance value of the "unaltered granite" and "altered granite" classes for each sensor's wavelength of the supervised classification map. The "mortar" class was not finally evaluated due to its variability in thickness along the façade and due to the fact that the FSD achieved was in many areas greater than its thickness.

It should be mentioned that a great fit of the reflectance values from both sensors (discrete points) was achieved for both granite real spectral behaviors (spectroradiometer measurements) with admissible standard deviations associated (lower than those associated with spectroradiometer measurements). For both evaluated materials, the mean error was 0.007 (in the range 0–1), being the maximum 0.049 (in the range 0–1), which is better than the expected error for this vicarious calibration technique (around 5%).

The confusion matrices for the assessment of both sensors are shown in Tables 4 and 5 where the main diagonal indicates the percentage of pixels that have been correctly classify and the off-diagonal values represent misclassification. The producer and user accuracies as well as the overall accuravy are given. Regarding the moisture class, a significant performance improvement of the classifier is observed for this class for the operating wavelength of the FARO Focus3D. In the case of the mortar class, the Mini MCA6 do not bring good results mainly due to the errors produced during the 6-band registration process. Finally, we mention that in the case of the unaltered and altered granites, little variations were observed between both sensors.
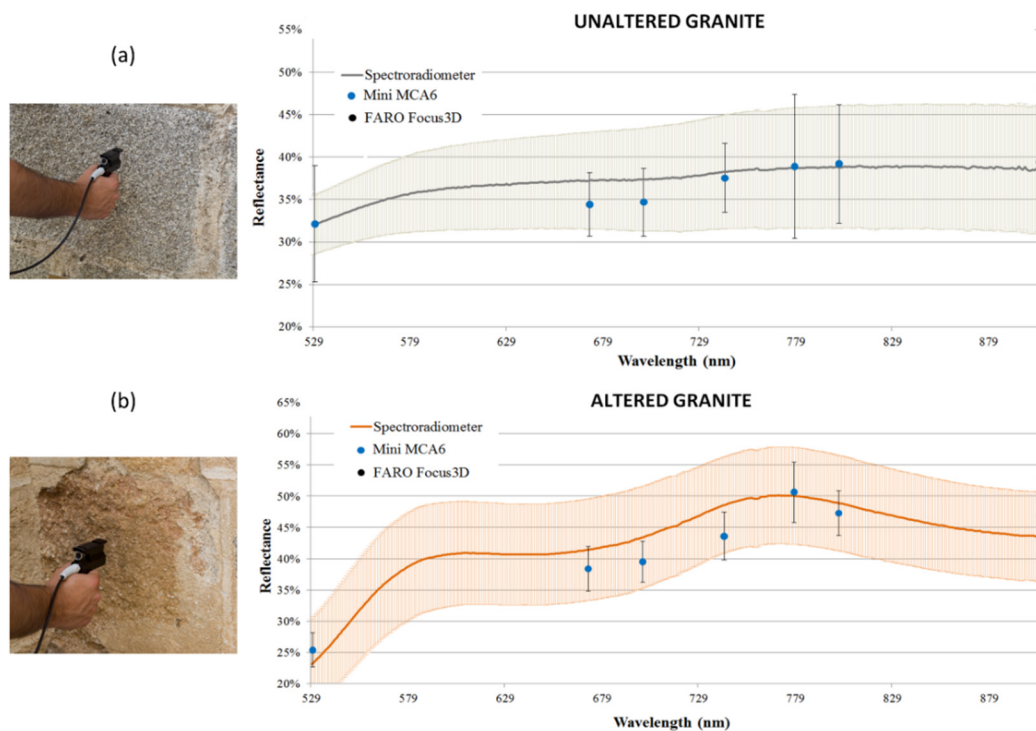
Figure 11. Spectral signatures of the two different types of granites, (**a**) unaltered and (**b**) altered, measured with the ASD spectroradiometer for the wavelength interval covered by the sensors used (Mini MCA6 and FARO Focus3D) where points are obtained from the orthoimages in reflectance values.

Table 4. Confusion matrix of the Mini MCA6 unsupervised classification.

	Moisture	Mortar	Altered Granite	Unaltered Granite	Wood	User Accuracy
Moisture	40.14%	25.40%	0.54%	33.92%	0.01%	40.14%
Mortar	0.06%	39.11%	59.53%	1.31%	0.00%	39.11%
Altered granite	3.79%	7.69%	73.86%	14.61%	0.05%	73.86%
Unaltered granite	6.56%	5.30%	16.39%	70.75%	1.01%	70.75%
Wood	0.00%	0.00%	0.00%	0.00%	100.00%	100.00%
Producer accuracy	21.10%	57.71%	66.00%	74.28%	94.26%	
				Overall accuracy:		**66.04%**

Table 5. Confusion matrix of the FARO Focus3D unsupervised classification.

	Moisture	Mortar	Altered Granite	Unaltered granite	Wood	User Accuracy
Moisture	52.46%	1.04%	23.17%	19.81%	3.52%	52.46%
Mortar	0.00%	60.46%	37.36%	2.18%	0.00%	60.46%
Altered granite	0.05%	12.81%	78.29%	8.64%	0.20%	78.29%
Unaltered granite	0.29%	1.49%	21.70%	75.47%	1.04%	75.47%
Wood	0.48%	0.00%	0.00%	0.00%	99.52%	99.52%
Producer accuracy	89.64%	68.32%	68.68%	83.62%	91.81%	
				Overall accuracy:		**74.39%**

To conclude, it should be highlight that the improvement in both the overall accuracy and the Kappa coefficient is significant in the case of working with radiometrically calibrated sensors as opposed to the use uncalibrated ones [17]. The results for the Mini MCA6 have experienced a 24% improvement in terms of overall accuracy and 23% regarding the Kappa coefficient. Furthermore, the improvement from the use of the calibrated FARO Focus3D was of 29% and 35% regarding the overall

accuracy and Kappa coefficient, respectively. Results worsen in the case of the Mini MCA6 due to two factors; the first is that the camera is a passive sensor, so it is sensitive to changes in light conditions and shadow areas during data acquisition. The second error factor is caused by the slave image registration process, as has been mentioned above, due to the errors in the determination of baselines, angular misalignments and the internal parameters of the camera. Any error in those parameters is propagated into the final multispectral orthoimage, being worsened for higher spatial resolutions, where the geometric pixel footprint in the object may differ depending on the wavelength.

4. Conclusions

The work presented in this paper shows a comparison of the classification results from the use of different radiometrically calibrated sensors to detect pathologies in materials of historical buildings façades. By combining the use of two different data acquisition techniques (active and passive), two sensors were examined: a multispectral camera and a 3D laser scanner. The results show the different radiometric responses of the ashlars of a church with different damages levels (mainly moisture). The classification algorithms used for the classification processes were the Fuzzy K-means and the maximum likelihood classification algorithms.

A complete description of the workflow followed is outlined describing the data acquisition, pre-processing (including sensors radiometric calibrations), orthoimages generation and the application of two classification algorithms to assess the final results. Our results show that the most comprehensive sensor for which the best results were obtained is the FARO Focus3D. This is possibly due to the advantage of working in an active way with no need of external radiation. As a result, classification maps were not affected by different lighting conditions during data acquisition. Furthermore, geometric models of the study object can be derived thanks to its data capture. With these models, physical pathologies (such as fissures, desquamations, *etc.*) could be analyzed and both these damages and chemical pathologies could be quantified. However, for the challenge of the registration of 6 wavelength bands, the results from the Mini MCA6 were quite good. Considering all those issues and with the experience of working with these sensors in previous studies, it is concluded that the radiometric calibration of the sensors is crucial since it contributes to improving the accuracy of the outcomes (a 35% Kappa coefficient improvement in the case of the FARO Focus3D). Thus, a sensor combination with laser scanning as a primary choice is the best solution for pathology detection and quantification. By adding the intensity information to visible or multispectral information, results of classification improve in a quantitative and a qualitative way.

In future work, the use of a hyperspectral camera or another laser scanner operating in the shortwave infrared as a complement of the sensors proposed will improve the pathologies detection and the overall accuracy results since the spectral resolution of the study would be increased. In addition, and for non-carved historical buildings, the roughness of the façade would be calculated from the scan points in order to have additional data of the materials so it can help in the discrimination process. Finally, and regarding the data acquisition of passive sensors, constant favorable climatic conditions will be planned so that the accuracy of its classification results may be significantly improved.

Author Contributions: All authors conceived, designed and performed the experimental campaign. Susana del Pozo and Pablo Rodriguez-Gonzálvez implemented the methodology and analyzed the results. Susana del Pozo wrote the manuscript and all authors read and approved the final version.

Conflicts of Interest: The authors declare no conflict of interest.

References

1. Marszalek, M. Deterioration of stone in some monuments exposed to air pollution: A Cracow case study. In *Air Pollution and Cultural heritage*; Taylor and Francis: London, UK, 2004; pp. 151–154.

2. Corvo, F.; Reyes, J.; Valdes, C.; Villaseñor, F.; Cuesta, O.; Aguilar, D.; Quintana, P. Influence of air pollution and humidity on limestone materials degradation in historical buildings located in cities under tropical coastal climates. *Water Air Soil Pollut.* **2010**, *205*, 359–375. [CrossRef]

3. Fort, R.; de Azcona, M.L.; Mingarro, F. Assessment of protective treatment based on their chromatic evolution: Limestone and granite in the Royal Palace of Madrid, Spain. In *Protection and Conservation of the Cultural Heritage in the Mediterranean Cities*; Galan, E., Zezza, F., Eds.; CRC Press/Balkema: Sevilla, Spain, 2002; pp. 437–441.

4. Weritz, F.; Kruschwitz, S.; Maierhofer, C.; Wendrich, A. Assessment of moisture and salt contents in brick masonry with microwave transmission, spectral-induced polarization, and laser-induced breakdown spectroscopy. *Int. J. Archit. Herit.* **2009**, *3*, 126–144. [CrossRef]

5. Lambers, K.; Eisenbeiss, H.; Sauerbier, M.; Kupferschmidt, D.; Gaisecker, T.; Sotoodeh, S.; Hanusch, T. Combining photogrammetry and laser scanning for the recording and modelling of the late intermediate period site of pinchango alto, Palpa, Peru. *J. Archaeol. Sci.* **2007**, *34*, 1702–1712. [CrossRef]

6. González-Aguilera, D.; Gómez-Lahoz, J.; Sánchez, J. A new approach for structural monitoring of large dams with a three-dimensional laser scanner. *Sensors* **2008**, *8*, 5866–5883. [CrossRef]

7. Buckley, S.J.; Howell, J.; Enge, H.; Kurz, T. Terrestrial laser scanning in geology: Data acquisition, processing and accuracy considerations. *J. Geol. Soc.* **2008**, *165*, 625–638. [CrossRef]

8. Armesto, J.; Ordóñez, C.; Alejano, L.; Arias, P. Terrestrial laser scanning used to determine the geometry of a granite boulder for stability analysis purposes. *Geomorphology* **2009**, *106*, 271–277. [CrossRef]

9. Höfle, B.; Pfeifer, N. Correction of laser scanning intensity data: Data and model-driven approaches. *ISPRS J. Photogramm. Remote Sens.* **2007**, *62*, 415–433. [CrossRef]

10. Kaasalainen, S.; Kukko, A.; Lindroos, T.; Litkey, P.; Kaartinen, H.; Hyyppä, J.; Ahokas, E. Brightness measurements and calibration with airborne and terrestrial laser scanners. *IEEE Trans. Geosci. Remote Sens.* **2008**, *46*, 528–534. [CrossRef]

11. Franceschi, M.; Teza, G.; Preto, N.; Pesci, A.; Galgaro, A.; Girardi, S. Discrimination between marls and limestones using intensity data from terrestrial laser scanner. *ISPRS J. Photogramm. Remote Sens.* **2009**, *64*, 522–528. [CrossRef]

12. Lichti, D.D. Spectral filtering and classification of terrestrial laser scanner point clouds. *Photogramm. Record* **2005**, *20*, 218–240. [CrossRef]

13. Mather, P.; Tso, B. *Classification Methods for Remotely Sensed Data*, 2nd ed.; CRC Press: Boca Raton, FL, USA, 2009.

14. Lerma, J.L. Multiband *versus* multispectral supervised classification of architectural images. *Photogramm. Record* **2001**, *17*, 89–101. [CrossRef]

15. Lerma, J.L. Automatic plotting of architectural facades with multispectral images. *J. Surv. Eng.* **2005**, *131*, 73–77. [CrossRef]

16. Ruiz, L.; Lerma, J.; Gimeno, J. Application of computer vision techniques to support in the restoration of historical buildings. *ISPRS Int. Arch. Photogramm. Remote Sens. Spatl. Inf. Sci.* **2002**, *34*, 227–230.

17. Hemmleb, M.; Weritz, F.; Schiemenz, A.; Grote, A.; Maierhofer, C. Multi-spectral data acquisition and processing techniques for damage detection on building surfaces. In Proceedings of the ISPRS Commission V Symposium "Image Engineering and Vision Metrology", Dresden, Germany, 25–27 September 2006.

18. Del Pozo, S.; Herrero-Pascual, J.; Felipe-García, B.; Hernández-López, D.; Rodríguez-Gonzálvez, P.; González-Aguilera, D. Multi-sensor radiometric study to detect pathologies in historical buildings. *ISPRS Int. Arch. Photogramm. Remote Sens. Spat. Inf. Sci.* **2015**, *XL-5/W4*, 193–200. [CrossRef]

19. López, D.H.; García, B.F.; Piqueras, J.G.; Alcázar, G.V. An approach to the radiometric aerotriangulation of photogrammetric images. *ISPRS J. Photogramm. Remote Sens.* **2011**, *66*, 883–893. [CrossRef]

20. Del Pozo, S.; Rodríguez-Gonzálvez, P.; Hernández-López, D.; Felipe-García, B. Vicarious radiometric calibration of a multispectral camera on board an unmanned aerial system. *Remote Sens.* **2014**, *6*, 1918–1937. [CrossRef]

21. Kaasalainen, S.; Ahokas, E.; Hyyppä, J.; Suomalainen, J. Study of surface brightness from backscattered laser intensity: Calibration of laser data. *IEEE Geosci. Remote Sens. Lett.* **2005**, *2*, 255–259. [CrossRef]

22. Soudarissanane, S.; Lindenbergh, R.; Menenti, M.; Teunissen, P. Scanning geometry: Influencing factor on the quality of terrestrial laser scanning points. *ISPRS J. Photogramm. Remote Sens.* **2011**, *66*, 389–399. [CrossRef]

23. Al-amri, S.S.; Kalyankar, N.V.; Khamitkar, S.D. A comparative study of removal noise from remote sensing image. *Int. J. Comput. Sci. Issue* **2010**, *7*, 32–36.

24. Zheng, Y.; Lin, S.; Kambhamettu, C.; Yu, J.; Kang, S.B. Single-image vignetting correction. *IEEE Trans. Pattern Anal. Mach. Intell.* **2009**, *31*, 2243–2256. [CrossRef] [PubMed]

25. Reshetyuk, Y. *Self-Calibration and Direct Georeferencing in Terrestrial Laser Scanning. Doctoral Thesis in Infrastructure, Geodesy*; Royal Institute of Technology (KTH): Stockholm, Suecia, 2009.

26. Honkavaara, E.; Arbiol, R.; Markelin, L.; Martinez, L.; Cramer, M.; Bovet, S.; Chandelier, L.; Ilves, R.; Klonus, S.; Marshal, P. Digital airborne photogrammetry—A new tool for quantitative remote sensing? A state-of-the-art review on radiometric aspects of digital photogrammetric images. *Remote Sens.* **2009**, *1*, 577–605. [CrossRef]

27. Biggar, S.; Slater, P.; Gellman, D. Uncertainties in the in-flight calibration of sensors with reference to measured ground sites in the 0.4–1.1 µm range. *Remote Sens. Environ.* **1994**, *48*, 245–252. [CrossRef]

28. Dinguirard, M.; Slater, P.N. Calibration of space-multispectral imaging sensors: A review. *Remote Sens. Environ.* **1999**, *68*, 194–205. [CrossRef]

29. Kaasalainen, S.; Krooks, A.; Kukko, A.; Kaartinen, H. Radiometric calibration of terrestrial laser scanners with external reference targets. *Remote Sens.* **2009**, *1*, 144–158. [CrossRef]

30. Jelalian, A.V. *Laser Radar Systems*; Artech House: New York, NY, USA, 1992.

31. Bourke, P. An algorithm for interpolating irregularly-spaced data with applications in terrain modelling. In Proceedingsof the Pan Pacific Computer Conference, Beijing, China, 1 January 1989.

32. Attene, M. A lightweight approach to repairing digitized polygon meshes. *Vis. Comput.* **2010**, *26*, 1393–1406. [CrossRef]

33. Kraus, K. *Photogrammetry: Geometry from Images and Laser Scans*, 2nd ed.; Walter de Gruyter: Berlin, Germany, 2007.

34. Albertz, J.; Kreiling, W. *Photogrammetrisches Taschenbuch*; Herbert Wichmann Verlag: Berlin, Germany, 1989.

35. Bezdek, J.C. *Pattern Recognition with Fuzzy Objective Function Algorithms*; Plenum Press: New York, NY, USA, 1981.

36. Kannan, S.; Sathya, A.; Ramathilagam, S.; Pandiyarajan, R. New robust fuzzy C-Means based gaussian function in classifying brain tissue regions. In *Contemporary Computing*; Ranka, S., Aluru, S., Buyya, R., Chung, Y.-C., Dua, C., Grama, A., Gupta, S.K.S., Kumar, R., Phoha, V.V., Eds.; Springer: Berlin, Germany, 2009; pp. 158–169.

37. Richards, J.A. *Remote Sensing Digital Image Analysis*; Springer: Berlin, Germany, 1999; Volume 3.

38. Lillesand, T.; Kiefer, R.W.; Chipman, J. *Remote Sensing and Image Interpretation*, 7th ed.; John Wiley & Sons: Hoboken, NJ, USA, 2015.

39. García, F.A.F. *La Invención de la Iglesia de san Segundo. Cofrades y Frailes Abulenses en los Siglos xvi y xvii*; Institución Gran Duque de Alba: Ávila, Spain, 2006.

40. Rantanen, J.; Antikainen, O.; Mannermaa, J.-P.; Yliruusi, J. Use of the near-infrared reflectance method for measurement of moisture content during granulation. *Pharm. Dev. Technol.* **2000**, *5*, 209–217. [CrossRef] [PubMed]

41. Davis, S.M.; Landgrebe, D.A.; Phillips, T.L.; Swain, P.H.; Hoffer, R.M.; Lindenlaub, J.C.; Silva, L.F. *Remote Sensing: The Quantitative Approach*; McGraw-Hill International Book Co.: New York, NY, USA, 1978.

42. Tolpekin, V.; Stein, A. Quantification of the effects of land-cover-class spectral separability on the accuracy of markov-random-field-based superresolution mapping. *IEEE Trans. Geosci. Remote Sens.* **2009**, *47*, 3283–3297. [CrossRef]

43. Cohen, J. Weighted kappa: Nominal scale agreement provision for scaled disagreement or partial credit. *Psychol. Bull.* **1968**, *70*, 213–220. [CrossRef] [PubMed]

4.2. Automatización en la detección de humedades en estructuras de hormigón mediante hibridación sensorial

Este subcapítulo contiene el artículo *Automatic mapping of moisture affectation in exposed concrete structures by fusing different wavelength remote sensors* (Mapeo automático de humedades en estructuras de hormigón mediante la fusión de sensores remotos de diferente longitud de onda) publicado en Noviembre de 2015 en la revista internacional *Structural Control and Health Monitoring*.

4.2.1. Resumen

El objetivo principal de este trabajo consistió en analizar la viabilidad de automatizar los procesos de inspección de humedades en estructuras de hormigón a través del análisis y procesado de datos multiespectrales procedentes de sensores geomáticos. Para aumentar el rango espectral de estudio y poder caracterizar mejor esta patología un total de cuatro sensores, dos sistemas láser activos y dos cámaras digitales (una convencional y una multiespectral), fueron analizados abarcando con ello los rangos visible, infrarrojo cercano e infrarrojo de onda corta. Con el fin de automatizar al máximo el proceso y reducir los tiempos de procesado de datos se prescindió de la calibración radiométrica de los sensores. Además, para analizar los resultados se emplearon algoritmos de clasificación automáticos de imagen.

La fusión sensorial se consiguió tras varios procesamientos geométricos de los datos: (i) transformación de las nubes de puntos 3D procedentes de los láser escáner a ortoimágenes y (ii) corrección y registro de las imágenes procedentes de los sensores pasivos. Finalmente, y tras aplicar una metodología automática de clasificación no supervisada, fue posible analizar de los diferentes grados de humedad contrastando los resultados obtenidos con los ofrecidos por la inspección visual realizada por un experto.

Tras la realización de este estudio se concluyó que si bien los sensores pasivos ofrecen una mayor resolución espectral, en cuanto a número de

bandas, que la ofrecida por los láser escáner terrestres (mono-espectrales), los últimos dieron mejores resultados aun cuando no se llevó a cabo la calibración radiométrica de los mismos. Esto se debe a que son sensores que no están influenciados por los cambios en las condiciones lumínicas durante la duración de la toma de datos. Sin embargo, para estos dispositivos se observa una disminución de la señal de retorno proporcional al cuadrado de la distancia de la adquisición y hay que corregirlos de este hecho. Tras realizar un análisis de varianza, se determinó que el rango espectral más adecuado para la detección de humedades es el infrarrojo, concretamente las bandas de 778, 905 y 1550 nm de longitud de onda destacando que los mejores resultados fueron obtenidos con los datos capturados en infrarrojo de onda corta (1550 nm). Tras la realización de este trabajo se validada la automatización del proceso de detección de diferentes niveles de humedad en estructuras de hormigón haciendo uso de sensores no calibrados que preferiblemente trabajen en el rango infrarrojo. Además de la detección de distintos grados de humedad, y gracias a la utilización de sensores activos, fue posible cuantificar esos niveles de humedad superficiales.

Automatic mapping of moisture affectation in exposed concrete structures by fusing different wavelength remote sensors

B. Conde[1], S. Del Pozo[2], B. Riveiro[1,*,†] and D. González-Aguilera[2]

[1]*Department of Materials Engineering, Applied Mechanics and Construction, School of Industrial Engineering, University of Vigo, Vigo 36208, Spain*
[2]*Department of Cartographic and Land Engineering, High School of Ávila, University of Salamanca, Ávila 05003, Spain*

SUMMARY

Water content is a critical parameter for the early detection of moisture degradation in exposed concrete structures. Traditionally, visual inspection is the most extended procedure to detect superficial pathologies caused by moisture in concrete constructions, principally when access is limited. For such cases, remote sensing is a valuable tool to recover radiometric information useful for detecting and quantifying different degrees of affectation caused by water. This paper presents an approach to identifying and evaluating the water content in a real concrete structure by fusing several sensors recording data in different wavelengths. In particular, a procedure to integrate three-dimensional intensity data collected by two terrestrial laser scanners (Riegl-Z390i and FARO Focus 3D) with two-dimensional radiometric data provided by a six-band multispectral camera and a commercial digital camera (MCA6 Tetracam and Canon EOS 5D) is developed. After data fusion in a two-dimensional space, a multiband image was created for further spectral analysis. Finally, an unsupervised classification using clustering algorithms was performed to identify the degrees of affectation and the most suitable remote sensor for moisture mapping. Comparisons between the sensors used in this survey reveal that intensity imagery from both laser scanners has high potential for the recognition and characterisation of the degree of moisture in this type of structure. Copyright © 2015 John Wiley & Sons, Ltd.

1. INTRODUCTION

The main cause of degradation in engineering constructions, and more specifically in reinforced concrete structures, is the influence of meteorological conditions [1]. This damage is caused, generally, by the presence of water and its influence on the corrosion of the steel bars [2] that may result in the presence of external cracks exposing the steel reinforcement to the atmospheric environment [3]. Thus, when the concrete is dry, the corrosion shows negligible values (below $0.1 \, \mu A/cm^2$). These values increase when the humidity goes up to maximum values of around $100 \, \mu A/cm^2$ [4]. In addition, it is common that vegetation appears with the presence of moisture in wet areas, which is an additional deterioration factor for the structure's conservation because it increases water infiltration [5].

Therefore, surveillance and maintenance are very important tasks for the conservation of these structures, especially in areas of greatest exposure to degradation factors. Currently, routine inspections are performed visually without resulting in quantitative assessments of the conservation status and which rely on experience-based expertise that must be developed over years of practice. Remote sensing would be a good solution to analyse remotely the deterioration level of the materials in these cases

---

*Correspondence to: B. Riveiro, Department of Materials Engineering, Applied Mechanics and Construction, School of Industrial Engineering, University of Vigo, Torrecedeira 86, Vigo 36208, Spain.
†E-mail: belenriveiro@uvigo.es

and when structures are inaccessible. Thus, this technology becomes an important tool to assist in the decision-making and the maintenance of damaged structures [6].

The expansion of laser scanning technology towards civil engineering applications is remarkable, particularly for surveying infrastructures with difficult access. In that sense, many works have been reported in the literature for cases, for example of bridges. Laser scanning is a technology of great interest for studying historic masonry bridges where the geometry is closely related to structural performance [7]. In the literature, there are important works such as those presented by [8], software for the quantification of bridge deterioration based on Light Detection and Ranging (LiDAR) data. Furthermore, the combination of other technologies such as infrared thermography, photogrammetry and ground penetrating radar [9] have provided suitable models to conduct simulations of areas affected by moisture content in masonry arch bridges. Ground-penetrating radar is currently applied in the inspection of concrete bridge conditions with a really good accuracy of the results [10]. Ultrasonic [11] and laser scanner [12] methods, meanwhile, are also currently used for this purpose. In this sense, the high potential of remote sensing technologies for assessing concrete bridges is demonstrated.

It is important to note the role of geometry in structural health monitoring using spatial computations. In this sense, the work developed by [13] proposes spatial information systems for the assessment of risk management of large structures. This is in accordance with building information models, the new standards for three-dimensional (3D) modelling accounting not only for geometry but also for semantic and topologic information. Thus, the monitoring of built-up structures can benefit from the full potential of computer technology and can be based on more efficient methods giving a spatial perspective to inspection data. Therefore, the growth of standard information models for civil engineering infrastructures, such as bridge information models [14], promotes the development of new methods to accomplish the inspection and assessment of the state of built-up constructions.

Based on the advances in geomatic technologies and the new standards for 3D modelling and the monitoring of built-up structural systems, this paper presents an approach to detecting and quantifying the area affected by the presence of surface moisture in concrete structures by fusing multispectral data registered by both 3D and two-dimensional (2D) remote sensors. The aim consists of comparing four different sensors and determining which one is the best to identify, quantify and analyse moisture damage in concrete structures. To this end, both the geometric transformations and the spectral analysis are described in Section 3 of this paper. The data set will be subjected to three different cluster-number classifications, and the results are presented in Section 4. The final section is devoted to outlining the main conclusions.

2. THEORETICAL BACKGROUND

Remote sensing techniques and methods allow the automatic detection of damage in built-up constructions with an accurate georeferencing and geometric characterisation of pathologies [15]. In recent years, laser scanning has experienced a significant expansion because of its potential for providing the spatial information of 3D objects in a massive way. However, laser scanners not only provide information about the geometry of the objects but also information about the portion of the energy reflected by an object's surface, which depends on its spectral reflectance characteristics. The backscatter generated when the laser beam strikes the object's surface is recorded by most LiDAR instruments as a function of time [16,17] or the returned phase of the laser beam (Figure 1).

The amount of energy returned in LiDAR systems is modelled through Equation 1, the radar equation. This model establishes that the returned energy is a function of some sensor parameters, the measurement geometry and the cross-section of the target [18], given by

$$P_r = \frac{P_t}{4\pi} \cdot \frac{D_r{}^2}{R^4 \beta_t{}^2} \cdot \sigma \tag{1}$$

where P_r is the received signal power from the transmitted laser pulse after reflecting on the target, P_t is the transmitted signal power, D_r is the diameter of the optical receiver, R is the slant range to the target from the sensor and β_t is the laser beam width.
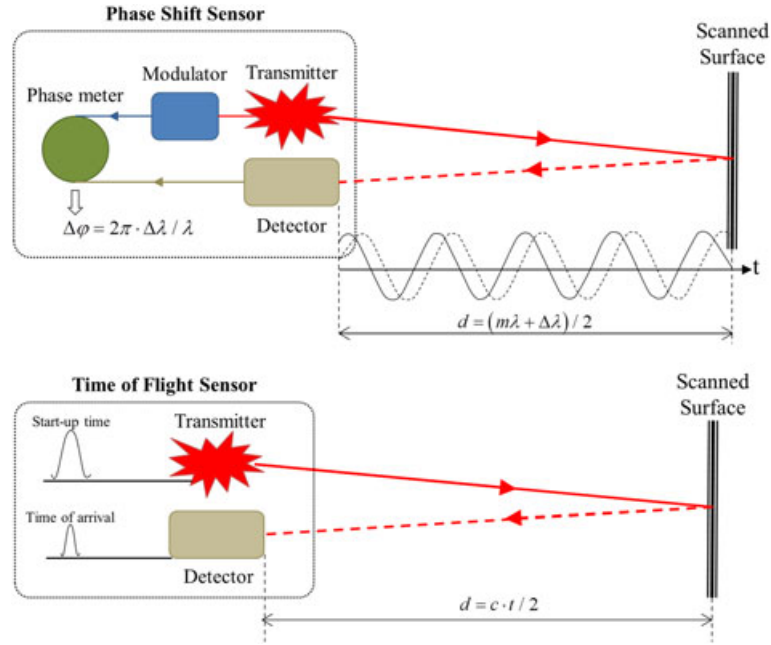
Figure 1. Sketch of a LiDAR sensor for two different principles of operation: the phase-shift and time-of-flight methods being $\Delta\phi$ the phase shift, λ the wavelength, m the ambiguity or integer number of cycles, c the speed of light and t the round-trip time.

The effective target cross-section σ can be expressed as a function of the scattering solid angle of the target, as

$$\sigma = \frac{4\pi P_r}{\Omega_s P_i} A_{lf} \tag{2}$$

where Ω_s is the solid angle of the scattered radiant flux, P_i is the incident radiant flux (equal to the transmitted laser power P_t) and A_{lf} is the laser footprint area at the target.

Also, the effective target cross-section has a proportionality of the $\cos\alpha$ when the incidence angle α is greater than 0.

The biconical reflectance ρ [19] is defined as the ratio of the reflected to the incident flux. Materials with Lambertian characteristics may be discriminated attending to the response of this property through the spectrum, and this is usually denoted by a spectral curve. Knowing the reflectance value for a specific wavelength would allow the identification of the material being observed. However, as previous equations reveal, the discrimination of materials by using laser intensity is not immediate. Furthermore, it must be taken into account that the amount of returned energy depends not only on the previous parameters but also on power losses due to the sensor and the atmosphere, η_{sys} and η_{atm}, respectively. The first loss is caused by all the optical components of the LiDAR sensor and affects the optical transmission efficiency. The second loss refers to the transmission efficiency of the atmosphere between the sensor and the target (at range R). After these assumptions, the amount of return power registered by a LiDAR system may be expressed by Equation 3 [20]:

$$P_r = \frac{P_t \cdot D_r^{\,2} \cdot \rho}{4R^2} \eta_{sys} \cdot \eta_{atm} \cdot \cos\alpha \tag{3}$$

Laser scanners have the ability of recording the return power as a function of time after transmission, and depending on the objects hit by the laser beam, there might be several function peaks. These peaks denote objects located at different ranges, and depending on the intensity recorded, the spectral characteristics may be derived. While most commercial systems do not provide information about proprietary pulse detection algorithms, the usual procedures are based on computing a threshold, the centre of gravity, or are even based on finite differences using numerical derivatives or others. The first

scanners provided only a return echo, but now, most of the instruments register several echoes with their respective intensity attribute, normally at 8-bit, 12-bit or 16-bit resolution. The most modern laser scanning instruments digitalise not only a few echoes but also the full waveform [21].

Traditionally, remote sensing is classified into active and passive sensors. Contrary to laser scanning, photography has been included in the passive methods because it records reflected solar energy in different bands of the electromagnetic spectrum. However, the information collected from 3D space is registered on a planar sensor through a central projection.

Intersection is an application in analytical photogrammetry that allows the assignment of the colour registered in an image to a point in the object space after calculating the orientation of the image. So, if the spatial coordinates of an object are known, the image coordinates can be calculated through the collinearity equations (Equation 4). The collinearity condition establishes that the camera station, any object point and its photo image all lie along a straight line in 3D space.

$$
\begin{aligned}
x_a &= -f\left[\frac{m_{11}(X_A - X_0) + m_{12}(Y_A - Y_0) + m_{13}(Z_A - Z_0)}{m_{31}(X_A - X_0) + m_{32}(Y_A - Y_0) + m_{33}(Z_A - Z_0)}\right] \\
y_a &= -f\left[\frac{m_{21}(X_A - X_0) + m_{22}(Y_A - Y_0) + m_{33}(Z_A - Z_0)}{m_{31}(X_A - X_0) + m_{32}(Y_A - Y_0) + m_{33}(Z_A - Z_0)}\right]
\end{aligned}
\tag{4}
$$

where x_a y_a) are the image coordinates, f is the principal distance, (X_0 Y_0 Z_0) are the spatial coordinates of the projection centre and (X_A Y_A Z_A) are the spatial coordinates of the object.

Conversely, if both the image and spatial coordinates of a minimum of four points are known, the orientation of the projection centre can be obtained. This is general practice when texturing point clouds. However, this method is costly, and its application to automation in the inspection and mapping of superficial pathologies may be limited. To ease the last goal, this paper proposes a method that allows the registration of several sources of spectral data and the automatic classification of moisture areas. The two main purposes of this study are as follows: first, to analyse the spectral response of moisture in concrete walls and second, to determine which remote sensor and spectral range regarding those proposed are the most suitable to conduct the inspection of such pathologies.

3. MATERIALS AND METHODS

3.1. Equipment

Both active and passive remote sensing techniques were applied in this study. The active sensors involve two terrestrial laser scanners, and the passive sensors comprise a multispectral camera and an RGB single-lens reflex (SLR) digital camera. Figure 2 shows the different wavelength sensors used in this research.

The first laser scanner was the Riegl-Z390i, a time-of-flight laser scanner that emits pulses at a 1550 nm wavelength. This device measures distances in the range of 1–400 m with a point

Figure 2. Sensors used for data collection. From left to right as active sensors: RIEGL-Z390i and FARO Focus 3D. As passive sensors: MCA6 Tetracam and Canon EOS 5D.

measurement rate of 11 000 points per second. It has a nominal accuracy of 6 mm at a distance of 50 m in normal lighting and reflectivity conditions and a beam divergence of 0.3 mrad, equivalent to the 30 mm per 100 m range. The viewing field extends 80° vertically and 360° horizontally with a 0.001° of angular resolution [22]. The signal intensity received by the sensor system is recorded in 8-bit format.

The other laser scanner was the FARO Focus 3D, which measures distances using the principle of phase shift at a wavelength of 905 nm. This device measures distances in a range of 0.60–120 m with a point measurement rate of 976 000 points per second. It has an accuracy of 0.015° in normal lighting and reflectivity conditions and a beam divergence of 0.19 mrad, equivalent to the 19 mm per 100 m range. The field of view extends 300° vertically and 360° horizontally with a 0.009° of angular resolution, and the returning intensity is recorded in 11-bit format. Additionally, this laser scanner includes a double compensator in the horizontal and vertical axes.

The lightweight Multiple Camera Array, MCA6 (Tetracam, Chatsworth, CA, USA), was a multispectral sensor (visible–near infrared) of 10-bit data and a resolution of 1280×1024 pixels. The sensor was equipped with six bands of 530, 672, 700, 742, 778 and 801 nm. The recording of the images is time triggered, and it has a focal length of 9.6 mm and a pixel size of 5.2 μm [23].

The Canon EOS 5D (Canon, Tokyo, Japan) is a high-resolution SLR digital camera chosen to acquire information relating to the visible range of the spectrum with a resolution of 5616×3744 pixels. This camera uses a complementary metal–oxide–semiconductor sensor. The focal length is 24 mm, and it shoots 3.9 frames per second [24].

3.2. Methodological procedure

This study, motivated by the radiometric data fusion and sensor integration, needs to follow specific methodology and data processing to finally analyse the data from the mentioned sensors all together. To this end, the proposed methodology has three main stages, as outlined in Figure 3. In the first phase, a series of geometric transformations must be applied to the data trying to have them on the same scale and reference system. Provided as input data point clouds and images, these transformations consisted of point cloud processing to obtain orthoimages and the rectification of images collected by the passive sensors. The second stage was the registration of the data to a common reference coordinate system and scale. Thus, a multidimensional array was created with an 11-band matrix (two bands from laser scanners, six from the multispectral camera and three from the SLR camera) where digital levels represented the reflected energy for the different wavelengths registered by the sensors. The last stage consisted of the automatic mapping of the concrete wall under study according to different levels of moisture by an unsupervised classification of the set of 11 images. Finally, for each degree of moisture class, the analysis of variance test was performed to evaluate significant differences among the different sensors used for the survey.

3.2.1. Geometric transformations. The first step to building a multispectral array for the remote evaluation of moisture in concrete structures is the registration of the data collected by the different sensors in a common geometric space. Because raw data are registered in both 3D space (laser scanning) and 2D projective space (RGB and multispectral cameras), the information had to be converted into a common 2D space through orthogonal projections.

From 3D laser scanning to 2D raster images
To transform 3D data into orthogonal 2D raster structures (Figure 4), a rasterisation process was developed using MATLAB software (The MathWorks, Inc., Natick, MA, USA) [5].

The projection plane was computed as the plane that best fits the point cloud in the structure wall. This operation was computed by hyper-planar fitting using orthogonal regression. This model uses least squares where the errors are measured orthogonally to the proposed plane. Once this plane is
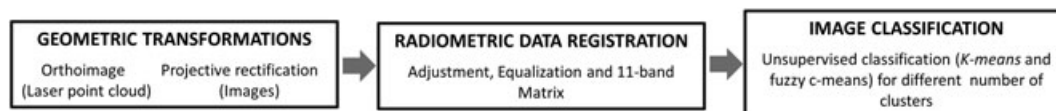
Figure 3. Workflow developed for the assessment of moisture damage in concrete structures.

Point cloud in 3D space

Point cloud projected in raster structure
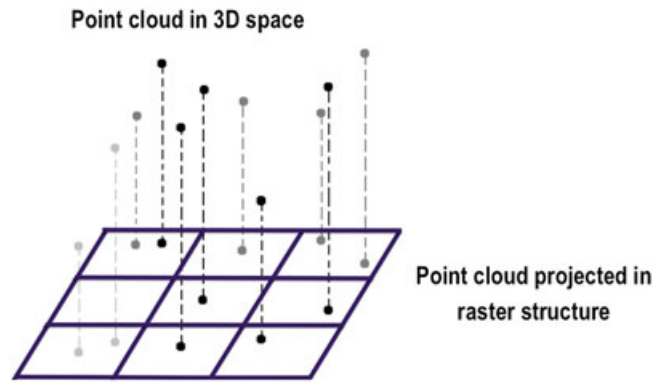
Figure 4. Conversion of a three-dimensional (3D) point cloud into a raster image.

obtained, the orthogonal projection of the points forming the 3D point cloud is immediate. Given a point P of the point cloud defined by its Cartesian components (X_0, Y_0, Z_0) and the normal N to the fitted plane (defined by (A, B, C)), the equation of the line may be expressed by the so-called vector equation (Equation 5) or in the form of implicit equations (Equation 6):

$$(X, Y, Z) = (X_0 Y_0 Z_0) + \lambda(A, B, C) \tag{5}$$

Here, λ is any scalar.

$$\frac{(X - X_0)}{A} = \frac{(Y - Y_0)}{B} = \frac{(Z - Z_0)}{C} \tag{6}$$

These equations, together with the implicit equation of the previous fitted plane (Equation 7), define the point of intersection Q between the line and the plane. The intersection corresponding to each point of the point cloud constitutes the 2D point cloud for rasterisation.

$$N = AX + BY + CZ + d = 0 \tag{7}$$

The next step was to define the intensity attribute for each element in the raster structure. The intensity values of an area S of the structure wall can be defined as a random field model $\{I(s): s \in S \subset \mathrm{R}^2\}$. The set of points of the point cloud covering the element area can be considered as the collection of independent observations at locations $s = \{s_1, s_2, \ldots, s_n\}$ on the random field, denoted by the data vector $I(s) = \{I(s_1), I(s_2), \ldots, I(s_n)\}$.

The raster representation of the point cloud consists of latticing its continuous domain S and computing a value of intensity [a digital number (DN)] for each raster element (pixel). By Equation 8, the intensity of a given pixel, defined by the region P and the corresponding area $|P|$, can be estimated by averaging the random field in P:

$$DN = I(P) = \frac{1}{|P|} \int I(s) ds \tag{8}$$

The value of the $I(P)$ is computed by using the observed data contained in the region of a pixel. Consequently, the spatial resolution of the classification results was constrained by the window size for DN prediction: the pixel size. Figure 5 summarises the process of intensity image generation for the Riegl and the FARO point clouds (1540 and 905 ηm, respectively).

The ground sample distance (GSD) set for our tests (defined through pixel size) was based on the point cloud resolution.

Rectification of imagery: Even if the images were registered in a plane, they need to be corrected of the central perspective in order to convert them into rectified images. This transformation was carried out through a bilinear projective rectification [25] of every single image (six from MCA6 and three from Canon). These sets of images had to be corrected of perspective and adjusted to the size and shape of the orthoimages generated from laser scanning data. Figure 6 illustrates the process of the bilinear rectification performed for planar images.

GEOMETRIC TRANSFORMATIONS
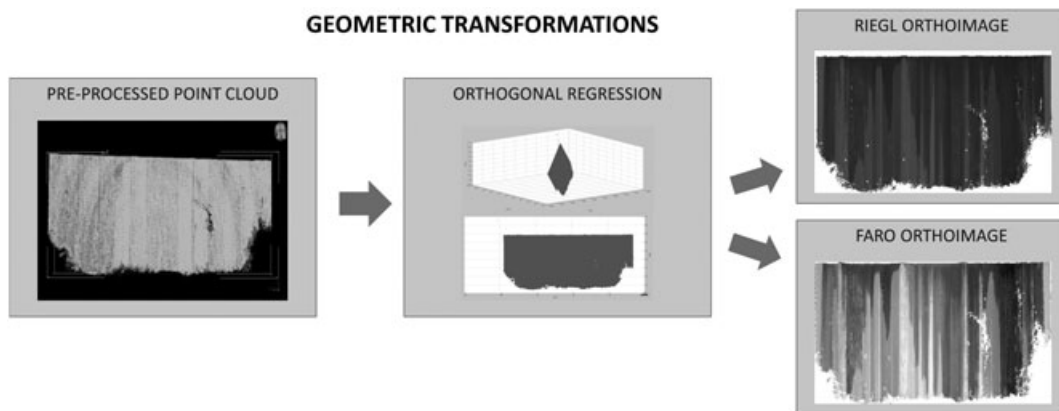
Figure 5. Geometric transformations of the laser point clouds.
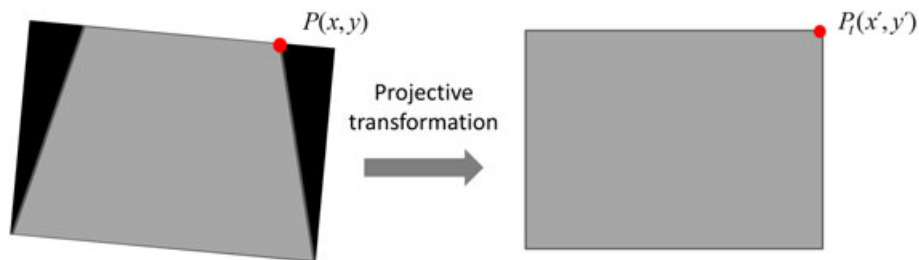
Figure 6. Projective rectification of images acquired with digital cameras.

Being x and y the coordinates of a point P in raw images, $\begin{pmatrix} a_1 & a_2 \\ a_3 & a_4 \end{pmatrix}$ the affine transformation that encloses scale and rotation parameters, $\begin{pmatrix} b_1 \\ b_2 \end{pmatrix}$ the translation vector and $(c_1 \quad c_2)$ the projection vector that encloses the perspective effect along the X and Y axes, respectively, the new coordinates of the points (x' and y') after the transformation were calculated according to Equation 9. A minimum number of four points is necessary to perform a projective rectification, but in our investigation, 14 points were used by applying a least squares adjustment. Also, two of the control points were used to define the rectangular area under study of the abutment.

$$\begin{pmatrix} a_1 & a_2 & b_1 \\ a_3 & a_4 & b_2 \\ c_1 & c_2 & 1 \end{pmatrix} \times \begin{pmatrix} x \\ y \\ 1 \end{pmatrix} = \begin{pmatrix} x' \\ y' \\ 1 \end{pmatrix} \tag{9}$$

3.2.2. Radiometric data registration. Before the classification process, the set of 11 orthoimages had to be registered in a common coordinate system, so those created from laser scanning data were registered to the same coordinate system and boundary used for the previously rectified images. The workflow consisted of using a common GSD (note that laser scanning images have a GSD of 25 mm whereas the rectified images have a GSD of 1 mm). Thus, a bilinear interpolation was used to scale all the rectified images to a GSD of 25 mm. Furthermore, all the images were scaled to the same radiometric resolution (8 bit) optimising the dynamic range of each sensor. Finally, the normalised images were stored as an array (Figure 7) where each element stores the digital number values for the 11 bands.

3.2.3. Image classification. There is a variety of algorithms to perform unsupervised image classification in remote sensing. One of the most frequently used is the *K*-means clustering
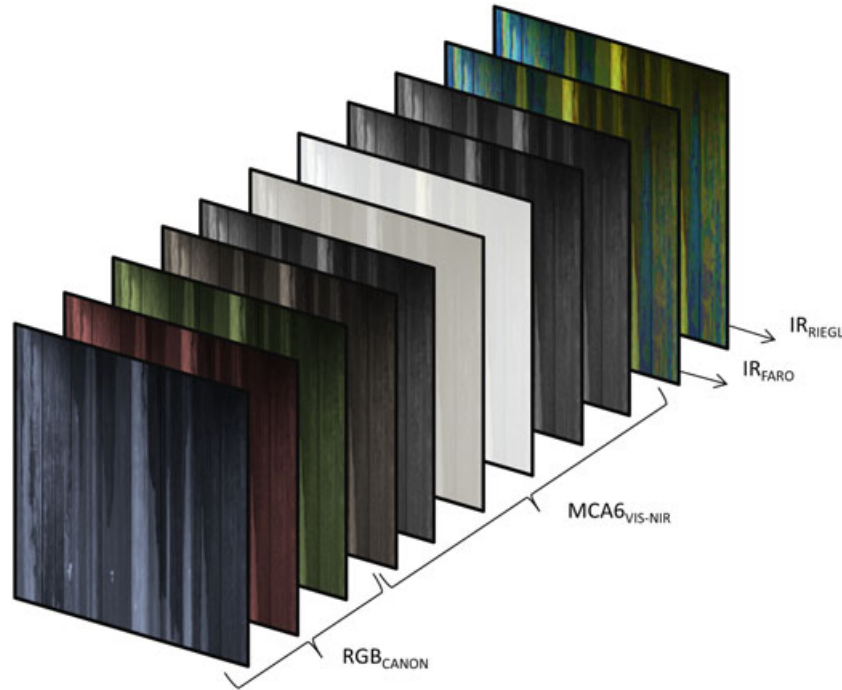
Figure 7. Eleven-band multispectral image.

algorithm [26]. This standard method was first proposed by Stuart Lloyd in 1957, and it separates X observations into K clusters that are represented by their centroids. Each observation belongs to the cluster with the nearest centre of mass. The centre of each cluster is solved by finding the minimum of a sum-of-squares cost function using coordinate descent. Therefore, the aim is to minimise the function presented in Equation 10:

$$P(W,Q) = \sum_{l=1}^{k} \sum_{i=1}^{n} w_{i,l} d(X_i, Q_l) \tag{10}$$

where W is an $n \times k$ partition matrix, $Q = \{Q_1, Q_2, \ldots, Q_k\}$ is a set of objects in the same object domain and d is the squared Euclidean distance between two objects.On the other hand, the fuzzy C-means clustering is very similar to the K-means algorithm where each observation can concurrently belong to multiple clusters [27]. The objective of the algorithm (developed by Dunn in 1977 and improved by Bezdek in 1981) is to minimise the function presented in Equation 11 [28]:

$$J_m = \sum_{i=1}^{n} \sum_{l=1}^{k} u^m_{i,l} \|x_i - c_l\|^2, \ 1 \le m < \infty \tag{11}$$

where m is any real number greater than 1, $u_{i,l}$ is the degree of membership of x_i in the cluster l, x_i is the ith of d-dimensional measured data, c_l is the d-dimensional centre of the cluster and $\| * * \|$ is any norm expressing the similarity between any measured data and the centre.

Fuzzy partitioning is carried out through an iterative optimisation of the objective function shown earlier, with the update of membership $u_{i,l}$ and the cluster centres c_l by

$$u_{i,l} = \frac{1}{\sum_{k=1}^{C} \left[\frac{\|x_i - c_l\|}{\|x_i - ck\|} \right]^{\frac{2}{m-1}}}, \ c_l = \frac{\sum_{i=1}^{N} u^m_{il} x_i}{\sum_{i=1}^{N} u^m_{il}}$$

This iteration will stop when $\max_{il}\{|u_{il}^{(k+1)} - u_{il}^{(k)}|\} < \varepsilon$, where ε is a termination criterion between 0 and 1 whereas k are the iteration steps. This method converges to a local minimum or a saddle point of J_m.

In this research, the *K*-means classifier was tested to perform several unsupervised image classifications with different numbers of classes (three, four and five classes referring to degrees of moisture affectation). The goal of this approach is to determine which number of classes presents a more robust classification, and to provide information on which sensor was the most suitable to conduct such investigations.

4. EXPERIMENTAL RESULTS

To test all these remote sensing technologies, a viaduct abutment of the OU-536 road in Ceboliño, Ourense (Spain), was selected (Figure 8). This region is characterised by a high precipitation rate; thus, the roads have a large number of bridges to protect them from the steps of the rivers. The concrete of the abutments in this bridge is visibly affected by the surface run-off of the deck in the rainy season, so it is exposed to a high moisture level. For that reason, it was likely to be a perfect scenario to study moisture. For the data acquisition, a sunny and dry day was selected in order to avoid environmental conditions such as high relative humidity and vapour content that could affect the intensity measurements from the laser scanner sensors over their optimal working conditions.

4.1. Results of the geometric transformations

In order to create intensity images from laser scanning surveys in an identical coordinate system, both point clouds, the one acquired with the FARO Focus and the one acquired with the Riegl scanner, were aligned using 14 ground control points with an acceptable standard deviation of 2 mm. Figure 9 shows the intensity orthoimages from the 3D laser scanners after the orthogonal regression and projection of points on a vertical plane.

Furthermore, Figure 10 shows the results of the perspective rectification for the Canon EOS 5D and MCA6 images. In this way, each image matches with the intensity images created from the point cloud because the control points used for the projective rectification were the same as those used for the point cloud registration (ground control points). As a result of the transformation process, areas without information (in black) were created. However, these areas were excluded from the region of study on the wall.

4.2. Results of the image classification

In order to assess the effectiveness of the proposed approach, three unsupervised classifications were carried out: establishing three, four and five classes. These different situations were studied because an expert inspection only provided a subjective visual ground truth for the visible spectra (Figure 11); however, the purpose of this research is not only to perform the classification automatically but also to determine which band of the spectrum and remote sensor is the most suitable to conduct such inspections. Figure 12 (from top to bottom) shows the classification image from FARO Focus 3D for three, four and five classes, respectively.

Figure 8. Images of a wall of the abutment studied.
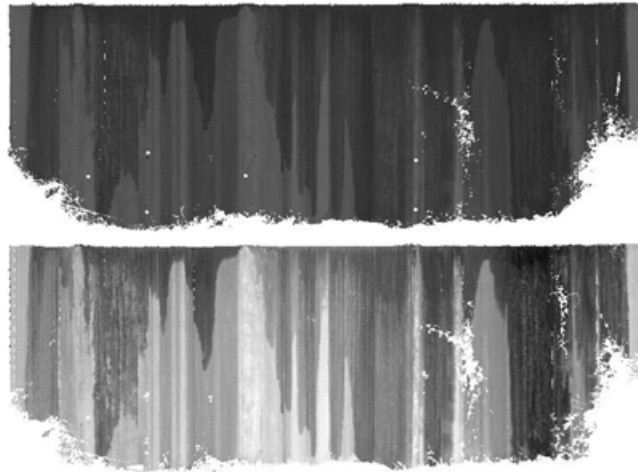
Figure 9. Intensity orthoimages resulting from laser scanner data. From Riegl (on the top) and FARO Focus 3D (on the bottom).

Figure 10. Camera images corrected for perspective. On the left is an RGB image and on the right a band 0 image (778 nm) from the MCA6.
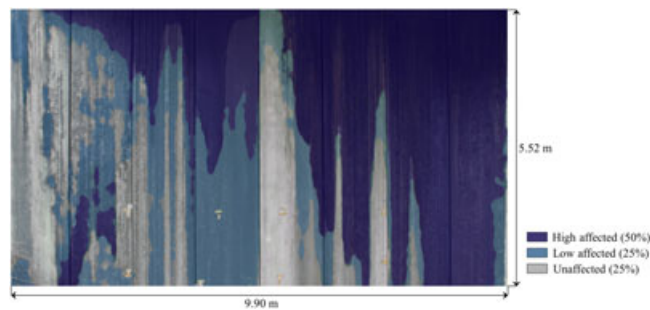
Figure 11. Visual inspection of the wall under study with three different degrees of moisture affectation.

The dark blue class represents areas of higher moisture, followed by green, orange, maroon and finally light blue. The images created from the laser scanning (FARO and Riegl) data provided more homogeneous classes (in terms of spatial representation in the image).

The three classifications even show a high correspondence; a subsequent analysis was necessary in order to identify which is the most suitable number of classes when remote sensing technologies are used. To that end, the spectral signatures of the different degrees of affectation of concrete were calculated according to the three unsupervised classifications performed. In the multiband data registration, an 11-band matrix (Table I) was uploaded, so an analysis of variance test assisted the assessment of the most suitable number of classes.
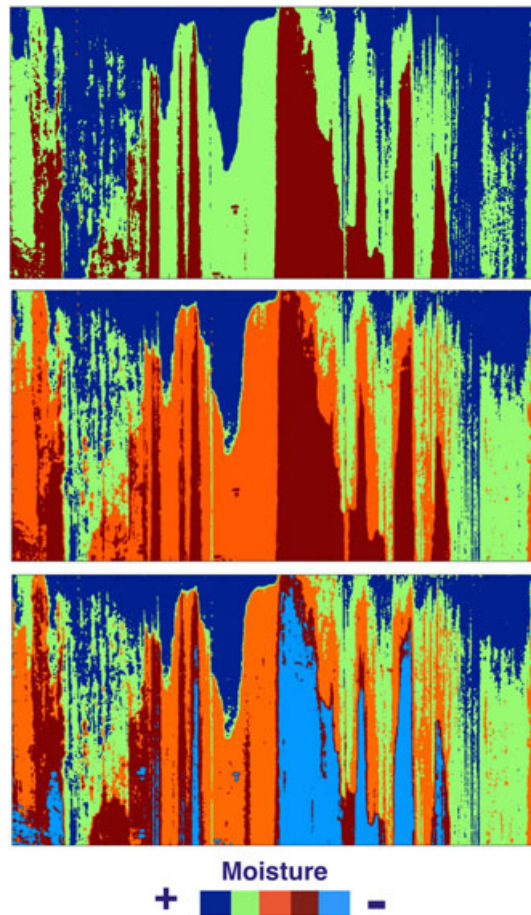
Figure 12. The unsupervised classification results of the FARO image for three, four and five classes corresponding to moisture affectation.

Table I. Sensor bands arranged in ascending order of wavelength.

Sensor	B	G	M0	R	M1	M2	M3	M4	M5	FARO	Riegl
Wavelength (nm)	436	520	530	660	670	700	740	780	800	905	1550

B (blue), G (green) and R (red) are the three bands of the Canon EOS 5D and M0, M1, M2, M3, M4 and M5 the six bands of the MCA6 multispectral camera.

To obtain the spectral signature of each class, in each of the three classifications, the mean and standard deviation of digital levels were calculated by a random selection of 50 pixels per class. Note that these pixel coordinates were marked using the overlapping information from the classification of the 11 spectral bands (Table I). The plotted results are presented in Figure 13.

As Figure 13 shows, when using only three classes to distinguish the degrees of affectation, there were significant differences between the classes. However, when using five classes, the differences between the classes were not so evident, and the variance analysis confirms over-segmentation for classes that did not show significant differences for the passive sensors (only the two laser scanners presented clear differences in the spectral response of the five classes).

The results of the variance analysis show that for the case of four classes with unsupervised classification, most of the sensors presented significant differences between the classes. So, four was selected as the most suitable number of classes for the automatic mapping of moisture affectation in exposed concrete walls.

Finally, an analysis of variance with a significance level $\alpha = 0.01$ was carried out to conclude which sensor was more suitable for detecting and mapping moisture affectation using the four classes
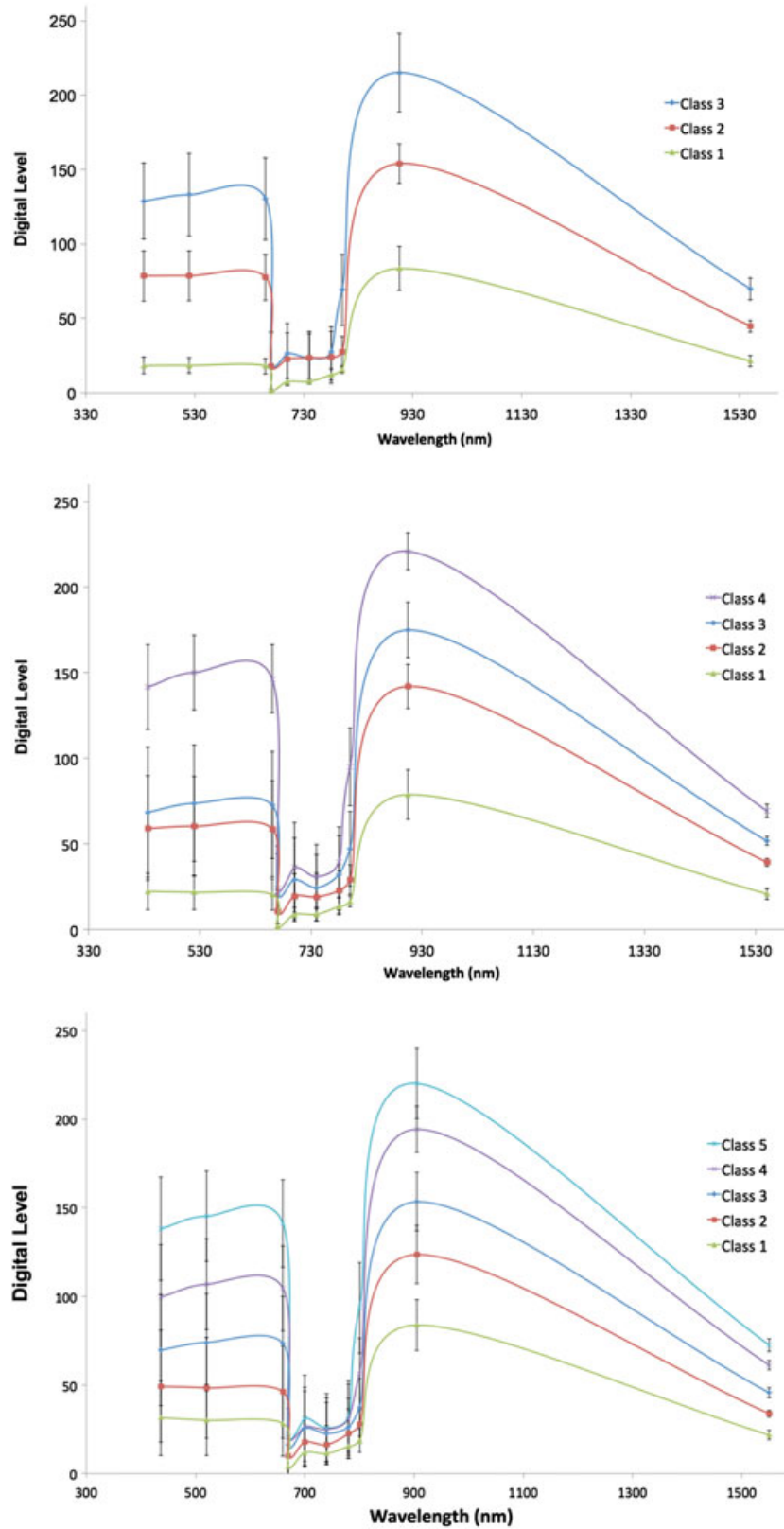
Figure 13. Spectral signatures of the concrete for three, four and five moisture affectation classes, class 1 having the highest moisture.

Table II. Results of the *F*-statistic and *P*-value for each wavelength and conclusions about the significant differences.

Sensor	Bands	Classes	Probability *P*		
			Class 1	Class 2	Class 3
Canon EOS 5D	R		Class 1	Class 2	Class 3
		Class 2	<0.0001	—	
		Class 3	<0.0001	0.0200	—
		Class 4	<0.0001	<0.0001	<0.0001
	G		Class 1	Class 2	Class 3
		Class 2	<0.0001	—	
		Class 3	<0.0001	0.0400	—
		Class 4	<0.0001	<0.0001	<0.0001
	B		Class 1	Class 2	Class 3
		Class 2	<0.0001	—	—
		Class 3	<0.0001	0.1800	—
		Class 4	<0.0001	<0.0001	<0.0001
MCA6 Tetracam	M0		Class 1	Class 2	Class 3
		Class 2	<0.0001		
		Class 3	<0.0001	0.0024	
		Class 4	<0.0001	<0.0001	<0.0001
	M1		Class 1	Class 2	Class 3
		Class 2	<0.0001	—	—
		Class 3	<0.0001	0.0121	—
		Class 4	<0.0001	0.001	0.4600
	M2		Class 1	Class 2	Class 3
		Class 2	<0.0001	—	—
		Class 3	<0.0001	0.0150	—
		Class 4	<0.0001	<0.0001	0.1600
	M3		Class 1	Class 2	Class 3
		Class 2	<0.0001	—	—
		Class 3	<0.0001	0.1100	—
		Class 4	<0.0001	0.0005	0.0900
	M4		Class 1	Class 2	Class 3
		Class 2	<0.0001	—	—
		Class 3	<0.0001	0.0114	—
		Class 4	<0.0001	<0.0001	0.0900
	M5		Class 1	Class 2	Class 3
		Class 2	<0.0001	—	—
		Class 3	<0.0001	<0.0001	—
		Class 4	<0.0001	<0.0001	<0.0001
FARO Focus	FARO		Class 1	Class 2	Class 3
		Class 2	<0.0001	—	—
		Class 3	<0.0001	<0.0001	—
		Class 4	<0.0001	<0.0001	<0.0001
Riegl-Z390i	Riegl		Class 1	Class 2	Class 3
		Class 2	<0.0001	—	—
		Class 3	<0.0001	<0.0001	—
		Class 4	<0.0001	<0.0001	<0.0001

established in the previous analysis. First, the variance analysis indicated that for the set of 11 spectral images, significant differences between the four classes existed. Subsequently, for each spectral band, it was verified whether significant differences between each class and each of the other three classes existed. As shown in Table II, only the images collected by laser scanners and band 0 of the MCA (M0) show significant differences between all the classes. The rest of the bands analysed (R, G, B, M1, M2, M3, M4 and M5) are not capable to properly distinguish between class 2 and class 3, being class 3 also misclassified regarding class 4 for these set of bands of the MCA6 multispectral camera.

From an analysis of Table II it can be summarised that there were no significant differences between some of the classes, specifically between classes 2 and 3 of each of the bands of the Canon camera and between classes 2 and 3, and classes 3 and 4 of the M1, M2, M3 and M4 bands of the MCA6.

The multispectral matrix created can serve also as the basis for calculating vegetation indices, such as the normalized difference vegetation index, by using the MCA6 (with data from 630-nm and 801-nm

bands) or by combining data from FARO Focus 3D (905 nm) and from the red band of the Canon EOS 5D. This is possible because of the spectral behaviour of the chlorophyll pigment of the vegetation in these spectral bands. For the efflorescence phenomenon, visible and near-infrared wave bands can detect it because surfaces with efflorescence have higher reflectance in these spectral ranges. If it is caused by chlorides or sulphates, the short-wave infrared range is more suitable [29]. The Riegl laser scanner could be a solution in such cases. As can be seen in previous works by [30,31], the intensity of laser scanners can be properly used to automatically detect mortar efflorescence and biological crusts.

5. CONCLUSIONS

This paper presents a comparative study to determine which remote sensing technology is more suitable for moisture detection in concrete structures. The proposed methodology advocates analysing different classification images through several unsupervised classifications based on a *K*-means algorithm. For this purpose, a multiband matrix comprising orthoimages collected with several 3D and 2D remote sensors was created. Data fusion was possible after several geometric transformations and radiometric normalisations. Even if the study presented here is a qualitative approach for the moisture content classification of concrete surfaces, it has potential to estimate the area affected by the different degrees of humidity in a quantitative manner ($43\,m^2$ of the $55\,m^2$ studied, 77.33% according to the four-classes classification map).

The unsupervised classification using a *K*-means algorithm demonstrated that the mapping of moisture affectation in exposed concrete structures can be properly achieved. This is verified by the statistical tests that allowed us to conclude the optimal number of classes to be used for mapping the structure under study. Moreover, the evaluation of the spectral signatures built with the 11 spectral images led to the conclusion that both the intensity images created from the laser scanning data (FARO and Riegl scanners) are more suitable for detecting and mapping surface moisture affectation.

This work allows the definition of a robust methodology to compare spectral images captured from remote sensors that are being used more and more to assist the routine inspection of existing infrastructures. Also, the algorithms implemented using MATLAB software permit the use of the methodology presented and are validated in this paper for the routine inspection of exposed concrete structures, thus providing a new set of tools to improve the structural health monitoring of civil engineering structures and buildings.

Because the proposed method cannot directly provide information about the degree of penetration of moisture into the subsurface, future research into the correlation of the external presence of moisture with the degree of degradation inside is required. On the other hand, some studies have been carried out in order to gain qualitative information about the inner characteristics of materials by using ground-penetrating radar and infrared thermography, so new methods that can connect that information with the method proposed in this article will be investigated.

REFERENCES

1. BRIME; 2001. http://www.transport-research.info/Upload/Documents/200310/brimerep.pdf (last accessed April 2015).
2. Isgor OB, Razaqpur AG. Finite element modeling of coupled heat transfer, moisture transport and carbonation processes in concrete structures. *Cement and Concrete Composites* 2004; **26**(1):57–73.
3. Granju J-L, Balouch SU. Corrosion of steel fibre reinforced concrete from the cracks. *Cement and Concrete Research* 2005; **35**:572–577.
4. Andrade C, Alonso C, Sarrıa J. Corrosion rate evolution in concrete structures exposed to the atmosphere. *Cement and Concrete Composites* 2002; **24**(1):55–64.
5. González-Jorge H, Gonzalez-Aguilera D, Rodriguez-Gonzalvez P, Arias P. Monitoring biological crusts in civil engineering structures using intensity data from terrestrial laser scanners. *Construction and Building Materials* 2012; **31**:119–128.

6. Weritz F, Kruschwitz S, Maierhofer C, Wendrich A. Assessment of moisture and salt contents in brick masonry with microwave transmission, spectral-induced polarization, and laser-induced breakdown spectroscopy. *International Journal of Architectural Heritage* 2009; **3**(2):126–144.

7. Carr AJ, Jáuregui D, Riveiro B, Arias P, Armesto J. Structural evaluation of historic masonry arch bridges based on first hinge formation. *Construction and Building Materials* 2013; **47**:569–578.

8. Liu W, Chen S. Reliability analysis of bridge evaluations based on 3D Light Detection and Ranging data. *Structural Control and Health Monitoring* 2013; **20**(12):1397–1409.

9. Solla M, Lagüela S, Riveiro B, Lorenzo H. Non-destructive testing for the analysis of moisture in the masonry arch bridge of Lubians (Spain). *Structural Control and Health Monitoring* 2013; **20**(11):1366–1376.

10. Hugenschmidt J. Concrete bridge inspection with a mobile GPR system. *Construction and Building Materials* 2002; **16**(3):147–154.

11. Rens KL, Greimann LF. Ultrasonic approach for nondestructive testing of civil infrastructure. *Journal of Performance of Constructed Facilities* 1997; **11**(3):97–104.

12. Armesto-González J, Riveiro-Rodríguez B, González-Aguilera D, Rivas-Brea MT. Terrestrial laser scanning intensity data applied to damage detection for historical buildings. *Journal of Archaeological Science* 2010; **37**(12):3037–3047.

13. Qin J, Faber MH. Risk management of large RC structures within spatial information system. *Computer-Aided Civil and Infrastructure Engineering* 2012; **27**(6):385–405.

14. Lee K-M, Lee Y-B, Shim C-S, Park K-L. Bridge information models for construction of a concrete box-girder bridge. *Structure and Infrastructure Engineering* 2012; **8**(7):687–703.

15. Hemmleb M, Weritz F, Schiemenz A, Grote A, Maierhofer C. Multi-spectral data acquisition and processing techniques for damage detection on building surfaces. *Image engineering and vision metrology*, Dresden, Germany, 2006

16. Höfle B, Pfeifer N. Correction of laser scanning intensity data: data and model-driven approaches. *ISPRS Journal of Photogrammetry and Remote Sensing* 2007; **62**(6):415–433.

17. Shan J, Toth CK. *Topographic Laser Ranging and Scanning: Principles and Processing*. CRC Press: London, UK, 2008.

18. Wagner W. Radiometric calibration of small-footprint full-waveform airborne laser scanner measurements: basic physical concepts. *ISPRS Journal of Photogrammetry and Remote Sensing* 2010; **65**(6):505–513.

19. Nicodemus FE, Richmond JC, Hsia JJ, Ginsberg IW, Limperis T. Geometrical considerations and nomenclature for reflectance: US Department of Commerce, National Bureau of Standards Washington, DC, USA, 1977.

20. Pfeifer N, Höfle B, Briese C, Rutzinger M, Haring A. Analysis of the backscattered energy in terrestrial laser scanning data. *The International Archives of the Photogrammetry, Remote Sensing and Spatial Information Sciences* 2008; **37**:1045–1052.

21. Mallet C, Bretar F. Full-waveform topographic lidar: state-of-the-art. *ISPRS Journal of Photogrammetry and Remote Sensing* 2009; **64**(1):1–16.

22. 3D scanner hardware. Geographica. http://www.geographica.hr/english/instruments/scanners/riegl. (Accessed on 19 May 2014)

23. Del Pozo S, Rodríguez-Gonzálvez P, Hernández-López D, Felipe-García B. Vicarious radiometric calibration of a multispectral camera on board an unmanned aerial system. *Remote Sensing* 2014; **6**(3):1918–1937.

24. Canon EOS 5D camera. Canon. http://www.canon.es/For_Home/Product_Finder/Cameras/Digital_SLR/EOS_5D/. (Accessed on 19 May 2014)

25. Liebowitz D, Zisserman A, editors. Metric rectification for perspective images of planes. Computer Vision and Pattern Recognition, 1998 Proceedings 1998 IEEE Computer Society Conference on; 1998: IEEE.

26. Hartigan JA, Wong MA. Algorithm AS 136: a *k*-means clustering algorithm. *Applied Statistics* 1979; **28**(1):100–108.

27. Bezdek JC. *Pattern Recognition with Fuzzy Objective Function Algorithms*. Kluwer Academic Publishers: Norwell, MA, USA, 1981.

28. Kannan S, Sathya A, Ramathilagam S, Pandiyarajan R. New robust fuzzy c-means based gaussian function in classifying brain tissue regions. In *Contemporary Computing*. Springer: Berlin, Germany, 2009; 158–169.

29. Metternicht G, Zinck J. Remote sensing of soil salinity: potentials and constraints. *Remote Sensing of Environment* 2003; **85**:1–20.

30. González-Jorge H, Puente I, Riveiro B, Martínez-Sánchez J, Arias P. Automatic segmentation of road overpasses and detection of mortar efflorescence using mobile lidar data. *Optics & Laser Technology* 2013; **54**:353–361.

31. González-Jorge H, Gonzalez-Aguilera D, Rodriguez-Gonzalvez P, Arias P. Monitoring biological crusts in civil engineering structures using intensity data from terrestrial laser scanners. *Construction and Building Materials* 2012; **31**:119–128.

4.3. Teoría de las imágenes multiespectrales y su aplicación al análisis de patologías presents en las construcciones

Este subcapítulo abarca el capítulo *Multispectral Imaging: Fundamentals, Principles and Methods to damage assessment in Constructions* (Imágenes multiespectrales: fundamentos, principios y métodos de evaluación de patologías en las construcciones) del libro *Geotechnologies for the Reverse Engineering of Structures and Infrastructures* publicado en Diciembre de 2015 como volumen de la serie *Structures & Infrastructures* en la editorial CRC Press/Balkema.

4.3.1. Resumen

Este capítulo de libro destaca la versatilidad y el potencial que tienen las imágenes multiespectrales para el diagnóstico y evaluación de patologías superficiales y particularizando para el caso de los materiales de construcción. A través de una revisión teórica de sus fundamentos, principios y métodos es posible adquirir las bases técnicas y de procesado para conseguir realizar una evaluación de patologías económica y eficiente a través del análisis de imágenes multiespectrales. Se dedica un apartado a las recomendaciones para elegir el sensor óptimo para cada caso de estudio concreto, las resoluciones requeridas, el coste, el tiempo, etc. Asimismo, se pone de manifiesto la importancia de convertir los datos crudos (en niveles digitales) de cada sensor a magnitudes físicas para mejorar los resultados de los procesos de clasificación de las imágenes. En este sentido, se dedica un apartado específico que proporciona asesoramiento tanto para realizar la calibración radiométrica como para el registro sensorial para una amplia gama de sensores. Para concluir, decir que los sistemas multiespectrales permiten la generación de productos híbridos de mapeo de patologías superficiales que resultan de gran utilidad para los expertos en materiales de construcción. Las imágenes multiespectrales se convierten de esta manera en una herramienta muy valiosa tanto para la detección como la cuantificación de patologías superficiales y para el mantenimiento y la toma de decisiones en este sentido.

Multispectral Imaging: fundamentals, principles and methods to damage assessment in constructions

S. Del Pozo, L. J. Sánchez-Aparicio, P. Rodríguez-Gonzálvez, J. Herrero-Pascual, A. Muñoz-Nieto, D. González-Aguilera
Dept. of Cartographic and Land Engineering, High School of Ávila, University of Salamanca, Ávila, Spain

D. Hernández-López
Regional Development Institute-IDR, University of Castilla-La Mancha, Albacete, Spain

ABSTRACT: Nowadays, the knowledge and maintenance of constructions has become a high-priority task for private and public institutions, largely due to the development, economy and cultural heritage that these constructions represent. The prevention, rehabilitation and restoration processes in constructions involve, among other task, the pathological analysis and assessment of building materials. To this end, it is important to perform qualitative analysis in some particular areas of the structure under consideration such as X-ray inspections or petrographic tests. This information is then extrapolated to the rest of the construction surface. Taking into account the above, and within a non-intrusive context, this chapter aims to provide readers the theoretical information necessary to carry out the diagnosis of pathologies in constructions by multispectral analysis.

1 INTRODUCTION

From early constructions to the sophisticated different architectural styles such as the Romanesque, Gothic or Neoclassical without overlooking the vernacular and the modern architecture, the choice of building materials has had a relevant role in constructions. The choice of the ideal material to be used (either for aesthetic reasons, workability, load-bearing capacity or availability) represents one of the most important decisions to be made. Besides, understanding how such material becomes degraded, its pathological state and evolution over time are unavoidable tasks in the conservation of buildings.

It is therefore crucial to establish a direct relationship between the pathological state of buildings and their conservation that should be addressed from a multidisciplinary approach that encompasses the use of different disciplines and types of sensors (Sánchez-Aparicio et al. 2014, Moropoulou et al. 2013).

In recent years, the use of multispectral data and different remote sensing techniques has drawn much attention focused on the classification of multispectral images. This product, defined as a set of data, in different regions of the electromagnetic spectrum, extracted from one or more sensors (active or passive) and assessed in the form of a 2D image offers decisive advantages and represents a new horizon for the analysis of building pathologies (Del Pozo et al. 2015, González-Jorge et al. 2012, Armesto-González et al. 2010).

In light of the foregoing, chapters VII and XIII aim to provide a complete overview (theoretical and practical) of the pathological study of constructions through the analysis of multispectral images. Under the same methodological framework, relevant aspects for the knowledge and conservation of buildings, as those listed below, have been taking into account:

Flexibility: understood as the applicability of the methodology presented, using data from both passive (conventional, multispectral or thermal cameras) and active sensors (laser scanning systems, microwave systems, geo-radar, tomography, etc.).

Versatility: directly related to the diversity of applicable sensors. Thanks to them and to the methodology proposed it is possible to differentiate a broad variety of construction materials and detect possible pathologies affecting them.

Safety: ensured because robotic platforms (terrestrial or aerial) are used allowing the implementation of this methodology in buildings whose structural integrity is in doubt and there is an increased safety risk to operators, and even in areas of difficult access (roofs, tops of towers, etc.).

Non-invasiveness: that is crucial in the maintenance and preservation of buildings. This property becomes more relevant in the case of historical buildings, where the main priority is to maintain the originality of their design.

Scalability: One of the most important properties of the technique discussed in this chapter lies in its ability to assess large-scale data, that can be defined as the analysis over large areas or even complete façades, unlike conventional methodologies for the study of pathologies confined to small localized areas.

After mentioning the most relevant characteristics of the methodology, among which highlight the abundance of geometric and radiometric data and the ability of analyzing large areas, it is logical to imagine that such methodology must occupy and important place in variety of engineering applications; more specifically preventive conservation and reverse engineering, as will be discussed below.

1.1   *Relation of the multispectral imaging with reverse engineering*

Traditional engineering uses methods and techniques for the planning, design manufacturing, testing and production of different objects where each process is carried out separately and the workflow is only in one direction.

By contrast, reverse engineering attempts to obtain information referring to a real object in order to analyze and improve it. This analysis encompasses the study of manufacturing defects, building materials, its operation and other aspects, such as its design and geometry, which must be taken into account for improving it.

In short, reverse engineering tries to re-document objects as computer-aided design (CAD) models, graphics or maps in order to improve and optimize the final article of the production chain. Sometimes it is even possible to manufacture a new one including the improvements in quality on it.

Reverse engineering applied to constructions has the main goal of collecting and compiling all the information referring to the characteristics of building materials, type of construction, geometry, structural behaviors, identification of possible pathologies and technical documents (work plans at different scales, sketches, etc.) to gain an exhaustive and comprehensive knowledge of the building for its reconstruction, rehabilitation, restoration or improvement of energy efficiency.

Degradation and alteration phenomena affecting building materials are the result of complex pathological processes. However, they all follow the same trend: (i) an origin; (ii) an evolution, and (iii) a final consequence. An exhaustive knowledge and quantification of the degradation process allows acquiring a new comprehension level of the construction. At this level it is possible to develop and apply preventive, restoration and rehabilitation measures.

The principles of the methodology discussed in this chapter are based on reverse engineering. First, a detection of pathologies (final consequence) is performed; then, ways of pathologies evolution are studied and finally, a rigorous evaluation of the causes with the support of the cartographic products generated is pinpointed. This is why the approach attempts to obtain the information referring to the real object, in this case the construction, in order to obtain a causal analysis. The essential requirement is thus to have experience in building materials and construction techniques, how different materials degrade and also knowledge on techniques capable to quantify such kind of construction damages (Fig. 1).
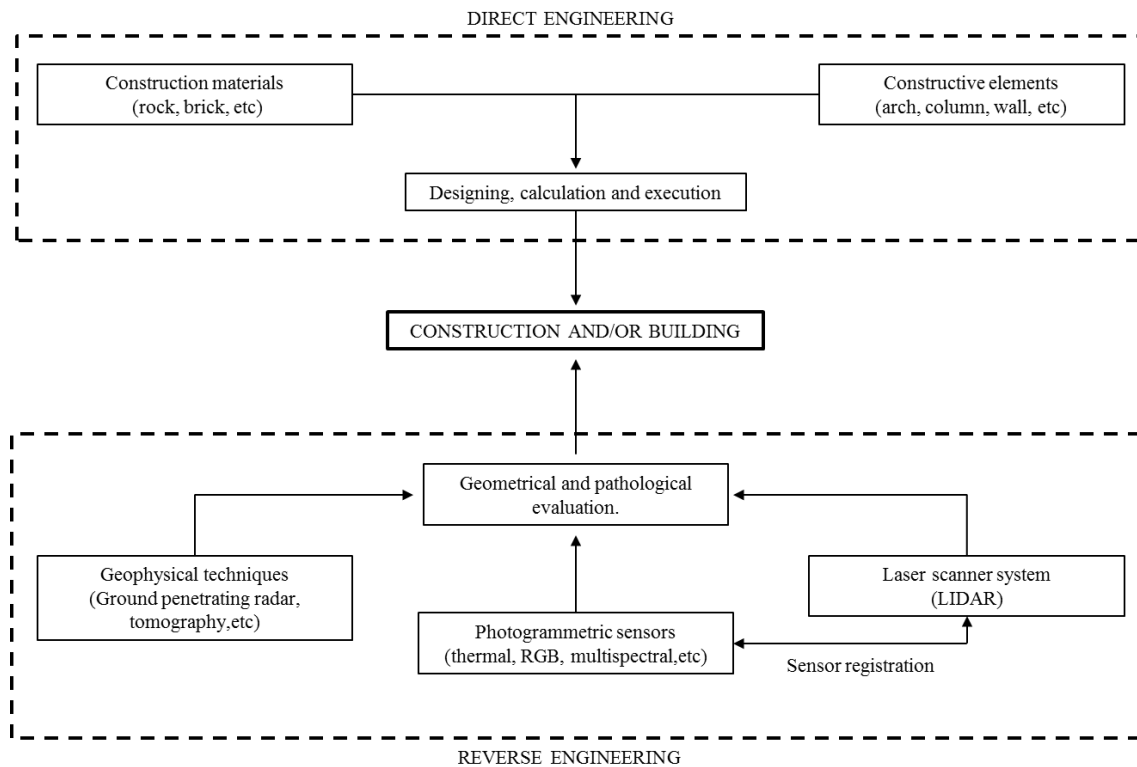
Figure 1. General workflow followed in the study of constructions through direct and reverse engineering.

Within the broad diversity of techniques that can be used for this purpose, remote sensing has become really important. This technology together with the use of algorithms and processing of computer data, allow data acquisition and interpretation in a rapid, reliable and precise way (Sánchez-Aparicio et al. 2015). Within this context, photogrammetry, remote sensing and multispectral image classification have become mainstream.

In light of the above, our aim in this chapter is to address, from a theoretical viewpoint, the most relevant aspects of the methodology presented, included in the following sections:

- Introduction. This section will afford an overall picture of the importance of pathological analysis in construction, together with the advantages provided by the multispectral analysis within the field.
- Theoretical background. This has a dual aim. On one hand, and in a clear and synthetic way, we shall describe and assess the most commonly materials used in construction, together with the pathological processes affecting them. On the other, we shall offer a series of basic data regarding remote sensing and multispectral imaging analysis, in the form of assumptions and principles.
- Acquisition of a multispectral dataset. This will provide a theoretical approach to: (i) types of sensors; (ii) technical specifications, and (iii) a short guide to good practices applicable to such sensors.
- Calibration and registration of multispectral data. This will address different aspects referring to the sensors used (radiometric calibration of photographic sensors, terrestrial laser scanners, and data registration from multiple sensors).
- Damage assessment. This section will show the final products (thematic, metric and cartographic information), together with the pathological analysis and evaluation revealing the potentiality of such products in the conservation of constructions.

2 THEORETICAL BACKGROUND

In this section a brief review of the physical fundamentals on which the data capture from electromagnetic energy is based is described.

2.1 *Principles of radiation*

In wave theory, electromagnetic radiation is described as a propagation phenomenon in which energy travels at constant speed (C) (the speed of light) and can be described by two parameters, the frequency(v) and the wavelength (λ), being:

$$C = v \cdot \lambda \tag{1}$$

In turn, Plank´s quantum theory explains how electromagnetic energy interacts with matter and that radiation is composed of discrete particles called photons or quanta, whose energy is described as:

$$Q = h \cdot v \tag{2}$$

Where h is the Plank's constant (6.626×10^{-34}J/second) and v is the frequency. Replacing v according to the Equation 1, we have:

$$Q = h \cdot C / \lambda \tag{3}$$

This expression indicates that the energy of a quanta becomes smaller as wavelength increases and is, therefore, more difficult to be detected.

2.2 *Energy interactions with materials*

The electromagnetic energy detected by a sensor crosses the atmosphere before being recorded. Since the atmosphere is a body with variable composition and characteristics, during its passage it may suffer many alterations. This fact is of great importance in the case of multispectral satellite sensors because the solar rays have to cross the whole of the atmosphere. Nevertheless, in the present context since the distance between the sensors used and the objects are very small (a maximum of 100-200 m), the atmospheric effect can be considered negligible with respect to the levels of precision we are working at.

It is therefore appropriate to focus on the interaction processes that happen when electromagnetic energy impinges on the different surfaces and materials. All this can be explained via the principle of the conservation of energy, according to which the incident energy is reflected, absorbed or transmitted by the different covers and depends on the wavelength considered (Equation 4).

$$E_i(\lambda) = E_r(\lambda) + E_a(\lambda) + E_t(\lambda) \tag{4}$$

where $E_i(\lambda)$ is the incident energy, $E_r(\lambda)$ is the reflected energy, $E_a(\lambda)$ is the absorbed energy, and $E_t(\lambda)$ is the transmitted energy.

The share of energy reflected, absorbed and transmitted by the same material depends not only on its composition and current condition but also on the wavelength at which it is observed. Thus, by using multispectral sensors, it is possible to distinguish different states, characteristics and properties of the same material at the same time.

From all the types of energy described in Equation 4, multispectral sensors are specialized in observing the proportion of energy reflected. In order to study it, it is important to bear in mind the way objects reflect, that is the geometry of the reflection. Essentially, it depends on the roughness of the object surface. Thus, it is possible to distinguish two types of ideal reflectors (Fig. 2a): the specular type, where the angle of incident radiation is the same as the angle of reflect radiation; and the diffuse or Lambertian types (on rough surfaces), in which the reflection is uniform in all directions. However, in practice, these cases are not seen and the reflection is mixed between these two ideal cases.
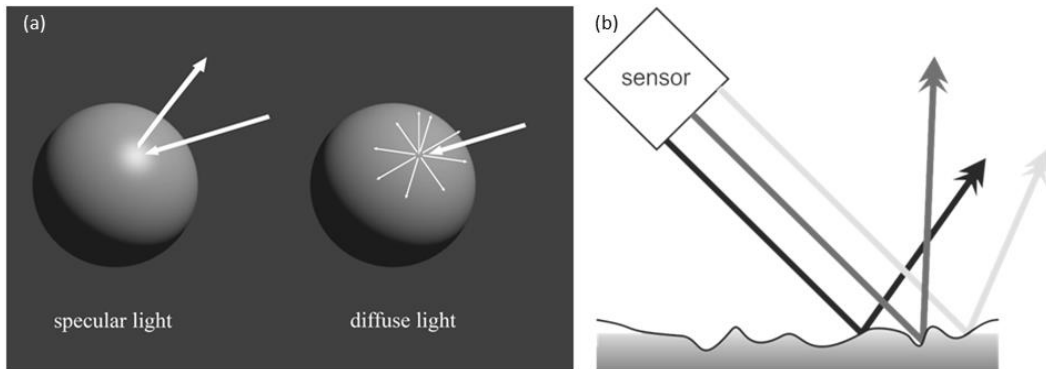
Figure 2. (a) Types of reflectors; (b) Diffuse reflection.

Regarding construction materials, the specular reflection may occur on surfaces such as glass, steel or aluminum. But in most cases, the incident wavelength is much smaller than the variations in height of the surface to be studied, so that the reflection is usually diffuse (Fig. 2b).

Diffuse reflection contains information about the color, being this property the most interesting one to be observed in view of the information it provides. The reflectance (ρ) of a material is defined as the portion of reflected energy compared to the incident energy (Equation 5).

$$\rho = \frac{E_r(\lambda)}{E_i(\lambda)} \tag{5}$$

where ρ is the reflectance, $E_r(\lambda)$ is the reflected energy and $E_i(\lambda)$ is the incident energy.

By analyzing the reflectance graphics for different wavelengths it is possible to construct the so-called spectral reflectance curves or spectral signatures.

2.3 Spectral Signatures

The wavelength and its location on the electromagnetic spectrum are the parameters that are usually used to classify electromagnetic waves. In the electromagnetic spectrum it is possible to distinguish different regions: the ultraviolet, the visible (wavelengths between blue and red; from 400 to 700 nm), the infrared (near infrared: 700-1,300 nm, middle infrared: 1,300-3,000 nm and thermal: 3,000-14,000 nm), microwaves (from 1 mm to 1 m) etc.
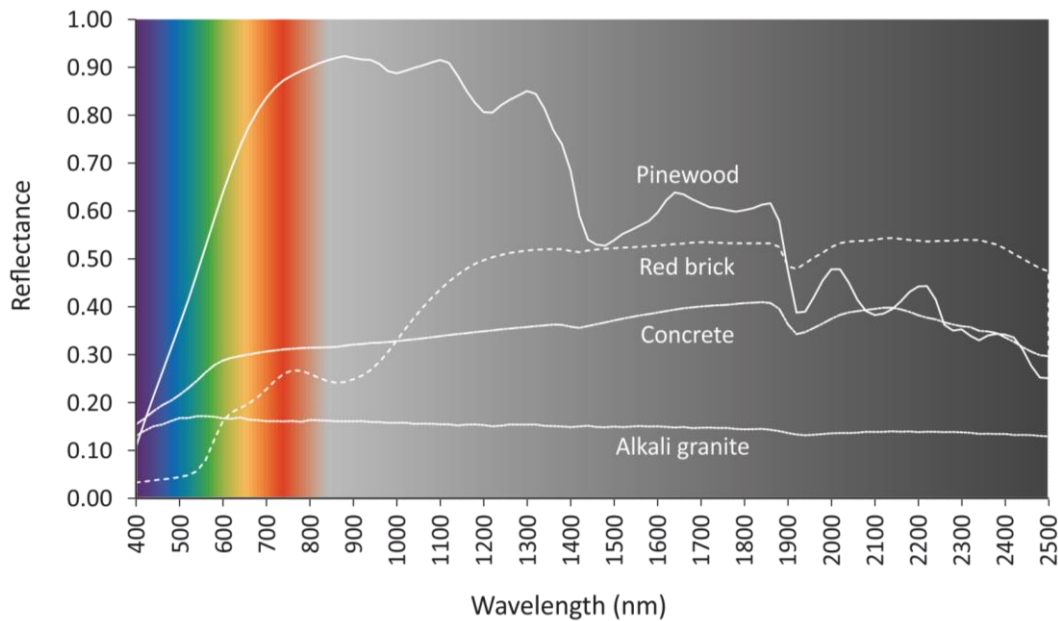
Figure 3. Spectral signatures of the most common construction materials.

Acquiring data from constructions and façades in a remote way by multispectral systems and sensors is possible thanks to the interaction between the electromagnetic energy and the different molecular components of materials. Each material has its specific spectral behavior, which can be obtained at the laboratory under controlled conditions. That is, each material has its specific way of reflecting energy at the different wavelengths and it is perceived by observing its spectral signature (Fig. 3).

However, far from being a unique and homogeneous behavior varies substantially as a function of the physico-chemical properties (temperature, moisture, degradation, decomposition). These characteristics are recorded in the data acquisition, and vary depending on some environmental factors (illumination, reflections, etc.) These alterations give rise to difficulties when attempting to identify, characterize and classify materials, but at the same time are the basis for acquiring valuable information about the alteration degree of the materials, the presence of chemical or biological pathologies as well as structural damages.

At this point, it could be asked how many points of the electromagnetic spectrum would be necessary to differentiate a given material or certain characteristics of that material. Without considering hyperspectral sensors, it may be sufficient to develop strategies based on the choice of just a few wavelengths, appropriately chosen, which could be enough to perform the identification and discrimination of a material. When the spectral signatures are significant along the different regions of the spectrum, there are no problems for the differentiation of materials to be classified. However, there are some materials with similar spectral responses and may be necessary to observe them at very close wavelengths. Accordingly, if the aim is to identify a single material or characteristic the choice of few suitable wavelengths will suffice. The greater variety of materials to be identified, the greater number of wavelengths necessary.

2.1 *Materials characterization: classification and common pathologies*

Throughout history, the quantity of different materials used for construction purposes has been increased. Accordingly, it is crucial to understand the nature and limitations of such materials, thus determining their applicability and behavior in a construction. Despite this, for the purpose of this chapter it is sufficient to establish a series of basic concepts, which enable, in a generalized way, the discrimination and knowledge of the broad variety of materials that are currently used in constructions.

Leaving aside the pathological conditions of the materials, the classification of materials can include several criteria, from a classification based on the construction functionality (resistant, agglomerating and auxiliary materials), through a classification based on their emplacement in

the construction (foundations, structures, envelopes, finishes and decoration) to a classification based on their nature (stone, agglomerates, organic and metallic materials, among others). Within this range of classifications, the most suitable one for our purposes would be the latter one (Fig. 4).
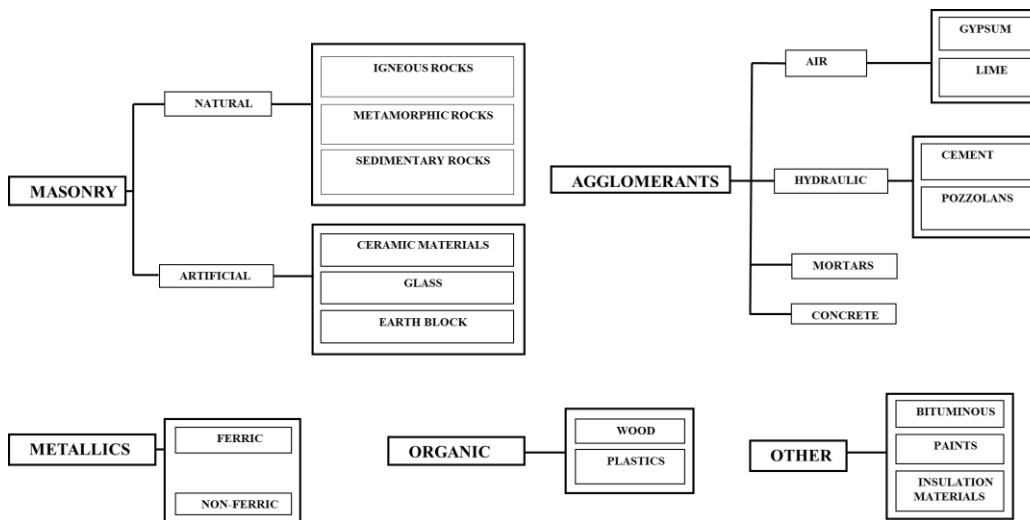
Figure 4. General classification of materials (attending to their nature) commonly used in construction.

Traditionally, humans have used available and durable materials that were closest to the construction. These materials may have changed due to possible degradation processes. Even, materials of the most modern constructions and buildings may be eventually deteriorated and become degraded due to time or other reasons (e.g., lack of maintenance). These alterations may depend on:

- The construction element (wood, granite, limestone, slate, adobe, brick, steel, concrete, etc.) and characteristics as composition, structure and texture.
- The constructive element (foundations, walls, arches, vaults, concrete slabs, pillars, etc.).
- The environmental conditions (sharp changes in temperature, rain, snow) which elicit processes of weathering and erosion.
- The location of the construction (orientation and geographic situation).
- Environmental pollution (e.g. constructions close to roads with a high traffic density or industrial parks).
- On human activity (paint on walls, acts of vandalism, armed conflicts).
- Natural disasters (earthquakes, fires, etc.).

To offer an exhaustive definition of the properties and pathologies that such materials might display is not the aim of this chapter. Accordingly, below we shall have a brief and fairly general look of the properties of the materials and the main causes of the pathologies affecting constructions.

In order to determine which type of material is ideal for a given construction it is necessary to know its properties, for that reason following properties of solids materials are studied:

- Mechanical properties: Deformation produced by the load of the structure. This property establishes the material strength and its elastic modulus.
- Electrical properties: Electrical conductivity and dielectric constant.
- Thermal properties: Thermal conductivity and heat capacity.
- Magnetic properties: Response of the material to a magnetic field.
- Optical properties: Refractive and reflectivity indexes and the response to the electromagnetic radiation.
- Chemical properties: Chemical reactivity of the material.

The origin or cause of the pathological process can be divided into two well-differentiated groups:

- Indirect causes: derived from construction problems due to poor design, inadequate building practices, the use of defective materials, and from lack of maintenance. These are the first causes that must be prevented.
- Direct causes: refer to all the damage arising from structural, atmospheric, chemical, physical, reasons, among others.

Below we show schematically the main direct causes:

- Structural causes: movement of structures, separation of wall coverings and materials etc. In this context, the following mechanical damages must be studied:
  - Deformations: strains, deflections, impacts and vibrations.
  - Cracks: longitudinal openings affecting the thickness of the construction element owing to excess load or hygrothermal expansion and shrinkage.
  - Fissures: like cracks, the affect the surface of the construction element as the results of a discontinuity, owing to a join, to the lack of adherence or to deformations and movements of expansion and shrinkage.
  - Material detachments: owing to the lack of adherence between the finishing material and its support. The main cause is due to other previous damages such as those caused by humidity, cracks or deformations.
  - Mechanical erosion: caused by accidental knocks or grazes that produce the loss of surface material. This erosion usually occurs on the plinths and lower parts of façades.
- Degradation of materials due to:
  - Internal factors (composition, structure, and texture). Knowledge of the internal properties of each material used allows choosing the most suitable one. A wrong selection of a material may lead to its rapid degradation.
  - External factors as environmental conditions (frosts, rains, etc.), its use and its maintenance.

The following external factors must be taken into account:

- Physical damage due to environmental phenomena. Highlighting :
  - Humidity: an excess of water, greater than admitted by the construction material, causes physical variations of the materials (humidity during construction, capillarity, leaks, condensation and other accidental factors).
  - Erosion: the loss of surface or modification of materials due to the action of atmospheric agents that produce weathering.
  - Pollution: this leads to dirtiness on façades owing to the deposition of suspended particles in the air. If the particles are simply deposited, the result of dirtiness is due to deposition, but if they enter the pores of the surface the dirtiness is caused by differential washing that cause characteristic marks on surfaces.
- Chemical damages. Caused by the appearance of salts or exposure to acid or alkaline environments, which react with the construction material and lead to its decomposition and degradation. The following factors are the most important:
  - Efflorescence. The soluble salts contained in the construction material are dissolved in the water of humid parts showing as a white chalky deposit on the surface. The crypto-efflorescence is also very important and it is refers to crystallized salts that are formed inside the material, leading to hollows and later detachment of the material.
  - Oxidation and corrosion. These processes occur on metals such as iron and steel due to electrochemical reactions between the metal and the external elements of its surroundings. This may lead to a progressive loss of materials from the surface of the construction.
  - Organisms. This refers to living beings, either animal or vegetal, which can secrete aggressive substance that can degrade and alter the construction materials (moulds and fungi) and also can penetrate the surface (insects, roots, etc.) causing physical damage.
  - Erosion due to chemical factors can cause molecular transformations in the materials by reacting with other elements.

It is important to note that after gathering an exhaustive data collection referring to the construction, it is necessary to perform a rigorous data acquisition to study the degradation level of

the materials. In the data acquisition, and depending on the specific pathology, greater or lesser importance should be given to geometric aspects (the assessment of deformation, mechanical erosion, etc.) and to qualitative (X-ray, the use of reagent, etc.) and quantitative analysis (multi-spectral image studies).

If it becomes necessary to get an in-depth knowledge of the construction materials, their properties and associated pathologies, readers are invited to consult (Watt 1999), as well as the technical legislation for construction associated to each country.

3 ACQUIRING A MULTISPECTRAL DATASET

The concept of multispectral image is traditionally associated with the concept of data captured by a single remote sensor (multispectral cameras) capable of recording information at various wavelengths at the same time (Campbell 2002). This section aims to provide a more comprehensive view of this concept, opening the possibility of acquiring multispectral datasets by the combination of data coming from different types of sensor, whether passive (visible, infrared, and thermal cameras) or active (laser scanners).

A multispectral dataset is essentially made up of a matrix of numerical values called digital levels that come from the analogic-digital transformation of the electromagnetic energy reflected by the surface of the object observed (Jones et al. 2010). The value of the digital level corresponding to a pixel is proportional to the intensity of the radiance ($W \cdot m^{-2} \cdot sr^{-1} \cdot nm^{-1}$) reflected by the object. The ability of the sensor to discriminate among levels of radiance, and hence offer a greater or smaller range of digital levels, will depend on the radiometric resolution. If in the acquisition of a multispectral dataset several mono-spectral sensors are used with the aim of capturing several bands or channels of the electromagnetic spectrum, the process of the formation of the digital image is repeated for each of the sensors used, recording information at the specific wavelength of each of them. However, in the case of using multispectral systems, the formation of the multispectral dataset is performed simultaneously owing to the synchronized use of a set of cameras integrated into a single sensor. Each of these cameras can be equipped with an optic filter designed to absorb radiation only within a specific wavelength range (Lillesand et al. 2004) or with a dedicated sensor with an integrated filter. Whichever method is used, the final result is the generation of a three-dimensional matrix (Fig. 5) (NxMxB) in which the value of the digital level of each pixel ($P_{n,m}$) will be located in a row (N), a column (M) and a band (B), from where the term of multispectral image is coined.
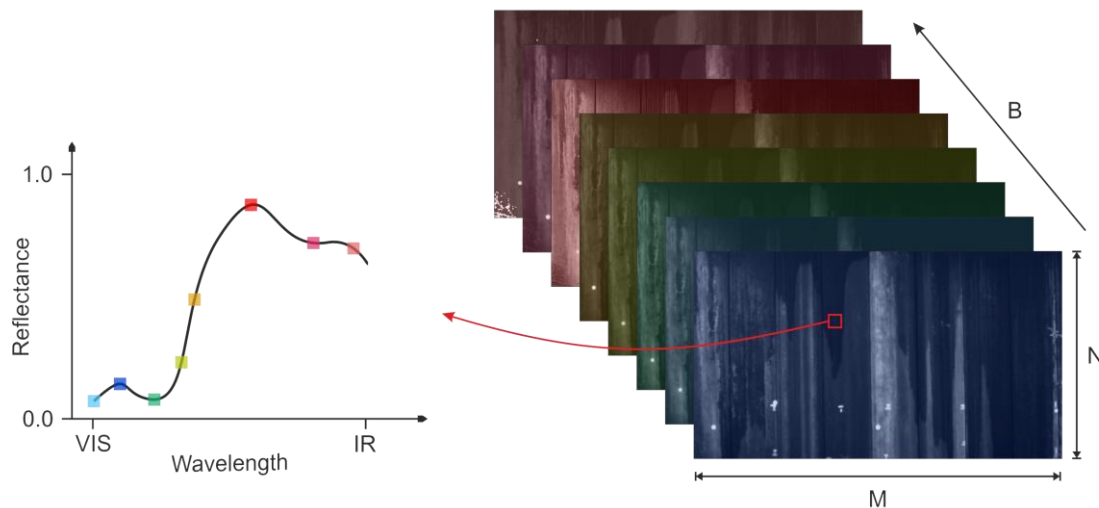
Figure 5. Multispectral image formed by eight different spectral bands and a spectral signature obtained from the reflectance of a pixel for each band.

In multispectral datasets, the information recorded by each sensor can be exploited together adding the advantages that various sensors can bring to the limited registration of a single one. In order to achieve this spectral hybridization, a number of corrections and modifications must be

undertaken to achieve uniformity in the resolution of the data and a rigorous registration process of the sensors involved (see Section 4). In short, the aim is to be able to simultaneously use the radiometric data collected by each sensor, thus broadening the spectral resolution of the final multispectral image. The ultimate objective is to analyze and assess the status and progress of degradation in constructions and detect possible pathologies by using different sensors strategically.

3.1   *Choosing the most appropriate sensor*

The choice of acquisition sensors for each individual study case will depend on several factors, among them: (i) the aim pursued (detection of biological elements damp patches, structural damage, etc.), which will dictate the range of wavelengths to be used; (ii) the working scale, which will govern the level of geometric resolution required for the sensor; (iii) the type of predominant material or materials in the object, and (iv) the temporal frequency necessary to appreciate unequivocally the changes in the object (Sabins 2007). Therefore, if the aim is focused on multispectral image generation from data captured by two or more different sensors, the first step is to ensure a perfect homogenization of the data resolutions after which a proper registration is made. This process will be addressed in detail in Section 4: Multispectral dataset calibration and registration.

Sensor resolution.

To understand the whole concept of the resolution of a sensor, four concepts need to be considered:
-   *Radiometric resolution*: Number of digital levels in which the intensity of the signal (radiance) is recorded. Since radiance is stored as a number of binary bits, the greater the number of storage bits of the sensor, the greater the radiometric resolution. For temperature sensors, the radiometric resolution is often converted to the equivalent thermal resolution. The most commonly used sensors for spectral studies of construction materials have radiometric resolutions ranging between 8 and 12 bits, (256 to 4096 different digital levels).
-   *Spatial resolution*: Size of the ground element represented by an individual pixel. This is usually determined by the optical system of the sensor used to capture the data and by the distance between the sensor and the object (scale). The ground sample distance (GSD) is equivalent pixel size on the ground and is defined in Equation 6.

$$GSD = \frac{d \cdot S}{f} \tag{6}$$

where d being the distance to the object; S is pixel size and f is the camera focal length.
If the sensor-object distance (d) is reduced very much, it may be possible to achieve sub-millimeter resolutions by the use of devices with large focal lengths and sensors with a very small pixel size.
-   *Spectral resolution*: The ability of a sensor to define wavelength intervals and hence to discriminate between different component wavelengths in the scene; it is determined by the number and width of the individual spectral bands recorded.
-   *Temporal resolution*: The time between successive data captures. It makes sense in satellite imagery and ground-based monitoring case studies to analyze the state of the object under study along time. It is vital for predicting maintenance strategies in order to prevent the degradation of building materials and to prioritize different stages of possible rehabilitations.

Below, a variety of sensors ranging from the mono-spectral to multispectral types are discussed in detail. As already mentioned, the data from all of them can be combined to form a multispectral dataset with more valuable information.

Sensing instruments

The most common classification of sensors categorize them in two main groups. Namely passive and active sensors, depending on whether they require or not an external energy source to

recover information (Tsang et al. 1985). All can be fixed or loaded onto a large variety of plat-forms for the acquisition of data around the object of interest (from hand-held platforms at ground level to unmanned aerial systems, aircraft and satellites). In practice, and particularly in the case of constructions, the most widely used platforms are those that allow the sensors to be fixed and make a controlled capture to be made at ground level, and in some cases from above the ground, by the use of drones several meters above the structure. The platform chosen deter-mines the position of the sensor in the data collection and the theoretical spatial resolution as long as a distance to the object is fixed.

- *Passive sensors.* Passive sensors need an external energy source. The Sun acts as a natu-ral source of radiation and the energy reflected by the different construction materials is captured passively. The energy that is naturally emitted in the specific case of thermal infrared can be detected in the daytime or night, as long as the amount of energy is large enough to be recorded. Since light is crucial for passive optical sensors, it must be en-sured that the light will be as uniform as possible during data acquisition. These systems are made up of photo-detectors or thermal detectors sensitive to the electromagnetic ra-diation at wavelengths ranging from the visible spectrum to the infrared and their corre-sponding filters. There are two possible configurations for the case of photo-detectors. Those called CCD (Charge-Coupled Device) and CMOS (Complementary Metal-Oxide Semiconductor) (Magnan 2003). Both comprise metal-oxide semiconductors distributed in matrix form and they accumulate an electric charge for each pixel proportional to the intensity of the incident radiation but differ in method of reading the electric charges; different advantages and drawbacks are inherent to both. Thermal detectors use a differ-ent kind of technology based on the absorption of the heat energy emitted by the object being studied. Except for thermographic cameras, the use of filters adds the possibility of selecting the bands of the spectrum at which the best characterization of the object to be studied can be achieved. Below are images of the passive sensors most widely used for the spectral analysis of construction materials (Fig. 6a).

Figure 6. Examples of sensors used in the inspection of constructions: (a) active sensors, (b) passive sen-sors.

- *Consumer-grade/reflex digital cameras* (Visible region 400-700 nm)
  The lens is the element of cameras that is used to focus the light reflected onto the photoelectric detector. For the inspection of constructions, high geometric and radiometric resolutions and the use of high-quality lenses is required. The main advantages of consumer-grade digital cameras are their convenience, portability (weights of 150 g or even less) and low cost. Unfortunately, however, these sensors come with a number of features which have adverse effects on remote sensing applications. The final product of these sensors is color images. To generate these images, an optical filter is coupled to the photoelectric detector (normally CCD) in order to obtain the three primary colors (red, green and blue), which combined in different proportions cause the sensation of color. This filter is known as a Color Filter Array (CFA) mask, or Bayer filter mosaic, and in it four original pixels from the detector are required to generate each color pixel, with the consequent loss of spatial resolutions (Lu et al. 2003).
- *Multispectral cameras* (From visible to short-wave infrared – SWIR – region 400-3,000 nm)
  Multispectral sensors are the only passive systems able to record information simultaneously in a few bands of the spectrum. The main problem with these systems is how to achieve multispectrality and the correct synchronization of all the elements involved. There are several configurations that can be used to do this. On the one hand, the integration of several lenses (photo-detector plus optical filter) in a single device (such as the case illustrated in Fig. 6), where each lens records information for the spectral band permitted by its filter. On the other, there are the cameras that achieve multispectrality using a single photo-detector and a ring of filters that, by means of small, rapid rotation, fixes the required input filter. The advantage of these over the former is the absence of eccentricity between the different captures; in this case the multispectral image is conformed almost immediately with no need for parallax correction (distance between the lenses). In this case, the geometric corrections and the correction of systematic errors (Del Pozo et al., 2014) are made only for the existing lens, such that time can be saved. By contrast, they have the important drawback of not being able to capture the multispectral dataset at the same moment of time.
- *Thermal cameras* (Thermal infrared region 8,000-15,000 nm)
  Any object with a temperature higher than absolute zero (-273 ℃ or 0 ℃K) is able to emit infrared energy. The cameras included in this group allow the temperature of the object studied to be obtained at a given distance, without the need to establish physical contact with its surface. Thanks to the thermal detectors incorporated, they capture the infrared radiation belonging to the radiation emitted by different surfaces and convert this into electrical energy. This electrical energy is translated into a digital value, finally providing the so-called thermographs or thermal images, from which is it is possible to derive the temperature for each pixel.

- *Active sensors.* These provide their own source of radiation for illumination. They emit radiation, which is directed toward the surface to be investigated. The radiation reflected from that target is detected and measured by these sensors. One of the most widely used sensors for the radiometric and spectral study of materials is the terrestrial laser scanner.
  - *3D laser scanners*
    Three-dimensional laser scanners are of standard use in the geometric documentation of constructions and buildings since they allow real objects to be reconstructed in three dimensions with high spatial resolution in a short period of time. Use of this type of sensor for the creation of multispectral dataset needs data processing to perform the required transformations and obtain 2D images from 3D information.
    These are active systems, generally narrow-band mono-spectral that emit a series of laser pulses in all spatial directions thanks to deflector mirrors, after which the returning beam is captured, obtaining 3D information of the element studied. In some cases they have cameras, such that as well as the above-mentioned intensity it

is possible to extract information about the visible range of the object. These sensors do not need to be in contact with the structure, which is a key factor in the documentation of constructions and buildings where techniques that might degrade the construction material have been ruled out. One of the greatest advantages of this type of sensor is the possibility of combining the geometric and radiometric information provided so that the pathologies detected in the construction materials can be characterized.

The physical principles on which the system of distance measurement is based (optical triangulation, time of flight and phase shift govern the range and precision of the laser. There are different configurations and models, and we are now witnessing the evolution towards the design of increasingly rapid, light and precise sensors. This variety of configurations allows different possibilities and functionalities that are useful for many user needs. Figure 6b shows some of the laser scanners most widely used for the documentation and characterization of the pathologies found in construction materials.

3.2 *Advise and best practices for multispectral data acquisition*

Since there is a large variety of sensors that can be used to characterize possible pathologies in constructions, the aim of this section is to offer a guide to good practices for the data acquisition and ease data processing required to conform the final multispectral dataset. In chapter XIII, where several study cases are discussed, conclusions may be drawn about the adequacy of each of the sensors and their suitability for each situation and pathology. In the long run, the issue is to perform a good planning of the data acquisition step in which the appropriate sensors and criteria are taken into account

Below there is a list of the most important criteria to bear in mind in the general capture of data (the use of both passive and active sensors) and for the particular use of optical passive and thermal passive sensors.

Active and passive sensors:
- Distance to the object vs. spatial resolution. In this matter, it is necessary to bear in mind that correct focusing of the object is crucial if we are to obtain clear, high-quality results. Accordingly, it is necessary to take into account the field of view (FOV) of the sensor. This will determine the total number of settings and hence the total duration of final data acquisition.
- Surface uniformity. The more uniform the surface, the better the results obtained since the radiation will be reflected in a diffuse and uniform way so fewer shadows will be generated.
- Overlapping. With a view to obtaining a large amount of information, ease the matching of geometries and ensuring the validity of the dataset, it is appropriate to establish certain overlapping zones between captures, whose amount may vary depending on the particular study case.
- Number of settings. The greater the number of settings, the longer the time spent on acquisition, the greater the amount of information and the greater the error propagation. The general strategy consists of optimizing the number of stop settings, maintaining the criterion of overlapping and solving the problem of masking and interferences that may exist (object interposed, static and in motion).

Passive optical sensors:
- Homogeneous illumination. Care must be taken to prevent the surface studied from having any kind of projected shadow, deriving either from the construction itself or from some element outside it. Accordingly, it is recommended that measurements be taken on cloudy days since these are when solar radiation is most uniform and diffuse.
- Time of data acquisition. Care should be taken to avoid the central hours of the day when the variability in the radiation between illuminated and non-illuminated zones is most pronounced. Also, maximum efforts should be made to avoid situations when zone of shadow, hidden zones and zones with reflections arise. The ideal times are therefore at dawn and just before dusk.

- Position with respect to the Sun. The reflection from a surface is a function of the angle of view and depends on the proportion of specular and diffuse reflectance. The most appropriate position, in cases where there is no homogeneous light, is the one in which the Sun is immediately behind the device, so that the surface is completely illuminated. It may be useful to note down the time and date of image capture in case it were necessary to make any corrections later.

Passive thermal sensors:
- Thermal equilibrium. A specific thermographic data acquisition protocol is performed to avoid surface heating by direct radiation from the Sun. In particular, images are acquired before sunrise and after sunset. Thermographies are taken with the same focus the camera is calibrated for, from an orthogonal position with respect to the façade considered, maintaining a constant distance according to the resolution required and guaranteeing an overlap between adjacent thermographies.

4   MULTISPECTRAL DATASET CALIBRATION AND REGISTRATION

As a function of its composition and state each object reflects and emits radiation differently, fulfilling the laws of physics (Section 2). Thus, the curve that describes the proportion of radiation reflected as a function of the wavelength is known as the spectral signature (Fig. 3). Regarding emission, this is a function of the temperature of the object and will take place in the infrared for temperatures close to the Earth's surface (Orlande et al. 2011). The challenge of remote sensing is no more than using a camera/sensor that can digitally store the energy coming from the object observed, radiance either reflected or emitted. By this way it is possible to use the images generated to classify the type of object, extract its characteristics and even assess its possible states, such as for example the existence of pathologies. To solve the problem at hand, it is necessary to follow a series of steps that invert the process of transformation undergone by the radiation since it is emitted or reflected from the object until it is stored digitally.

The first alteration to the radiation is due to the propagation medium between the object and the sensor, which essentially consists of scattering and addition of radiation emitted by the atmosphere itself. As commented in Section 2, its correction can be considered negligible for captures taken at ground level, where the object-sensor distance is very small. Nevertheless, there are mathematical models for calculating this type of correction, such as the 6S model (Vermote et al. 1997).

From the time when the radiation reaches the sensor until the image stored in binary format is generated a series of processes occurs, outlined in the following figure (Fig. 7).
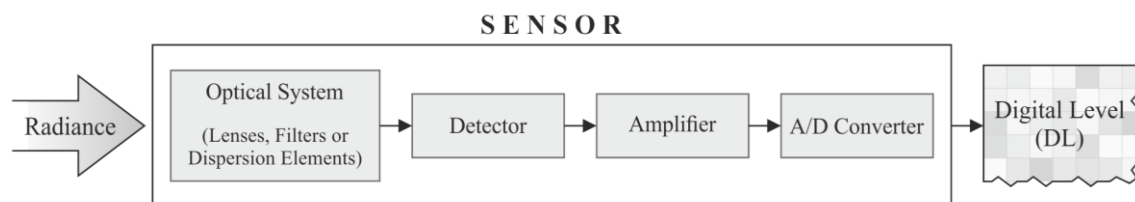
Figure 7. Main components of a sensor.

When the radiation finally reaches the surface of the detector, the signal generated will depend on the amount of energy of each wavelength and the response of the detector. This process involves the response curve of the sensor, which depends on its chemical composition and will vary for each wavelength, as illustrated below (Fig. 8).
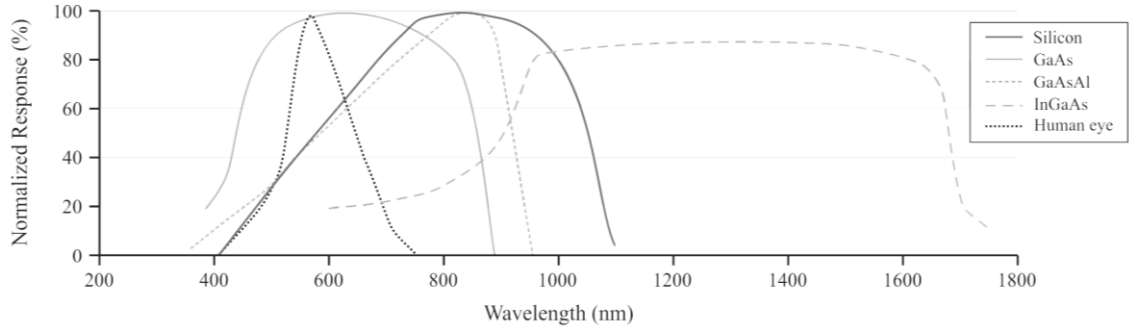
Figure 8. Spectral response of the human eye in comparison with different detectors: silicon (visible and infrared cameras), GaAs-GaAsAl (Near infrared cameras) and InGaAs (SWIR cameras).

Then, the signal received, expressed as an electrical response (Fig. 9), is amplified and converted into a digital level, applying two coefficients, called gain and offset, and a quantification to convert it into a whole number (as a function of the radiometric resolution of the sensor, as commented in Section 3). In some cameras, the choice of an ISO sensitivity corresponds to the alteration in gain, its increase allowing the acquisition of images from poorly lit scenes, with the drawback of the consequent increase in noise that is translated into a loss of definition.
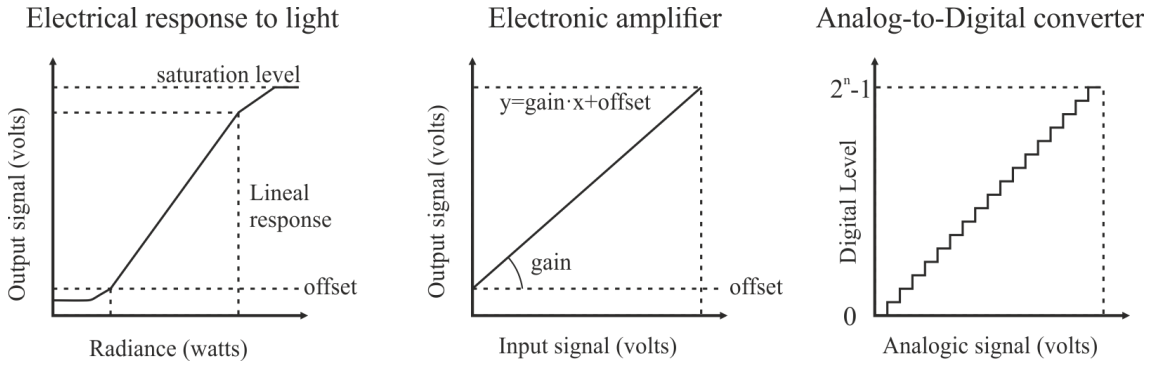
Figure 9. Different stages involved in the conversion of light radiance to digital levels: electrical response (left), amplification (centre) and analog-to-digital conversion (right).

New cameras/sensors working in regions beyond the visible spectrum have appeared on the market for short-range applications, including multispectral, hyperspectral and thermal sensors. However, currently it is necessary to use different cameras/sensors to complete the perception of objects in the different regions of the spectrum that the final user one is interested in. This need is imposed by the trade-off between the different resolution components of sensors (Section 3.1). The use of several sensors involves solving two problems: the radiometric calibration, which will allow the physical variables to be estimated for each of the bands, and the geometric fusion or registration of sensors that will allow the correct three-dimensional position to be attributed to the physical information obtained. Below we devote two subsections to addressing both issues.

4.1 *Radiometric calibration*

In remote sensing, the relationship between the digital level (DL) and the reflectivity of the object observed (ρ_k) is expressed, in a first approximation, as Equation 7 shows:

$$\rho_k = \frac{\pi \cdot L_k}{E_\lambda} = \frac{\pi(gain \cdot DL + offset)}{E_\lambda} \tag{7}$$

where L represents radiance, E represents the irradiance of the scene, gain and offset are the radiometric calibration coefficients, considering the following as a hypothesis: a Lambertian be-

havior (π) of the surface of the observed object, and a propagation unaffected by alterations from the atmosphere (Section 2).

The radiometric calibration is simply the process that allows knowing the gain and offsetting coefficients necessary for later application in order to obtain physical magnitudes, in terms of radiance, reflectivity, temperature, etc. They will be estimated from the digital levels extracted from the image in the correct position for each region of the surface of the observed object, which will also involve removing possible geometric aberrations by a photogrammetric modeling process.

In short, radiometric calibration is based on inverting Equation 7, in terms of reflectivity in this case, posing a set of equations where the unknowns are precisely the gain and offset calibration coefficients (Moran et al., 2001). As an example, in many case of satellite imagery, these coefficients are provided in a metadata file, and have been solved previously in a process of laboratory calibration prior to placing the sensor in orbit, but which in certain cases are corrected on the basis of a field calibration process. In the laboratory calibration there is total control over the energy source and an special device known as integrating sphere is used in order to approximate quite closely Lambertian behavior. In field calibration, or vicarious calibration, reflectivity values are obtained for a set of areas observed in the image using a spectroradiometer. Also, by measuring the radiance for an artificial surface of known and calibrated reflectance and Lambertian behavior at the same moment it is possible to obtained the reflectivity in the band in question. In this process, on one hand we measure pseudo-invariant artificial surfaces such as colored and gray scale tarps to solve the calibration model and on the other we measure artificial or natural surfaces to validate it.

4.2 *Registration based on multiple sensors*

If the aim is to consider the three-dimensional geometry of the surface of an object onto which the radiometric information of the different bands of the available images will be projected as texture, the solution will lie in solving the General Method of Aerial Photogrammetry (Kraus et al. 1993). But this methodology will have the added problem of the complex geometries present in terrestrial scenarios. This methodology can be split into two large steps: (i) determination of the position (spatial and angular) of the sensors, and (ii) reconstruction of the 3D geometry of the object. Having determined the geometry and having resolved the positions of the sensors, we shall be able to extract the radiometric values associated with the geometry of the object in each of the spectral bands.

In order to relate the values of the image pixels of the images from the different sensors to the corresponding points of the object observed, it is necessary to solve the internal parameters and external position of the sensor, which includes the processes of internal and external orientation respectively. The internal orientation solves the problems of the geometry in the sensor: the optics and sensor plane, including models to obtain the focal length, the principal point and the geometric distortion. The external orientation refers to the capture position and the orientation of the viewing axis.

The internal orientation can be solved by the process of geometric calibration of the sensors (Luhmann et al. 2013), which can be done at the laboratory before the field campaigns. Alternatively, the unknowns of internal parameters can be integrated in the adjustment of the external orientation described below, in the method known as self-calibration.

The determination of the images external orientations is a classic problem of photogrammetry, known as photogrammetric spatial resection, and this can be solved through the formulation of a mathematical model (collinearity condition). This model involves points of the scene of known position (Ground control points - GCPs), which are measured manually in the images, and tie-points of unknown position on the scene , measured in the images automatically by applying algorithms belonging to computer vision, such as SIFT (Scale-Invariant Feature Transform) (Lowe, 1999) or SURF (Speeded Up Robust Features) (Bay et al. 2006). However in certain cases tie-point detection can be completed by manual measurement. Solving this process requires having sufficient overlap between the images. Although this method provides valid results in the case of images in the visible spectrum with sufficient overlap and image quality, in

the case of other regions of the spectrum it is a problem that currently remains to be solved (known as multimodal matching). This is the case above all in the thermal infrared, owing to causes such as insufficient overlap between images, radiometric variations due to changes in perspective, low geometric resolution, poor definition in the images, a paucity of radiometric variation between certain bands, etc.

Accordingly, as an alternative to the process of registration from a 3D point of view there is the possibility of re-projecting the different images onto a common plane using a 2D projective transformation (Hartley et al., 2003). The only proviso of this approach is that if the object studied is not planar, variations due to relief will be generated and these will affect the subsequent metric analyses.

5 DAMAGE ASSESSMENT

The assessment of damage on façades and civil constructions from multispectral images using non-destructive/non-invasive technologies (Section 3), and the strategies of calibration and registration described (Section 4) will require the generation of hybrid mapping products. These derived products can be: 2D (rectified images and orthoimages for visual interpretation, in true and false color and for quantitative analysis in different regions of the spectrum-visible, infrared, thermal, etc.); 3D (models textured from images from different regions of the spectrum similar to the 2D case depending on whether they are destined for visual or quantitative analysis) and 4D (3D models that are comparable over time, in order to address monitoring processes). They will act as input data in the application of different strategies of multispectral classification and dimensional analysis, with a view to assessing possible chemical and physical pathologies, respectively.

To accomplish the above, here we is proposed a specific methodology that will allow the final user, using data acquired from several sensors, passive and active, multispectral and monochromatic, to assess the pathological damage in different types of construction, either heritage buildings (historical) or civil engineering constructions (infrastructures). The proposed methodology can be broken down into three steps: (i) generation of hybrid cartographic products; (ii) multispectral classification and dimensional analysis based on the hybrid products, and (iii) assessment of the results obtained with graphic, numerical and statistical methods.

5.1 *Generation of hybrid cartographic products*

In view of the sensors that can be used (Section 3), photogrammetric methods and laser scanning methods should be used; these will allow the generation of hybrid cartographic products. Moreover, depending on the complexity of the object to be assessed, 2D cartographic products in the form of image rectifications and true orthoimages, and 3D models that integrate any multispectral band as an additional value, will be considered. Regardless of their type, they can be comparable over time in order to monitor the object. More specifically, when the assessment of the pathological state refers to chemical aspects (e.g., the presence of salts, vegetation, etc.), multispectral classification will be the procedure chosen to accomplish this goal. This classification will use as input data correctly calibrated 2D images (section 4) and with a uniform scale through the use of rectification and orthorectification procedures. It should be noted that this multispectral image classification may be based on auxiliary information, which is sometimes of great value, in the form of 3D or 4D models (multitemporal) that may help the classification process, making the results much more robust. By contrast, when the aspect to be assessed corresponds to physical pathologies (e.g., cracks, detachments, structural changes, etc.), 3D and 4D models will be ideal for performing a dimensional analysis that will allow changes to be detected, displacements and deformations to be assessed in the construction under study.

5.2 *Multispectral classification and dimensional analysis*

Image classification is a fundamental task in the analysis and exploitation of multispectral images. This is especially relevant when the aim is to reduce the complexity of a set of digital levels

belonging to different regions of the electromagnetic spectrum in different homogeneous categories that represent different spectral clusters (spectral signature) or informational classes. The aim here is the render the numerical values acquired by the sensor or sensors interpretable via thematic maps. This process involves the conversion of a multispectral image into another image of the same size and characteristics by means of the assignation of each of the pixels to and informational and/or spectral category. To do so, two classification strategies are used, differentiating between supervised and unsupervised classification:

- *Supervised classification*. This starts out from identification on the image (by an expert user) of pilot areas, known as training polygons. These areas must correspond to, specific informational classes (material, chemical pathology, etc.) identified in situ or via existing images and/or maps. These areas fulfill a dual role; on one hand, some of them are used as a basis for the later segmentation process and, on the other, the others serve as check areas for assessing the results of the classification. Both types of area must show a certain degree of homogeneity and a balanced distribution in different zones of the image so that they will cover different variations within the same informational class. Based on a statistically study, an analysis of the viability of the differentiation among the classes chosen is made. As a result of this analysis, it is possible to modify (remove, fuse or split) the classes and select the spectral bands that best discriminate the problem in hand. Finally, via the application of different segmentation algorithms (Table 1) it will be possible to assign all the pixels of the image to one of the information categories established.

  Most segmentation strategies analyze pixels individually based on their spectral properties. However, there are more sophisticated approaches in which the neighborhood or context of several pixels is considered to adopt the criterion of segmentation. These strategies take into account additional information (e.g., 3D model, multi-temporal observations, fusion of active sensors with passive-optical ones, etc.) and even parametric and non-parametric strategies that allow segmentation tasks to be improved.

- *Unsupervised classification*: pursues the same aim but without requiring the interaction of the user in the definition of the classes, because it is based on an automatic procedure that looks for spectral clustering of the pixels. Finally, the user must analyze the classes detected automatically to establish possible correspondences with the informational classes. The main problem of unsupervised approaches is that sometimes, the results are far from having a relationship with the thematic classes (materials, chemical pathologies, etc.) being sought and there is no biunivocal correspondence between the spectral clusters and informational classes. In these cases, it is necessary to use additional criteria such as modifying the legend, including additional non-spectral criteria (e.g. textures, contextual information, 3D model, etc.) and multi-temporal information.

In view of the above limitations, it is usual to choose *mixed classification strategies*, which first apply an unsupervised classification that will serve as a guide for a later supervised classification. In this way there will be a preliminary discretization of the image in its main spectral classes that will act as a training phase for later application of the different segmentation strategies according to the previously defined training areas of informational classes.

In order to synthesize the most significant algorithms in the field of multispectral image classification, the following table (Table 1) illustrates the most relevant segmentation algorithms associated with each of the classification techniques and their strategies (point/area, parametric/non-parametric).

Table 1. Remote sensing image classification techniques (Li et al. 2014).

Classification techniques	Characteristics	Examples of classifiers

Pixel-based techniques	Each pixel is assumed pure and typically labeled as a single class.	- Unsupervised (e.g. k-means, ISODATA, SOM, hierarchical clustering). - Supervised (e.g. Maximum likelihood, Minimum distance-to-means, Mahalanobis distance, Parallelepiped, k-nearest Neighbours). - Machine learning (e.g. artificial neural network, classification tree, random forest, support vector machine, genetic algorithms).
Sub-pixel-based techniques	Each pixel is considered mixed, and the areal portion of each class is estimated.	- Fuzzy classification, neural networks, regression modeling, regression tree analysis, spectral mixture analysis, fuzzy-spectral mixture analysis.
Object-based techniques	Geographical objects, instead of individual pixels, are considered the basic unit.	- Image segmentation and object-based image analysis techniques (e.g. E-cognition, ArcGIS Feature Analyst).

As a result of the multispectral classification a thematic map in pseudocolour will be obtained, containing the spatial distribution of a given phenomenon such as the type of material and/or chemical pathology associated with a given construction, which this thematic map will serve as a basis for problem-solving and decision-making in different contexts.

Dimensional analysis and *detection of changes* constitute another tool used, in this case for the analysis of possible physical pathologies (quantitative or qualitative) of the construction under analysis. Its application may be made at 2D level (rectification, orthoimage) or at 3D/4D level (multi-temporal models).

From the quantitative point of view, the objects of analysis will be different metric parameters: distances, angles, differences in depth, changes in volume, etc. They will allow a dimensional analysis of the object studied and the detection of possible changes in its structure.

From the qualitative point of view, different images (belonging to the same band or combinations among them) or 3D models can be compared over time by a simple subtraction between images and/or 3D models, previously registered under the same coordinate system and, if necessary, normalized. In geometric terms, the change vector of a pixel will be defined as the vector that joins the spectral position of that pixel on two different dates, its magnitude expressing the intensity of the change, and its direction the type of change, such that it provides quantitative and qualitative information. This method is a valuable tool not only for quantifying the changes but also for their visual interpretation. The results can be highlighted in pseudo-color in order to analyse qualitative changes in the image and/or model.

5.3 *Evaluation of the results obtained*

Assessment of the results obtained in the study of chemical and physical pathologies is oriented in two directions, corresponding to the results of the multispectral classification and the results of the dimensional analysis.

Evaluation of the results of the multispectral classification looks at the precision and reliability globally and in particular for each class. The most widely used analytical tool is known as a confusion matrix (Fig. 10) and consists of performing an empirical evaluation by selecting a sample of pixels from the thematic map obtained (classified image) and comparing the class assigned with respect to the real class determined from reference data, preferably obtained by field sampling (ground truth). In this way it is possible to estimate the percentage of the pixels of each class that have been correctly classified as well as the proportion of errors due to confusion among the different classes. The confusion matrix is a numerical representation of the samples used for evaluation (checking areas), in which the rows (or columns) represent the classes assigned in the classification process and the columns (or rows) are the real classes obtained from the field sampling or from reference data (ground truth) (Fig. 10).

	Reference						
	Class 1	Class 2	Class 3	Class n	Total	User's accuracy	Commission Error
Class 1	x_{11}				x_{1j}	x_{11}/x_{1j}	$x_{1j}-x_{11}/x_{1j}$
Class 2		x_{22}			x_{2j}	x_{22}/x_{2j}	$x_{2j}-x_{22}/x_{2j}$
Class 3			x_{33}		x_{3j}	x_{33}/x_{3j}	$x_{3j}-x_{33}/x_{3j}$
Class n				x_{nn}	x_{nj}	x_{nn}/x_{nj}	$x_{nj}-x_{nn}/x_{nj}$
Total	x_{i1}	x_{i2}	x_{i3}	x_{in}	$\sum x_{ij}$		
Producer's accuracy	x_{11}/x_{i1}	x_{22}/x_{i2}	x_{33}/x_{i3}	x_{nn}/x_{in}			
Omision error	$x_{i1}-x_{11}/x_{i1}$	$x_{i2}-x_{22}/x_{i2}$	$x_{i3}-x_{33}/x_{i3}$	$x_{in}-x_{nn}/x_{in}$			

(Classification — vertical row label)

Omission errors (pixels of the reference class not correctly assigned)

Correctly classified pixels (diagonal matrix)

Commission errors (pixels incorrectly classified to the correct class)

Figure 10. Evaluation of the multispectral classification: Confusion matrix.

In turn, evaluation of the dimensional analysis consists of the diagnosis interpretation of the accuracy and reliability of the metric values obtained (distances, surfaces, volumes, etc.) and must be done following three steps: (i) a check of the reliability of the dimensional analysis via validation of the hypothesis of normality (i.e., the data fits a normal Gaussian curve); (ii) evaluation of the degree of accuracy of the dimensional analysis under the assumption of normality; and (iii) evaluation of the degree of accuracy under the assumption of non-normality.

- The first step involves analyzing whether there are gross errors and/or systematic errors and hence a lack of normality in the data. To accomplish this, the application, in the order of graphic, numerical and statistical methods, is recommended to validate the normality or not of the data. The graphical methods consist of application of QQ-plot analysis and error histograms. QQ-plot compares the quantiles of the empirical distribution against the quantiles of a theoretical normal distribution. If the distribution is normal, the QQ-plot will show a diagonal straight line. Error histograms allow two numerical parameters of great interest for seeing the normality of the data to be derived and these refer to the skewness and kurtosis of the normal distribution. Finally, and also importantly, there is a series of statistical tests that allows the hypothesis of the normality vs. the non-normality of the data to be validated. Nevertheless, it should be noted that such tests are inefficient in cases in which a large number of observables are being handled owing to the Central Limit Theorem (Chang et al. 2006); this is why they are applied last.
- For the second step, application of the usual parameters is recommended (Table 2): mean error (μ), root mean square error (RMSE) and standard deviation (σ).

Table 2. Accuracy measures for DEMs presenting normal distribution of errors (Höhle et al. 2009).

Accuracy measure	Notational expression
Root mean square error	$RMSE = \sqrt{\dfrac{1}{n}\sum_{i=1}^{n}\Delta x_i^2}$
Mean error	$\mu = \dfrac{1}{n}\sum_{i=1}^{n}\Delta x_i$
Standard deviation	$\sigma = \sqrt{\dfrac{1}{(n-1)}\sum_{i=1}^{n}(\Delta x_i - \mu)^2}$

- Finally, in cases in which the hypothesis of normality is not fulfilled, it is necessary to use non-parametric robust estimators such as (Table 3): sample quantiles, median, normalized median absolute deviation (Gencturk et al. 2014) and biweight midvariance (BWMV).

Table 3. Accuracy measures for data not presenting a normal distribution of errors (Höhle et al. 2009).

Accuracy measure	Error type	Notational expression
Median (50% quantile)	Δx	$Q_{\Delta x}(0.5) = m_{\Delta x}$
Normalized median absolute deviation	Δx	$NMAD = 1.4826 \cdot median_i \left(\left| \Delta x_i - m_{\Delta x} \right| \right)$
68.3% quantile	$\left| \Delta x \right|$	$Q_{\left| \Delta x \right|}(0.683)$
95% quantile	$\left| \Delta x \right|$	$Q_{\left| \Delta x \right|}(0.950)$

6. CONCLUSIONS

This chapter points out the significance of multispectral imaging in the assessment and diagnosis of pathologies in construction materials. Thus, this technology occupy an important place in a variety of engineering applications and more specifically in the reconstruction, rehabilitation and restoration fields of damaged constructions due to the quantity of geometric and radiometric information that it is capable of capturing and its ability to analyse large areas in a safe and non-invasiveness way.

In contrast to other inspection techniques, multispectral imaging represents a more versatile tool that allows the use of sensors with different operating principles (active and passive) and remote sensing techniques adjusting to the needs required for each specific case study. Due to the high versatility of the multispectral imaging systems and processing algorithms, this chapter shows the fundamental basis for an efficient and cost-effective damage assessment in constructions. To achieve these goals, the three steps of any operation are discussed: (i) acquisition; (ii) calibration of the data captured; and (iii) pathological analysis. Complementarily a theoretical re-view, to ease the approximation at these systems for non-expert users, is presented.

According to the project analysis requirements, there are several factors to take into account during the choice of the optimal sensor; mainly the spectral and geometric resolution. However, it may counter with other operational factors such as cost and time, being the optimal solution the combination of multispectral and/or mono spectral sensors. Data can be acquired by a different sensor, but requires additional considerations to ensure a perfect homogenization. Moreover, the conversion of the gather values into physical magnitudes is a critical step to classify images of the building into different materials pathologies and damage levels. In this chapter was shown the best practices to solve the sensor registration and radiometric calibration for a wide range of sensors.

The multispectral systems presented allow the generation of hybrid cartographic products valuable in the decision making process to experts in building materials, construction techniques, etc., which can be extended for temporal analysis and maintenance purposes. And even more important, it assesses the building damage quantitatively by the employment of non-parametric statistical methods.

REFERENCES

Armesto-González, J., Riveiro-Rodríguez, B., González-Aguilera, D., & Rivas-Brea, M. T. (2010). Terrestrial laser scanning intensity data applied to damage detection for historical buildings. *Journal of Archaeological Science, 37*(12), 3037-3047.

Bay, H., Tuytelaars, T., & Van Gool, L. (2006). Surf: Speeded up robust features *Computer vision–ECCV 2006* (pp. 404-417): Springer.

Campbell, J. B. (2002). *Introduction to remote sensing*: CRC Press.

Chang, H.-J., Huang, K.-C., & Wu, C.-H. (2006). Determination of sample size in using central limit theorem for weibull distribution. *International journal of information and management sciences, 17*(3), 31-46.

Del Pozo, S., Herrero-Pascual, J., Felipe-García, B., Hernández-López, D., Rodríguez-Gonzálvez, P., & González-Aguilera, D. (2015). Multi-Sensor Radiometric Study to Detect Pathologies in Historical Buildings. *ISPRS-International Archives of the Photogrammetry, Remote Sensing and Spatial Information Sciences, XL-5-W4*, 193-200.

Del Pozo, S., Rodríguez-Gonzálvez, P., Hernández-López, D., & Felipe-García, B. (2014). Vicarious radiometric calibration of a multispectral camera on board an unmanned aerial system. *Remote Sensing, 6*(3), 1918-1937.

Gencturk, B., Hossain, K., Kapadia, A., Labib, E., & Mo, Y.-L. (2014). Use of digital image correlation technique in full-scale testing of prestressed concrete structures. *Measurement, 47*, 505-515.

González-Jorge, H., Gonzalez-Aguilera, D., Rodriguez-Gonzalvez, P., & Arias, P. (2012). Monitoring biological crusts in civil engineering structures using intensity data from terrestrial laser scanners. *Construction and Building Materials, 31*(0), 119-128.

Hartley, R., & Zisserman, A. (2003). *Multiple view geometry in computer vision*: Cambridge university press.

Höhle, J., & Höhle, M. (2009). Accuracy assessment of digital elevation models by means of robust statistical methods. *ISPRS Journal of Photogrammetry and Remote Sensing, 64*(4), 398-406.

Jones, H. G., & Vaughan, R. A. (2010). *Remote sensing of vegetation: principles, techniques, and applications*: Oxford university press.

Kraus, K., & Waldhäusl, P. (1993). *Photogrammetry. Fundamentals and Standard Processes.–Vol. 1.* Bonn: Dümmmler Verlag.

Li, M., Zang, S., Zhang, B., Li, S., & Wu, C. (2014). A Review of Remote Sensing Image Classification Techniques: the Role of Spatio-contextual Information. *European Journal of Remote Sensing, 47*, 389-411.

Lillesand, T. M., Kiefer, R. W., & Chipman, J. W. (2004). *Remote sensing and image interpretation*: John Wiley & Sons Ltd.

Lowe, D. G. (1999). *Object recognition from local scale-invariant features.* Paper presented at the ICCV '99. *Procedings of the International Conference on Computer Vision.*

Lu, W., & Tan, Y.-P. (2003). Color filter array demosaicking: new method and performance measures. *IEEE Transactions on Image Processing, 12*(10), 1194-1210.

Luhmann, T., Piechel, J., & Roelfs, T. (2013). Geometric calibration of thermographic cameras *Thermal Infrared Remote Sensing* (pp. 27-42): Springer.

Magnan, P. (2003). Detection of visible photons in CCD and CMOS: A comparative view. *Nuclear Instruments and Methods in Physics Research Section A: Accelerators, Spectrometers, Detectors and Associated Equipment, 504*(1), 199-212.

Moran, M. S., Bryant, R. B., Clarke, T. R., & Qi, J. (2001). Deployment and calibration of reference reflectance tarps for use with airborne imaging sensors. *Photogrammetric engineering and remote sensing, 67*(3), 273-286.

Moropoulou, A., Labropoulos, K. C., Delegou, E. T., Karoglou, M., & Bakolas, A. (2013). Non-destructive techniques as a tool for the protection of built cultural heritage. *Construction and Building Materials, 48*(0), 1222-1239.

Orlande, H. R., Fudym, O., Maillet, D., & Cotta, R. M. (2011). *Thermal measurements and inverse techniques*: CRC Press.

Sabins, F. F. (2007). *Remote sensing: principles and applications*: Waveland Press.

Sánchez-Aparicio, L., Villarino, A., García-Gago, J., & González-Aguilera, D. (2015). Non-Contact Photogrammetric Methodology to Evaluate the Structural Health of Historical Constructions. *ISPRS-International Archives of the Photogrammetry, Remote Sensing and Spatial Information Sciences, XL-5-W4*, 331-338.

Sánchez-Aparicio, L. J., Riveiro, B., González-Aguilera, D., & Ramos, L. F. (2014). The combination of geomatic approaches and operational modal analysis to improve calibration of finite element models: A case of study in Saint Torcato Church (Guimarães, Portugal). *Construction and Building Materials, 70*(0), 118-129.

Tsang, L., Kong, J. A., & Shin, R. T. (1985). *Theory of microwave remote sensing:* Wiley-Interscience.

Vermote, E. F., Tanré, D., Deuze, J.-L., Herman, M., & Morcette, J.-J. (1997). Second simulation of the satellite signal in the solar spectrum, 6S: An overview. *IEEE Transactions on Geoscience and Remote Sensing, 35*(3), 675-686.

Watt, D. S. (1999). *Building pathology: Principles and practice*: Blackwell Science.

Capítulo V

CONCLUSIONES Y PERSPECTIVAS FUTURAS

5. CONCLUSIONES Y PERSPECTIVAS FUTURAS

5.1. Conclusiones

Esta Tesis Doctoral aborda el análisis de las imágenes multiespectrales en la región visible e infrarroja del espectro electromagnético tomando como base la calibración radiométrica de los sensores empleados. El procedimiento metodológico y los resultados han sido publicados en varias revistas de impacto como artículos de investigación científica o capítulos de libro.

Este capítulo final trata de resumir las contribuciones desarrolladas analizando los resultados más relevantes alcanzados y las directrices a seguir en futuros trabajos. A continuación se recogen las conclusiones relativas al uso de los sensores empleados, tanto de forma individual como conjunta, para los distintos campos de aplicación y estudios realizados.

5.1.1. En líneas generales

- Este periodo de investigación culmina con la adquisición de un alto nivel de conocimiento en lo que a conceptos y fundamentos en espectrometría y radiometría se refiere así como en lo concerniente a los procedimientos de análisis de datos multiespectrales de uso más extendido. Este saber queda recopilado de forma sintética con la publicación del capítulo de libro titulado "Multispectral Imaging: fundamentals, principles and methods to damage assessment in constructions" (ver sección IV.3 de la presente tesis).

- En el campo de la teledetección existen dos métodos comunes de calibración radiométrica: la calibración absoluta y la relativa

(Dinguirard y Slater, 1999). En el caso de la calibración absoluta, la respuesta ofrecida por el sensor se compara con una fuente de radiación conocida y constante; mientras que la calibración relativa consiste en ecualizar la señal de salida del sensor cuando existe una fuente de radiación uniforme. En la presente Tesis Doctoral se han calibrado con éxito dos sensores mediante el método de calibración radiométrico absoluto: una cámara multiespectral de bajo coste y un láser escáner terrestre.

- La calibración radiométrica del sensor pasivo (cámara multiespectral) se llevó a cabo en una campaña de campo y a través del método vicario basado en radiancias. Por su lado, la calibración radiométrica del sensor activo (laser escáner terrestre) se llevó a cabo en laboratorio mediante el método vicario de reflectancias (Slater et al., 1987). En ambos casos, la radiación de entrada al sensor (de fuente natural o artificial) fue comparada con la salida digital arrojada por cada sensor obteniéndose un buen grado de ajuste para ambos sensores.

- No todos los sistemas de adquisición de datos tienen un comportamiento interno lineal por diseño. Tras los resultados de la calibración absoluta de ambos sensores (cámara multiespectral pasiva y láser escáner terrestre activo) se observó que ambos tenían un comportamiento interno diferente. Mientras que la señal del sensor pasivo sigue una función lineal, en el caso del sensor activo sigue una función exponencial y/o logarítmica que a su vez depende de la distancia a la que se han adquirido los datos.

5.1.2. La calibración radiométrica

- Se ha verificado la viabilidad de usar distintas superficies artificiales de bajo coste (vinilos y lonas) como superficies de control para realizar la calibración radiométrica de sensores por el método vicario.

- Es posible llevar a cabo estudios remotos aéreos sin necesidad de realizar correcciones atmosféricas mediante la embarcación de

sensores en sistemas aéreos no tripulados a una altura moderada (<100 m) o trabajando a nivel terreno.

- Gracias al apoyo del software MULRACS desarrollado por los autores, se ha conseguido automatizar la calibración radiométrica de los sensores pasivos proporcionando rigurosidad al proceso, evitando introducir medidas erróneas en los cálculos gracias a la implementación de algoritmos robustos de resolución en el mismo.

- La calibración radiométrica de los sensores depara mejoras significativas en los resultados de clasificación de las imágenes, lográndose mejoras de entorno al 34% en fiabilidad tras realizar la calibración radiométrica.

5.1.3. La cámara Mini MCA-6 como sensor remoto pasivo

- La configuración espectral de la cámara Mini MCA-6 (530-801 nm) es ideal para realizar estudios de coberturas vegetales como muestran los resultados del Capítulo II. No obstante puede ser utilizada con resultados muy prometedores en campos como la geología y la detección de humedades desde la apuesta por su hibridación con algún otro sensor remoto.

- Antes de realizar la calibración radiométrica del sensor multiespectral fue necesario estudiar y corregir ciertos errores sistemáticos (errores de ruido de fondo y viñeteo) que el sensor transmitía a las imágenes distorsionando la realidad para eliminar trasladar estos errores al análisis radiométrico final.

- Si bien el rango espectral de la cámara Mini MCA-6 no es el idóneo para el estudio de rocas, fue posible encontrar diferencias entre algunos tipos de roca sedimentaria aun cuando este tipo de cobertura terrestre presenta muchas heterogeneidades superficiales que redundan en dificultades añadidas para su estudio radiométrico a través sensores pasivos. Asimismo, las tomas de datos a nivel terreno tienen el hándicap de que capturan

posibles sombras proyectadas en la superficie de las rocas lo que dificulta aún más su análisis.

5.1.4. Los laser escáner terrestres como sensores remotos activos

- Los datos de intensidad láser están menos influenciados por los cambios en las condiciones de iluminación que las imágenes capturadas por los sensores pasivos, de manera que mediante su uso se han observado mejoras significativas en los resultados de los análisis espectrales, incluso cuando a calibración radiométrica no se ha aplicado o no estaba resuelta.

- Para el caso concreto del FARO Focus3D (905 nm) y del Riegl LMS Z390i (1550 nm), se han obtenido buenos resultados en la detección de humedades en diversos materiales de construcción debido a que el comportamiento espectral de dicha patología para este caso concreto de materiales se hace característica para la región infrarroja del espectro.

- Los láser escáner terrestres aportan un valor añadido a los datos radiométricos ya que proporcionan escala y por lo tanto es posible cuantificar cualquier patología o daño caracterizado por sus datos de intensidad.

- A pesar del comportamiento interno desconocido de los láser escáner terrestres (black-box), es posible realizar una calibración radiométrica satisfactoria de los mismos para obtener valores físicos de reflectancia de cualquier material dado que la fuente de luz es controlada (sensor activo).

5.1.5. La fusion sensorial

- Se ha conseguido con éxito realizar una hibridación sensorial de hasta cuatro sensores diferentes, dos activos (laser escáner terrestres) y dos pasivos (una cámara multiespectral y una cámara digital convencional).

▪ A través de la fusión sensorial no solo se ha validado la capacidad de automatizar la detección de humedad sino que gracias a ella se ha podido delimitar y cuantificar de forma precisa su afección superficial.

▪ Los datos procedentes de los sensores pasivos, cámara multiespectral y cámara digital, estaban condicionados tanto por el registro de sus bandas espectrales como por la influencia de las condiciones de iluminación del momento de captura.

5.2. Perspectivas futuras

Tras realizar los trabajos de investigación desarrollaos durante esta Tesis Doctoral se abren nuevas líneas de investigación y mejoras para complementar y optimizar los estudios multiespectrales remotos a través de la fusión de sensores activos y pasivos.

5.2.1. En líneas generales

▪ No hay que olvidar que la mayor parte de las superficies de los materiales tienen un comportamiento no Lambertiano, al contrario de lo que se presupone a primera instancia. Mediante el estudio del comportamiento anisotrópico de los materiales se conseguiría mejorar la caracterización de su reflectancia y por ende, el análisis espectral de los mismos ya que la radiación reflejada por cualquier superficie depende tanto de la orientación de la fuente radiante como del punto de vista de la adquisición de los datos.

5.2.2. La calibración radiométrica y la cámara Mini MCA-6 como sensor remoto pasivo

▪ Se propone realizar una calibración radiométrica del sensor en condiciones controladas de laboratorio para llevar un seguimiento de los posibles cambios que puedan producirse en sus coeficientes de calibración con el uso y el paso de los años.

5.2.3. Los láser escáner terrestres como sensors remotos activos

- Se propone ampliar el abanico de posibilidades que ofrece actualmente el software de calibración radiométrico MULRACS de tal forma que sea posible no solo la calibración de sensores pasivos sino también de sensores activos, lo que contribuiría a la automatización completa del proceso de hibridación sensorial a la vez que se favorecería el uso de este tipo de sensores para realizar estudios espectrales de los materiales.

- El ángulo de incidencia de un haz láser, tal y como establece la Ley de Lambert, es un factor relevante y que afecta a la intensidad de retorno capturada por el láser, analizada en los estudios radiométricos. Si bien en los trabajos realizados durante esta investigación sus efectos han sido minimizados mediante un diseño y configuración concretos de la toma de datos, se propone, siempre que sea posible, estimar su magnitud y corregir los datos para mejorar los resultados de futuros análisis.

5.2.4. La fusion sensorial

- La posibilidad de trabajar con láser escáner terrestres en el rango visible y sensores pasivos en el rango SWIR ayudaría a complementar estos estudios de los cuales se sacarían conclusiones más completas acerca de los principios de funcionamiento y rangos espectrales para cada caso de estudio concreto. Además, el uso de sensores hiperespectrales también abriría nuevos desafíos en este sentido.

- Se propone la técnica de pansharpening como método de optimización de los resultados tras la fusión sensorial tratando de combinar la mayor resolución especial y radiométrica ofrecida por cada uno de los sensores utilizados.

REFERENCIAS

6. REFERENCES

Barrett, E.C. *Introduction to environmental remote sensing*. Routledge: 2013.

Bartholomé, E.; Belward, A. Glc2000: A new approach to global land cover mapping from earth observation data. *International Journal of Remote Sensing* **2005**, *26*, 1959-1977.

Biggar, S.; Slater, P.; Gellman, D. Uncertainties in the in-flight calibration of sensors with reference to measured ground sites in the 0.4-1.1 μm range. *Remote Sensing of Environment* **1994**, *48*, 245-252.

Brooke, C.J. *Ground-based remote sensing*. Institute of Field Archaeologists: 1989.

Bruegge, C.; Chrien, N.; Haner, D. A spectralon brf data base for misr calibration applications. *Remote sensing of environment* **2001**, *77*, 354-366.

Campbell, J.B. *Introduction to remote sensing*. CRC Press: 2002.

Cohen, J. A coefficient of agreement for nominal scales. *Educational and psychological measurement* **1960**, *20*, 37-46.

Colwell, R.N. Some practical applications of multiband spectral reconnaissance. *American Scientist* **1961**, 9-36.

Davis, S.M.; Landgrebe, D.A.; Phillips, T.L.; Swain, P.H.; Hoffer, R.M.; Lindenlaub, J.C.; Silva, L.F. Remote sensing: The quantitative approach. *New York, McGraw-Hill International Book Co., 1978. 405 p.* **1978**, *1*.

Davis, G. History of the NOAA satellite program. *Journal of Applied Remote Sensing* **2007**, *1*, 012504-012518.

Dinguirard, M.; Slater, P.N. Calibration of space-multispectral imaging sensors: A review. *Remote Sensing of Environment* **1999**, *68*, 194-205.

Grum, F. *Radiometry*. Elsevier: 2012.

Honkavaara, E.; Arbiol, R.; Markelin, L.; Martinez, L.; Cramer, M.; Bovet, S.; Chandelier, L.; Ilves, R.; Klonus, S.; Marshal, P. Digital airborne photogrammetry—a new tool for quantitative remote sensing?—a state-of-the-art review on radiometric aspects of digital photogrammetric images. *Remote Sensing* **2009**, *1*, 577-605.

Hunt, G. Spectroscopic properties of rocks and minerals. *Handbook of physical properties of rocks* **1982**, *1*, 295-385.

Jensen, J.R.; Lulla, K. *Introductory digital image processing: A remote sensing perspective*. Prentice Hall: 1987.

Joseph, G. *Fundamentals of remote sensing*. Universities Press: 2005.

Justice, C.; Townshend, J.; Vermote, E.; Masuoka, E.; Wolfe, R.; Saleous, N.; Roy, D.; Morisette, J. An overview of modis land data processing and product status. *Remote sensing of Environment* **2002**, *83*, 3-15.

Kaasalainen, S.; Ahokas, E.; Hyyppä, J.; Suomalainen, J. Study of surface brightness from backscattered laser intensity: Calibration of laser data. *IEEE Geoscience and Remote Sensing Letters,* **2005**, *2*, 255-259.

Knoth, C.; Klein, B.; Prinz, T.; Kleinebecker, T. Unmanned aerial vehicles as innovative remote sensing platforms for high-resolution infrared imagery to support restoration monitoring in cut-over bogs. *Applied Vegetation Science* **2013**, *16*, 509-517.

Krarup, T.; Juhl, J.; Kubik, K. Gotterdammerung over least squares adjustment. *International archives of photogrammetry* **1980**, 369-378.

Lillesand, T.; Kiefer, R.W.; Chipman, J. *Remote sensing and image interpretation*. John Wiley & Sons: 2014.

Lo, C.; Yang, X. In *Some practical considerations of relative radiometric normalization of multidate landsat mss data for land use change detection*, Proceedings of the ASPRS/RTI 1998 Annual Convention, 1998; pp 1184-1193.

Palmer, J.M. In Calibration of satellite sensors in the thermal infrared, San Diego'92, 1993; International Society for Optics and Photonics: pp 108-117.

Parr, A.C.; Datla, R.; Gardner, J. *Optical radiometry*. Academic Press: 2005; Vol. 41.

Pohl, C.; Van Genderen, J.L. Review article multisensor image fusion in remote sensing: Concepts, methods and applications. *International journal of remote sensing* **1998**, *19*, 823-854.

Richards, J.A.; Richards, J. *Remote sensing digital image analysis*. Springer: 1999; Vol. 3.

Robinove, C.J. Computation with physical values from landsat digital data. *Photogrammetric Engineering and Remote Sensing* **1982**, *48*, 781-784.

Schowengerdt, R.A. *Remote sensing: Models and methods for image processing*. Academic press: 2006.

Shaw, G.A.; Burke, H.-h.K. Spectral imaging for remote sensing. *Lincoln Laboratory Journal* **2003**, *14*, 3-28.

Slater, P.; Biggar, S.; Holm, R.; Jackson, R.; Mao, Y.; Moran, M.; Palmer, J.; Yuan, B. Reflectance-and radiance-based methods for the in-flight absolute calibration of multispectral sensors. *Remote Sensing of Environment* **1987**, *22*, 11-37.

Slater, P.N.; Biggar, S.F.; Thome, K.J.; Gellman, D.I.; Spyak, P.R. Vicarious radiometric calibrations of eos sensors. *Journal of Atmospheric and Oceanic Technology* **1996**, *13*, 349-359.

Thorne, K.; Markharn, B.; Barker, P.S.; Biggar, S. Radiometric calibration of landsat. *Photogrammetric Engineering & Remote Sensing* **1997**, *63*, 853-858.

Zhang, L.; Furumi, S.; Muramatsu, K.; Fujiwara, N.; Daigo, M.; Zhang, L. Sensor-independent analysis method for hyperspectral data based on the pattern decomposition method. *International Journal of Remote Sensing* **2006**, *27*, 4899-4910.

Zhou, G.; Ambrosia, V.; Gasiewski, A.J.; Bland, G. Foreword to the special issue on unmanned airborne vehicle (uav) sensing systems for earth observations. *IEEE Transactions on Geoscience and Remote Sensing* **2009**, *3*, 687-689.

APÉNDICE A

FACTOR DE IMPACTO Y OTROS CRITERIOS DE CALIDAD DE LAS REVISTAS

FACTOR DE IMPACTO Y OTROS ÍNDICES DE CALIDAD DE LAS REVISTAS

Artículos I y III:

- *Vicarious radiometric calibration of a multispectral camera on board an unmanned aerial system*
- *Multispectral radiometric analysis of façades to detect pathologies from active and passive remote sensing*

Revista:	**Remote Sensing**
Editorial	**MDPI AG**
ISSN:	**2072-4292**
Factor de impacto (2014):	**3.180**
Ranking:	**5/28**
Cuartil:	**Q1**

ISI Web of Knowledge℠

Journal Citation Reports®

WELCOME | ? HELP | RETURN TO LIST

2014 JCR Science Edition

Journal: Remote Sensing

Mark	Journal Title	ISSN	Total Cites	Impact Factor	5-Year Impact Factor	Immediacy Index	Citable Items	Cited Half-life	Citing Half-life
☐	REMOTE SENS-BASEL	2072-4292	3061	3.180	3.257	0.505	572	2.5	7.9

Cited Journal 📊　Citing Journal 📊　Source Data　Journal Self Cites

CITED JOURNAL DATA | CITING JOURNAL DATA | 📊 IMPACT FACTOR TREND | RELATED JOURNALS

Journal Information ⓘ ▲

Full Journal Title: Remote Sensing
ISO Abbrev. Title: Remote Sens.
JCR Abbrev. Title: REMOTE SENS-BASEL
ISSN: 2072-4292
Issues/Year: 12
Language: ENGLISH
Journal Country/Territory: SWITZERLAND
Publisher: MDPI AG
Publisher Address: POSTFACH, CH-4005 BASEL, SWITZERLAND
Subject Categories: REMOTE SENSING 　SCOPE NOTE

Eigenfactor® Metrics
Eigenfactor® Score
0.01044
Article Influence®
Score
0.772

VIEW JOURNAL SUMMARY LIST | VIEW CATEGORY DATA

Journal Rank in Categories: 📊 JOURNAL RANKING

Journal Impact Factor ⓘ ▲

Cites in 2014 to items published in: 2013 = 893 　　Number of items published in: 2013 = 316
　　　　　　　　　　　　　　　　　　2012 = 697 　　　　　　　　　　　　　　　　　　2012 = 184
　　　　　　　　　　　　　　　　　Sum: 1590 　　　　　　　　　　　　　　　　　Sum: 500

Calculation: Cites to recent items 　　　$\frac{1590}{500}$ = **3.180**
　　　　　　　Number of recent items

5-Year Journal Impact Factor ⓘ ▲

Cites in {2014} to items published in: 2013 = 893 　　Number of items published in: 2013 = 316
　　　　　　　　　　　　　　　　　　2012 = 697 　　　　　　　　　　　　　　　　　　2012 = 184
　　　　　　　　　　　　　　　　　　2011 = 513 　　　　　　　　　　　　　　　　　　2011 = 137
　　　　　　　　　　　　　　　　　　2010 = 428 　　　　　　　　　　　　　　　　　　2010 = 141
　　　　　　　　　　　　　　　　　　2009 = 241 　　　　　　　　　　　　　　　　　　2009 = 73
　　　　　　　　　　　　　　　　　Sum: 2772 　　　　　　　　　　　　　　　　　Sum: 851

Calculation: Cites to recent items 　　　$\frac{2772}{851}$ = **3.257**
　　　　　　　Number of recent items

Journal Self Cites ⓘ ▲

The tables show the contribution of the journal's self cites to its impact factor. This information is also represented in the cited journal graph.

Total Cites	3061	Self Cites	920 (30% of 3061)
Cites to Years Used in Impact Factor Calculation	1590	**Self Cites to Years Used in Impact Factor Calculation**	528 (33% of 1590)
Impact Factor	3.180	**Impact Factor without Self Cites**	2.124

Journal Immediacy Index ⓘ ▲

Cites in 2014 to items published in 2014 = 289
Number of items published in 2014   = 572

Calculation: Cites to current items   289 = **0.505**
                Number of current items   572

Journal Cited Half-Life ⓘ ▲

The cited half-life for the journal is the median age of its items cited in the current JCR year. Half of the citations to the journal are to items published within the cited half-life.
Cited Half-Life: 2.5 years

Breakdown of the citations *to the journal* by the cumulative percent of 2014 cites to items published in the following years:

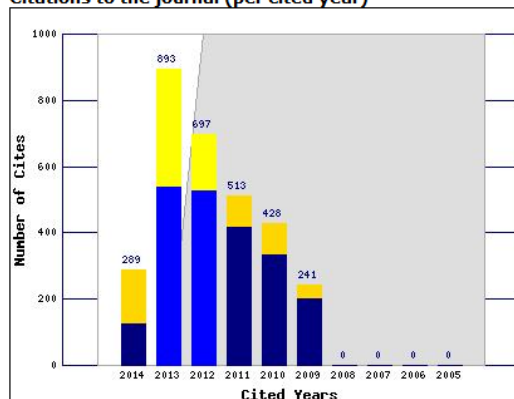| Cited Year	2014	2013	2012	2011	2010	2009	2008	2007	2006	2005	2004-all
# Cites from 2014	289	893	697	513	428	241	0	0	0	0	0
Cumulative %	9.44	38.61	61.39	78.14	92.13	100.00	100.00	100.00	100.00	100.00	100

Cited Half-Life Calculations:
The cited half-life calculation finds the number of publication years from the current JCR year that account for 50% of citations received by the journal. Read help for more information on the calculation.

Cited Journal Graph ⓘ ▲

Click here for Cited Journal data table

This graph shows the distribution by cited year of citations to items published in the journal REMOTE SENS-BASEL.
Citations to the journal (per cited year)

- The white/grey division indicates the cited half-life (if < 10.0). Half of the journal's cited items were published more recently than the cited half-life.

- The top (gold) portion of each column indicates Journal Self Citations: citations to items in the journal from items in the same journal.

- The bottom (blue) portion of each column indicates Non-Self Citations: citations to the journal from items in other journals.

- The two lighter columns indicate citations used to calculate the Impact Factor (always the 2nd and 3rd columns).

Journal Citing Half-Life ⓘ ▲

The citing half-life for the journal is the median age of the items the journal cited in the current JCR year. Half of the citations in the journal are to items published within the citing half-life.
Citing Half-Life: 7.9 years

Breakdown of the citations *from the journal* by the cumulative percent of 2014 cites to items published in the following years:

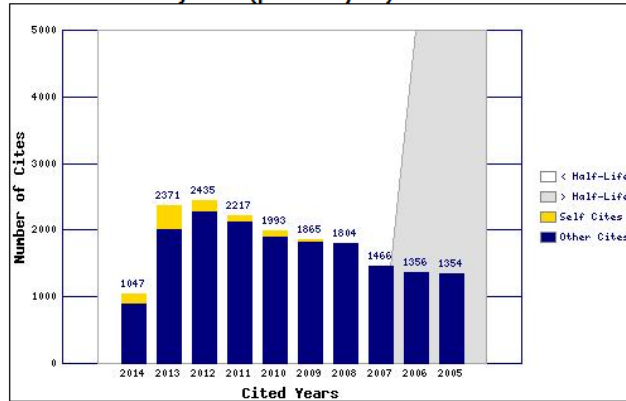| Cited Year	2014	2013	2012	2011	2010	2009	2008	2007	2006	2005	2004-all
# Cites from 2014	1047	2371	2435	2217	1993	1865	1804	1466	1356	1354	12068
Cumulative %	3.49	11.40	19.53	26.92	33.57	39.79	45.81	50.70	55.22	59.74	100

Citing Half-Life Calculations:
The citing half-life calculation finds the number of publication years from the current JCR year that account for 50% of citations in the journal. Read help for more information on the calculation.

Citing Journal Graph ⓘ ▲

Click here for Citing Journal data table

This graph shows the distribution by cited year of citations from current-year items in the journal REMOTE SENS-BASEL.

Citations from the journal (per cited year)

- The white/grey division indicates the citing half-life (if < 10.0). Half of the citations from the journal's current items are to items published more recently than the citing half-life.

- The top (gold) portion of each column indicates Journal Self-Citations: citations from items in the journal to items in the same journal.

- The bottom (blue) portion of each column indicates Non-Self Citations: citations from the journal to items in other journals.

Journal Source Data ⓘ ▲

	Citable items			
	Articles	**Reviews**	**Combined**	**Other items**
Number in JCR year 2014 (A)	555	17	572	10
Number of references (B)	27646	2188	29834	142.00
Ratio (B/A)	49.8	128.7	52.2	14.2

🏷 Rank in Category: Remote Sensing

Journal Ranking ⓘ

For **2014**, the journal **Remote Sensing** has an Impact Factor of **3.180**.

This table shows the ranking of this journal in its subject categories based on Impact Factor.

Category Name	**Total Journals in Category**	**Journal Rank in Category**	**Quartile in Category**
REMOTE SENSING	28	5	Q1

Category Box Plot ⓘ

For **2014**, the journal **Remote Sensing** has an Impact Factor of **3.180**.

This is a box plot of the subject category or categories to which the journal has been assigned. It provides information about the distribution of journals based on Impact Factor values. It shows median, 25th and 75th percentiles, and the extreme values of the distribution.
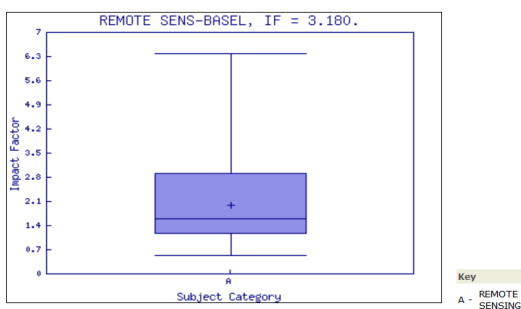
Artículo II:

- *Discrimination between sedimentary rocks from close-range visible and very-near infrared images*

Revista:	**PLOS One**
Editorial	**Public Library of Science**
ISSN:	**1932-6203**
Factor de impacto (2014):	**3.234**
Ranking:	**8/55**
Cuartil:	**Q1**

ISI Web of Knowledge℠

Journal Citation Reports®

WELCOME   ? HELP   RETURN TO LIST   **2014 JCR Science Edition**

📄 Journal: PLoS One

Mark	Journal Title	ISSN	Total Cites	Impact Factor	5-Year Impact Factor	Immediacy Index	Citable Items	Cited Half-life	Citing Half-life
☐	PLOS ONE	1932-6203	332716	3.234	3.702	0.489	30040	2.7	7.7

Cited Journal 📊   Citing Journal 📊   Source Data   Journal Self Cites

CITED JOURNAL DATA   CITING JOURNAL DATA   📊 IMPACT FACTOR TREND   RELATED JOURNALS

Journal Information ⓘ   ▲

Full Journal Title: PLoS One
ISO Abbrev. Title: PLoS One
JCR Abbrev. Title: PLOS ONE
ISSN: 1932-6203
Issues/Year: 0
Language: ENGLISH
Journal Country/Territory: UNITED STATES
Publisher: PUBLIC LIBRARY SCIENCE
Publisher Address: 1160 BATTERY STREET, STE 100, SAN FRANCISCO, CA 94111
Subject Categories: MULTIDISCIPLINARY SCIENCES   SCOPE NOTE

Eigenfactor® **Metrics**
Eigenfactor® **Score**
1.53341
Article Influence®
Score
1.209

📄 VIEW JOURNAL SUMMARY LIST   📋 VIEW CATEGORY DATA

Journal Rank in Categories: 📊 JOURNAL RANKING

Journal Impact Factor ⓘ   ▲

Cites in 2014 to items published in: 2013 = 82075   Number of items published in: 2013 = 31498
                                     2012 = 95631   2012 = 23447
                                     Sum: 177706   Sum: 54945

Calculation: Cites to recent items   177706   = **3.234**
             Number of recent items   54945

5-Year Journal Impact Factor ⓘ   ▲

Cites in {2014} to items published in: 2013 = 82075   Number of items published in: 2013 = 31498
                                       2012 = 95631   2012 = 23447
                                       2011 = 63047   2011 = 13782
                                       2010 = 33288   2010 = 6729
                                       2009 = 21581   2009 = 4403
                                       Sum: 295622   Sum: 79859

Calculation: Cites to recent items   295622   = **3.702**
             Number of recent items   79859

Journal Self Cites ⓘ   ▲

The tables show the contribution of the journal's self cites to its impact factor. This information is also represented in the cited journal graph.

Total Cites	332716	Self Cites	35722 (10% of 332716)
Cites to Years Used in Impact Factor Calculation	177706	**Self Cites to Years Used in Impact Factor Calculation**	19159 (10% of 177706)
Impact Factor	3.234	**Impact Factor without Self Cites**	2.886

Journal Immediacy Index ⓘ ▲

Cites in 2014 to items published in 2014 = 14697
Number of items published in 2014   = 30040
Calculation: Cites to current items   14697   =**0.489**
              Number of current items   30040

Journal Cited Half-Life ⓘ ▲

The cited half-life for the journal is the median age of its items cited in the current JCR year. Half of the citations to the journal are to items published within the cited half-life.
Cited Half-Life: 2.7 years

Breakdown of the citations *to the journal* by the cumulative percent of 2014 cites to items published in the following years:

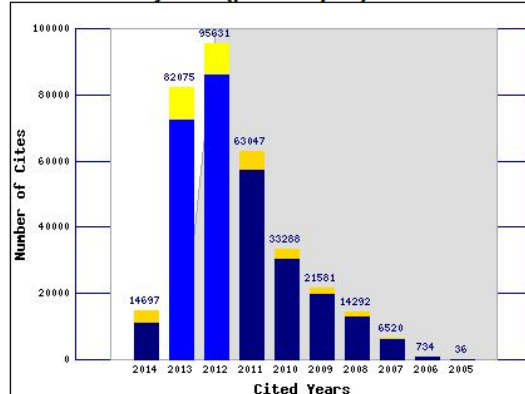| Cited Year	2014	2013	2012	2011	2010	2009	2008	2007	2006	2005	2004-all
# Cites from 2014	14697	82075	95631	63047	33288	21581	14292	6520	734	36	815
Cumulative %	4.42	29.09	57.83	76.78	86.78	93.27	97.56	99.52	99.74	99.76	100

Cited Half-Life Calculations:
The cited half-life calculation finds the number of publication years from the current JCR year that account for 50% of citations received by the journal. Read help for more information on the calculation.

Cited Journal Graph ⓘ ▲

Click here for Cited Journal data table

This graph shows the distribution by cited year of citations to items published in the journal PLOS ONE.
Citations to the journal (per cited year)

- The white/grey division indicates the cited half-life (if < 10.0). Half of the journal's cited items were published more recently than the cited half-life.

- The top (gold) portion of each column indicates Journal Self Citations: citations to items in the journal from items in the same journal.

- The bottom (blue) portion of each column indicates Non-Self Citations: citations to the journal from items in other journals.

- The two lighter columns indicate citations used to calculate the Impact Factor (always the 2nd and 3rd columns).

Journal Citing Half-Life ⓘ ▲

The citing half-life for the journal is the median age of the items the journal cited in the current JCR year. Half of the citations in the journal are to items published within the citing half-life.
Citing Half-Life: 7.7 years

Breakdown of the citations *from the journal* by the cumulative percent of 2014 cites to items published in the following years:

Cited Year	2014	2013	2012	2011	2010	2009	2008	2007	2006	2005	2004-all
# Cites from 2014	24009	102139	122681	115560	107925	98919	89936	81869	74485	68170	544713
Cumulative %	1.68	8.82	17.40	25.47	33.02	39.94	46.22	51.95	57.15	61.92	100

Citing Half-Life Calculations:
The citing half-life calculation finds the number of publication years from the current JCR year that account for 50% of citations in the journal. Read help for more information on the calculation.
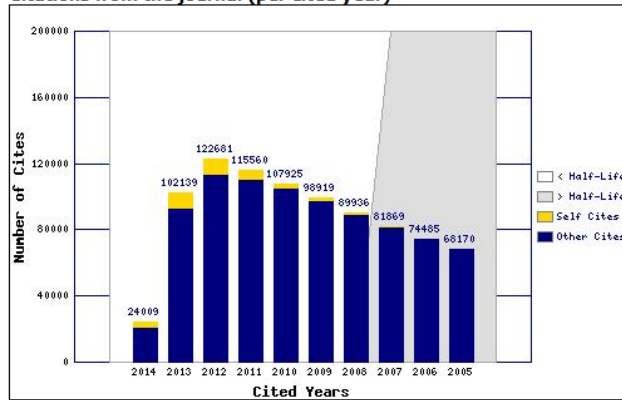
Citing Journal Graph ⓘ ▲

Click here for Citing Journal data table

This graph shows the distribution by cited year of citations from current-year items in the journal PLOS ONE.

Citations from the journal (per cited year)

- The white/grey division indicates the citing half-life (if < 10.0). Half of the citations from the journal's current items are to items published more recently than the citing half-life.

- The top (gold) portion of each column indicates Journal Self-Citations: citations from items in the journal to items in the same journal.

- The bottom (blue) portion of each column indicates Non-Self Citations: citations from the journal to items in other journals.

Journal Source Data ⓘ ▲

	Citable items			
	Articles	**Reviews**	**Combined**	**Other items**
Number in JCR year 2014 (A)	29777	263	30040	1439
Number of references (B)	1410713	16918	1427631	
Ratio (B/A)	47.4	64.3	47.5	0.0

🏷 Rank in Category: PLoS One

Journal Ranking ⓘ

For **2014**, the journal **PLoS One** has an Impact Factor of **3.234**.

This table shows the ranking of this journal in its subject categories based on Impact Factor.

Category Name	**Total Journals in Category**	**Journal Rank in Category**	**Quartile in Category**
MULTIDISCIPLINARY SCIENCES	57	9	Q1

Category Box Plot ⓘ

For **2014**, the journal **PLoS One** has an Impact Factor of **3.234**.

This is a box plot of the subject category or categories to which the journal has been assigned. It provides information about the distribution of journals based on Impact Factor values. It shows median, 25th and 75th percentiles, and the extreme values of the distribution.

PLOS ONE, IF = 3.234.

Key

A - MULTIDISCIPL
      SCIENCES
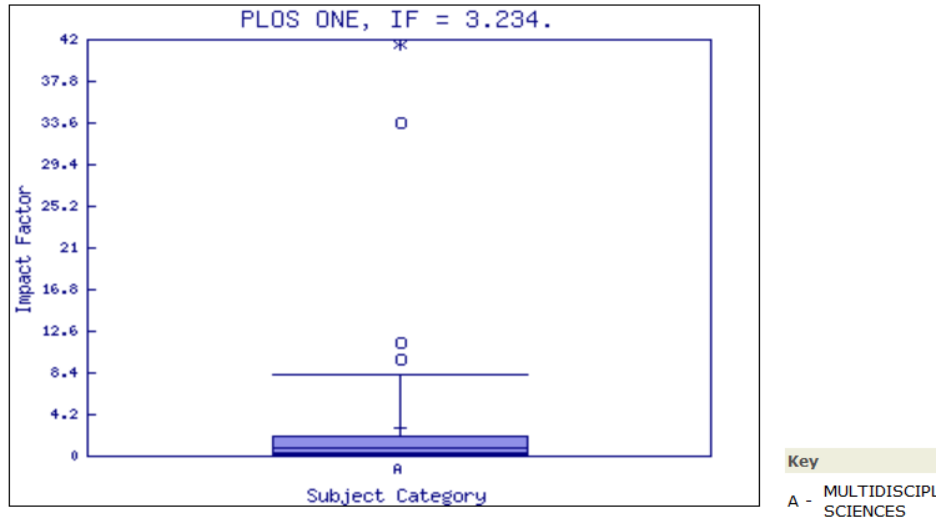
Artículo IV:

- *Automatic mapping of moisture affectation in exposed concrete structures by fusing different wavelength remote sensors*

Revista:	**Structural Control and Health Monitoring**
Editorial	**Wiley Online Library**
ISSN:	**1545-2255**
Factor de impacto (2014):	**2.133**
Ranking:	**8/59 (constructions & building technology)**
Cuartil:	**Q1**

ISI Web of Knowledge℠

Journal Citation Reports®

WELCOME | ? HELP | RETURN TO LIST

2014 JCR Science Edition

Journal: Structural Control & Health Monitoring

Mark	Journal Title	ISSN	Total Cites	Impact Factor	5-Year Impact Factor	Immediacy Index	Citable Items	Cited Half-life	Citing Half-life
☐	STRUCT CONTROL HLTH	1545-2255	1128	2.133	2.309	0.369	84	4.8	8.9

Cited Journal ▥   Citing Journal ▥   Source Data   Journal Self Cites

CITED JOURNAL DATA   CITING JOURNAL DATA   ▥ IMPACT FACTOR TREND   RELATED JOURNALS

Journal Information ⓘ   ▲

Full Journal Title: Structural Control & Health Monitoring
ISO Abbrev. Title: Struct. Control. Health Monit.
JCR Abbrev. Title: STRUCT CONTROL HLTH
ISSN: 1545-2255
Issues/Year: 12
Language: ENGLISH
Journal Country/Territory: ENGLAND
Publisher: WILEY-BLACKWELL
Publisher Address: 111 RIVER ST, HOBOKEN 07030-5774, NJ,
Subject Categories: CONSTRUCTION & BUILDING TECHNOLOGY   SCOPE NOTE

Eigenfactor® Metrics
Eigenfactor® Score
0.00341
Article Influence® Score
0.738

VIEW JOURNAL SUMMARY LIST   VIEW CATEGORY DATA

ENGINEERING, CIVIL   SCOPE NOTE

VIEW JOURNAL SUMMARY LIST   VIEW CATEGORY DATA

INSTRUMENTS & INSTRUMENTATION   SCOPE NOTE

VIEW JOURNAL SUMMARY LIST   VIEW CATEGORY DATA

Journal Rank in Categories: ▤ JOURNAL RANKING

Journal Impact Factor ⓘ   ▲

Cites in 2014 to items published in: 2013 = 185   Number of items published in: 2013 = 86
  2012 = 120   2012 = 57
  Sum: 305   Sum: 143

Calculation: $\dfrac{\text{Cites to recent items}}{\text{Number of recent items}} \quad \dfrac{305}{143} = 2.133$

5-Year Journal Impact Factor ⓘ   ▲

Cites in {2014} to items published in: 2013 = 185   Number of items published in: 2013 = 86
  2012 = 120   2012 = 57
  2011 = 134   2011 = 56
  2010 = 115   2010 = 47
  2009 = 118   2009 = 45
  Sum: 672   Sum: 291

Calculation: $\dfrac{\text{Cites to recent items}}{\text{Number of recent items}} \quad \dfrac{672}{291} = 2.309$

Journal Self Cites ⓘ

The tables show the contribution of the journal's self cites to its impact factor. This information is also represented in the cited journal graph.

Total Cites	1128	Self Cites	226 (20% of 1128)
Cites to Years Used in Impact Factor Calculation	305	Self Cites to Years Used in Impact Factor Calculation	59 (19% of 305)
Impact Factor	2.133	Impact Factor without Self Cites	1.720

Journal Immediacy Index ⓘ

Cites in 2014 to items published in 2014 = 31
Number of items published in 2014   = 84

Calculation: Cites to current items   31   **= 0.369**
                Number of current items   84

Journal Cited Half-Life ⓘ

The cited half-life for the journal is the median age of its items cited in the current JCR year. Half of the citations to the journal are to items published within the cited half-life.
Cited Half-Life: 4.8 years

Breakdown of the citations *to the journal* by the cumulative percent of 2014 cites to items published in the following years:

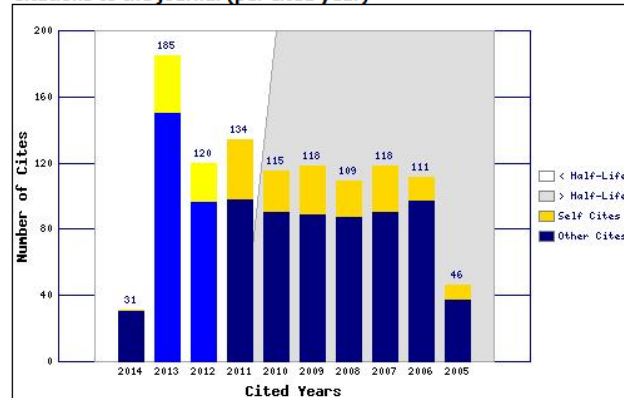| Cited Year	2014	2013	2012	2011	2010	2009	2008	2007	2006	2005	2004-all
# Cites from 2014	31	185	120	134	115	118	109	118	111	46	41
Cumulative %	2.75	19.15	29.79	41.67	51.86	62.32	71.99	82.45	92.29	96.37	100

Cited Half-Life Calculations:
The cited half-life calculation finds the number of publication years from the current JCR year that account for 50% of citations received by the journal. Read help for more information on the calculation.

Cited Journal Graph ⓘ

Click here for Cited Journal data table

This graph shows the distribution by cited year of citations to items published in the journal STRUCT CONTROL HLTH.

Citations to the journal (per cited year)

- The white/grey division indicates the cited half-life (if < 10.0). Half of the journal's cited items were published more recently than the cited half-life.

- The top (gold) portion of each column indicates Journal Self Citations: citations to items in the journal from items in the same journal.

- The bottom (blue) portion of each column indicates Non-Self Citations: citations to the journal from items in other journals.

- The two lighter columns indicate citations used to calculate the Impact Factor (always the 2nd and 3rd columns).

Journal Citing Half-Life ⓘ

The citing half-life for the journal is the median age of the items the journal cited in the current JCR year. Half of the citations in the journal are to items published within the citing half-life.
Citing Half-Life: 8.9 years

Breakdown of the citations *from the journal* by the cumulative percent of 2014 cites to items published in the following years:

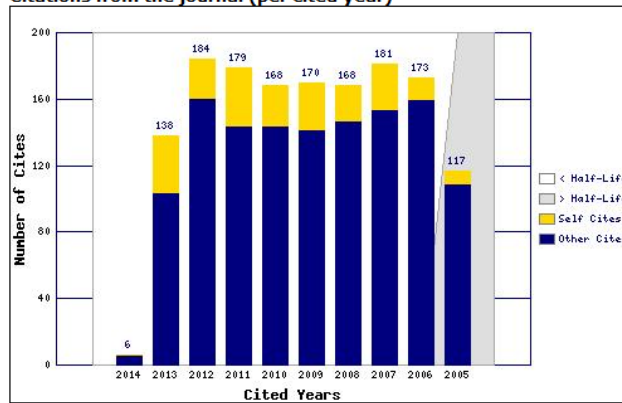| Cited Year	2014	2013	2012	2011	2010	2009	2008	2007	2006	2005	2004-all
# Cites from 2014	6	138	184	179	168	170	168	181	173	117	1228
Cumulative %	0.22	5.31	12.09	18.69	24.89	31.16	37.35	44.03	50.41	54.72	100

Citing Half-Life Calculations:
The citing half-life calculation finds the number of publication years from the current JCR year that account for 50% of citations in the journal. Read help for more information on the calculation.

Citing Journal Graph ⓘ ▲

Click here for Citing Journal data table

This graph shows the distribution by cited year of citations from current-year items in the journal STRUCT CONTROL HLTH.

Citations from the journal (per cited year)

- The white/grey division indicates the citing half-life (if < 10.0). Half of the citations from the journal's current items are to items published more recently than the citing half-life.

- The top (gold) portion of each column indicates Journal Self-Citations: citations from items in the journal to items in the same journal.

- The bottom (blue) portion of each column indicates Non-Self Citations: citations from the journal to items in other journals.

Journal Source Data ⓘ ▲

	Citable items			
	Articles	Reviews	Combined	Other items
Number in JCR year 2014 (A)	81	3	84	0
Number of references (B)	2428	284	2712	0.00
Ratio (B/A)	30.0	94.7	32.3	0.0

🏷 Rank in Category: Structural Control & Health Monitoring

Journal Ranking ⓘ

For **2014**, the journal **Structural Control & Health Monitoring** has an Impact Factor of **2.133**.

This table shows the ranking of this journal in its subject categories based on Impact Factor.

Category Name	Total Journals in Category	Journal Rank in Category	Quartile in Category
CONSTRUCTION & BUILDING TECHNOLOGY	59	8	Q1
ENGINEERING, CIVIL	125	19	Q1
INSTRUMENTS & INSTRUMENTATION	56	11	Q1

Category Box Plot ⓘ

For **2014**, the journal **Structural Control & Health Monitoring** has an Impact Factor of **2.133**.

This is a box plot of the subject category or categories to which the journal has been assigned. It provides information about the distribution of journals based on Impact Factor values. It shows median, 25th and 75th percentiles, and the extreme values of the distribution.
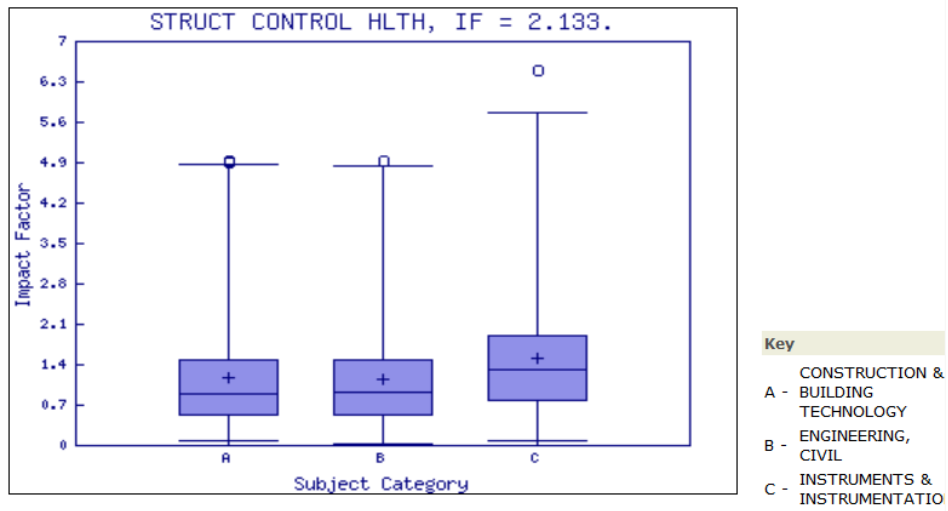
Capítulo de libro:

- *Multispectral imaging: fundamentals, principles and methods to damage assessment in constructions*

Bipublishers
Bibliometric Indicators for Publishers

(http://bipublishers.es)

(https://twitter/EC3metrics)

CRC Home (http://bipublishers.es/)   Indicators   Methodology   Team (http://bipublishers.es/team/)

Press

Data   Name variants

Publisher name	CRC Press
Website	http://www.crcpress.com/ (http://www.crcpress.com/)

Fields

Fields	PBK	PCH	CIT	FNCS	AI	ED
Science	145	1946	3412	1.56	1.97	56%
Engineering & Technology	126	1832	2400	1.22	4.71	58%
Social Sciences	34	560	158	0.45	0.33	61%
Humanities & Arts	8	110	90	1.73	0.10	51%

Disciplines	PBK	PCH	CIT	FNCS	AI	ED
Engineering	70	1057	1461	1.29	5.02	53%
Mathemathics	47	606	1424	1.25	5.70	25%
Computer Science	42	537	823	1.24	5.29	59%
Technology	42	681	599	0.87	4.83	74%
Applied Physics and Chemistry	21	324	886	1.74	5.32	71%
Earth & Enviromental Sciences	20	223	263	0.91	1.51	48%
Economics, Business & Management	18	299	93	0.48	0.62	63%
Medicine & Clinical Medicine	17	306	426	2.65	0.71	81%
Biological Sciences - Humans	16	212	376	1.83	1.84	72%
Chemistry	15	152	307	1.03	3.91	74%
Biological Sciences - Animals & Plants	14	212	251	0.79	1.92	82%
Molecular Biology and Biochemistry	13	206	180	0.83	2.80	86%
Physics & Astronomy	10	139	168	0.95	3.09	37%
Materials Science	9	88	214	1.82	2.13	48%
Political Science & International Relations	9	146	34	0.34	0.31	48%
Law, Criminology & Penology	8	116	47	0.87	0.65	40%

APÉNDICE B

SOFTWARE MULRACS

SOFTWARE MULRACS

MULRACS-Multispectral Radiometric Calibration Software

Tipo: Registro de la propiedad intelectual

Referencia: SA-00/2015/4722

Universidad: Universidad de Salamanca

Códigos UNESCO:

- 2209.18 Fotometría
- 2209.20 Radiometría
- 2209.90 Procesado de Imágenes
- 3311.11 Instrumentos Ópticos

Resumen:

Aplicación informática para la calibración radiométrica de sensores pasivos en su uso de rango cercano (sin que se vean afectados por la absorción atmosférica de radiación solar). La calibración implementada por dicho software está basada en el método vicario de radiancias y puede aplicarse tanto al caso de sensores monoespectrales como multiespectrales. Una vez el sensor esté calibrado se podrán obtener imágenes en magnitudes físicas (reflectancias o radiancias) las cuales pueden ser explotadas para obtener información sobre recursos naturales, medio ambiente, agricultura de precisión, clasificación de cultivos, etc. de gran utilidad para la comunidad científica y para empresas que lleven a cabo análisis de firmas espectrales y análisis radiométricos de imágenes.

Aplicaciones:

Aplicación de gran interés para las empresas que trabajan con firmas espectrales y análisis radiométricos de imágenes ya sea para realizar

evaluaciones, investigaciones, inspección de materiales o estudios de producción de los recursos naturales. También resulta de gran interés para la comunidad científica internacional en aras de investigar el potencial de los sensores radiométricos/geométricos que se utilizan con asiduidad para otros propósitos.

Autores:

- Susana Del Pozo Aguilera
- Mónica Herrero Huerta
- David Hernández López
- Pablo Rodríguez Gonzálvez
- Diego González Aguilera

Algunas Características:

Cualquier empresa o grupo de investigación que aspire a realizar análisis de cualquier cubierta o material terrestre mediante el uso de sensores remotos, han de, previamente, calibrar los mismos adoptando una serie de protocolos de medición y calibración que ayuden a controlar de forma adecuada la inspección de las superficies/materiales a estudiar. El software.

MULRACS permite realizar una calibración rigurosa de los sensores a través del método de calibración basado en radiancias. Aplica un ajuste por mínimos cuadrados al conjunto de imágenes capturadas y que recogen las superficies artificiales que servirán para la calibración.

$$Radiancia_i = f(c0_i, c1_i, ND_i) + \Delta\alpha_i \qquad (4)$$

donde $c0_i$ y $c1_i$, ordenada en el origen y ganancia o pendiente, son los coeficientes de calibración del dispositivo, ND_i los niveles digitales de las superficies artificiales extraídos de las imágenes, y α_i un coeficiente de corrección, todos ellos para cada una de las i bandas/canales del dispositivo.

Como método de resolución iterative se escogió el Método robusto de mínimos cuadrados Danés con el fin de asociar una serie de pesos en función del valor residual de cada iteración. De esta manera se se

descartan valores atípicos. El CD que se acompaña (contraportada de la tesis) incluye una versión digital de la tesis tanto en versión española como inglesa y un ejecutable del software MULRACS.

Datos de entrada:

- Medidas de radiancia procedentes de cada superficie de control obtenidas con espectroradiómetro calibrado
- Superficies Lambertianas artificiales como tarjetas/superficies de control para la calibración
- Superficies artificiales o naturales como superficies de chequeo de la calibración
- Eficiencia cuántica del sensor CCD O CMOS y de los filtros del dispositivo a calibrar
- Conjunto de imágenes junto a los parámetros de captura (focal, ISO, tiempo de exposición y apertura)

Productos:

- Parámetros de calibración del dispositivo por banda o canal
- Irradiancia solar
- Imágenes en valores de radiancia
- Imágenes en valores de reflectancia
- Resultados estadísticos de la calibración: gráficos, información correspondiente a las bandas/canals y a las superficies de control y chequeo.
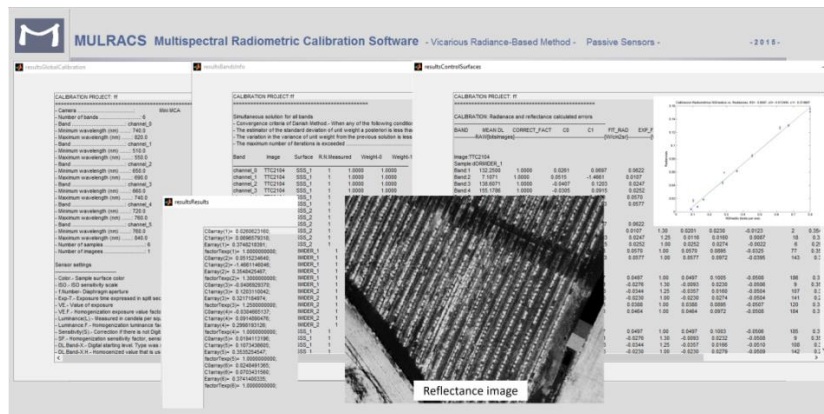
Figura Ap.B.1: Captura de pantalla de la interfaz del software mostrando algunos de los productos finales más relevantes.

CURRICULUM VITAE

Susana del Pozo Aguilera

01-07-1986   Nació en Ávila, España

Formación Académica

2011-2016   Tesis doctoral en el Departamento de Ingeniería Cartográfica y del Terreno, Escuela Politécnica Superior de Ávila, Universidad de Salamanca, España

2013   Grado en Ingeniería Civil, Universidad de Salamanca, España

2011   Master Oficial en Prevención de Riesgos Laborales, Universidad de la Rioja, España

2005-2009   Ingeniería Técnica en Obras Públicas, Universidad de Salamanca, España

Trabajo y Experiencia Profesional

2009-2016   Grupo de Investigación TIDOP

- Teledetección
- Ingeniería Inversa
- Fotogrametría y Visión Computacional

2014   Estancia de Investigación en TuDelft University of Technology, Paises Bajos (3 meses)

Publicaciones

Artículos en Revistas Internacionales

Gonzalez-Aguilera, D., Del Pozo, S., Lopez, G., & Rodriguez-Gonzalvez, P. (2012). From point cloud to CAD models: Laser and optics geotechnology for the design of electrical substations. Optics & Laser Technology, 44(5), 1384-1392.

González-Aguilera, D., Del Pozo, S., Holgado, A., & López, G. (2012, February). Spatial Information System for Management and Control of Electrical Substations. In Advanced Materials Research (Vol. 463, pp. 1686-1692). Trans Tech Publications.

Del Pozo, S., Rodríguez-Gonzálvez, P., Hernández-López, D., & Felipe-García, B. (2014). Vicarious Radiometric Calibration of a Multispectral Camera on Board an Unmanned Aerial System. Remote Sensing, 6(3), 1918-1937.

Del Pozo, S., Lindenbergh, R., Rodríguez-Gonzálvez, P., Blom, J. K., & González-Aguilera, D. (2015). Discrimination between Sedimentary Rocks from Close-Range Visible and Very-Near-Infrared Images. PloS one, 10(7), e0132471.

Conde, B., Del Pozo, S., Riveiro, B., & González-Aguilera, D. (2015). Automatic mapping of moisture affectation in exposed concrete structures by fusing different wavelength remote sensors. Structural Control and Health Monitoring.

Del Pozo, S., Herrero-Pascual, J., Felipe-García, B., Hernández-López, D., Rodríguez-Gonzálvez, P., & González-Aguilera, D. (2016). Multispectral Radiometric Analysis of Façades to Detect Pathologies from Active and Passive Remote Sensing. Remote Sensing, 8(1), 80.

Artículos de Conferencias

Del Pozo, S., Herrero-Pascual, J., Felipe-García, B., Hernández-López, D., Rodríguez-Gonzálvez, P., & González-Aguilera, D. (2015). Multi-sensor radiometric study to detect pathologies in historical buildings. The International Archives of Photogrammetry, Remote Sensing and Spatial Information Sciences, 40(5), 193.

Capítulos de Libro

Del Pozo, S; Sánchez-Aparicio, L.J; Rodríguez-Gonzálvez, P.; Herrero-Pascual, J.; Muñoz-Nieto, A.; González-Aguilera, D.; Hernández-López, D. Multispectral imaging: fundamentals, principles and methods to damage assessment in constructions. In Geotechnologies for the Reverse Engineering of Structures and Infrastructures; CRC Press/balkema, Francis & Taylor Group, December 2015.